Microcolony Dynamics: Motion from Growth, Order, and Incompressibility

by

Julien Smith-Roberge

A thesis
presented to the University of Waterloo
in fulfillment of the
thesis requirement for the degree of
Doctor of Philosophy
in
Applied Mathematics

Waterloo, Ontario, Canada, 2023

Examining Committee Membership

The following served on the Examining Committee for this thesis. The decision of the Examining Committee is by majority vote.

External Examiner:	Lennaert van Veen Department of Mathematics, University of Ontario Institute of Technology
Supervisor:	Brian Ingalls Department of Applied Mathematics, University of Waterloo
Internal Member(s):	Mohammad Kohandel Department of Applied Mathematics, University of Waterloo Henry Shum Department of Applied Mathematics, University of Waterloo
Internal-External Member:	Justin Wan Department of Computer Science, University of Waterloo

Author's Declaration

I hereby declare that I am the sole author of this thesis. This is a true copy of the thesis, including any required final revisions, as accepted by my examiners.

I understand that my thesis may be made electronically available to the public.

Abstract

Rod-shaped bacteria such as *E. coli* reproduce by expanding along their long axis and splitting into pairs of daughter cells. If conditions are favourable for growth, they will continue in this way, doubling repeatedly until they hit some limiting factor, such as a lack of nutrients or a buildup of toxic waste products. Long before they reach this stage, however, they must contend with another limited resource: space. As these bacteria lengthen, they push their neighbours aside to make room for their added volume. The result is a constantly shifting mass of tightly packed cells, each one rotating and reorienting itself in an ongoing competition for space.

In the past decade and a half, the physics governing this behaviour has garnered considerable attention, and a robust literature has developed, drawing on hydrodynamic theories of liquid crystals and their active matter counterparts (so-called "active nematics"). However, these models have relied exclusively on gradient effects to drive the dynamics of the system, and these are insufficient to describe the behaviour of real microcolonies, which exhibit asymmetric growth dynamics even in the absence of spatial gradients.

This thesis seeks to address this shortcoming. We do so by developing a novel model of microcolony dynamics, based in part on earlier models from the literature on nutrient-limited growth. We begin by showing that the physics in these models can be recast as a variational problem: minimizing the total kinetic energy. We then modify this variational problem to account for cell morphology, biasing the direction of a cell's motion based on its orientation. The result is a new model of microcolony growth that exhibits asymmetric spreading. Next, we develop numerical schemes to simulate our system, combining techniques from finite difference methods, level set methods, and unfitted finite element methods. These schemes are validated against analytical solutions. Finally, we use these numerical implementations to explore the behaviour of our model in more complex scenarios where exact solutions are lacking. Our findings suggest that this novel mechanism can reproduce several behaviours observed in real microcolonies, such as spontaneous alignment in semi-confined domains, as well as fingering and defect generation at a microcolony's boundary. We conclude by proposing some strategies to incorporate our model into other models in the active nematic literature.

Acknowledgements

I would like to thank my supervisor, Brian Ingalls, for his seemingly endless reserves of patience and support, Sander Rhebergen and Marek Stastna, for lending us their expertize when we ventured into unfamiliar territory, Bastien Polizzi, for his insights on biofilm modeling, and my lab mates, Nathan Braniff, Leon Avery, Sara Haghayegh Khorasani, Atiyeh Ahmadi, and Aaron Yip, who were always quick to offer help whenever I asked for it. I would like to thank my mother, Virginia Smith, my father, André Roberge, and my stepmother, Tony Payzant, for their love and support. I would especially like to thank my sister, Evelyne Smith-Roberge, and her husband, Sean Kafer, who made Waterloo feel like home. If I have seen further than others, it's because Evelyne told me about it. Finally, thank you to my partner, Kyle Shellington, who made these last few months of writing bearable.

Dedication

I dedicate this thesis to my cat, Eliot, though he has done nothing to deserve it.

Table of Contents

List of Figures

List of Tables

Chapter 1

Introduction

Rod-shaped bacteria such as *E. coli* reproduce by expanding along their long axis and splitting into pairs of daughter cells. If conditions are favourable for growth, they will continue in this way, doubling repeatedly until they hit some limiting factor, such as a lack of nutrients or a buildup of toxic waste products. Long before they reach this stage, however, they must contend with another limited resource: space. As these bacteria lengthen, they push their neighbours aside to make room for their added volume. The result is a constantly shifting mass of tightly packed cells, each one rotating and reorienting itself in an ongoing competition for space. This thesis seeks to investigate these early stages of colony formation using partial differential equation (PDE) models.

1.1 Bacteria

Bacteria are ubiquitous throughout both natural and man-made environments. The vast majority are beneficial, such as those responsible for soil health [37], the fermentation of food and drink [14], or the many species that make up our microbiome [31]. Others are responsible for disease, from minor irritants like dental plaque to life-threatening illnesses like tuberculosis.

As a bacterium grows from a single cell to a population, it will exhibit a diverse range of behaviours. Even restricting ourselves to biophysics, we find rich and unique modeling challenges at all stages of colony development, from the motion of daughter cells after the first cell division [65], to the early stages of microcolony formation when a 2-dimensional layer of cells begins to colonize a surface (the subject of this thesis), to the buckling of said

layer into the third dimension [9][36][73][48], all the way up to the material properties of biofilms [10]. Of course, bacterial colonies also exhibit interesting behaviour beyond their basic physical behaviour, from chemotaxis [66], to quorum sensing [57], to the collective dynamics of biofilms [43] and microbial communities [34].

Our work falls under the purview of active matter research, an interdisciplinary field drawing on mathematics, physics, chemistry, biology, and engineering. Active matter distinguishes itself from conventional matter by the fact that its constituent particles are governed not just by external energy sources, but also internal ones. Active particles can use energy to direct their own behaviour e.g. by propelling themselves. Examples include swarming fish, vibrating rods, microtubules, and growing bacteria.

From a purely mathematical perspective, active matter is interesting due to its propensity to exhibit emergent collective behaviour. Large collections of active particles will often perform coherent, large-scale behaviour that is not readily predictable from the microscopic behaviour of its individual constituent particles. Much of active matter research is to devoted to teasing out how these macroscopic behaviours emerge from the interactions of active particles.

The physical dynamics of growing microcolonies also poses interesting biological questions, both from an evolutionary perspective and for laboratory experiments. Regarding the first point, biologists have long observed that bacteria come in a dazzling array of cell morphologies, and these differences in shape impact the way bacteria interact when they come into physical contact. In the past few decades researchers have begun investigating what fitness advantage these various morphologies might confer [74].

Volfson *et al.* [69] and Cho *et al.* [15] have hypothesized that *E. coli*'s rod shape might facilitate growth in semi-confined spaces, such as pores and cracks on surfaces. Their experiments show that microcolonies spontaneously self-organize when grown in such environments. Cho *et al.* observed that *E. coli* appear to have an aspect ratio just large enough to facilitate collective motion, without being so large as to cause "traffic jam" effects. They further hypothesize that this organization may aid in waste elimination and nutrient flow. Cell orientation may also impact the efficiency of certain cell-cell interactions. For instance, experiments done by Seoane *et al.* [62] show that conjugation efficiency is affected by the relative orientation of the donor/recipient pair. Moving beyond bacteria, the same motion-by-growth mechanism that governs the dynamics of bacterial microcolonies has been shown to impact the evolutionary fitness of yeast cells growing in crowded environments [40].

The dynamics of cell orientation may also bear on the results of laboratory experiments. In recent years, microfluidic devices have emerged as an important experimental technology [7]. These devices can function as microchemostats, allowing researchers to grow cells in a

controlled environment, potentially indefinitely [70], all while exerting precise control over their growth environment and performing continuous observations of the growing cells. However, as they are currently used, these devices have a limited capacity, holding no more than a few hundred to a few thousand cells. At this scale, the physics of cell growth could dramatically impact the outcome of experiments.

For example, the outcome of conjugation experiments performed in our lab appeared to depend, at least in part, on the initial physical orientation of the donor cells (see figure 1.1). In these experiments, donor cells (the red cells in figure 1.1) pass on their genetic material to recipient cells (green) via conjugation, creating transconjugants (yellow/orange). The total conjugation efficiency, measured as the fraction of recipient cells that became transconjugants, varied significantly between experiments. Based on our initial observations, it appears that the ultimate fate of any given experiment depends not only on the conjugation rate, but also on the physical motion of the cells themselves. When designing such experiments, it is therefore crucial to consider how the physics of cell growth might impact the ultimate outcome. Understanding these physical processes could help researchers design more robust microfluidic studies.

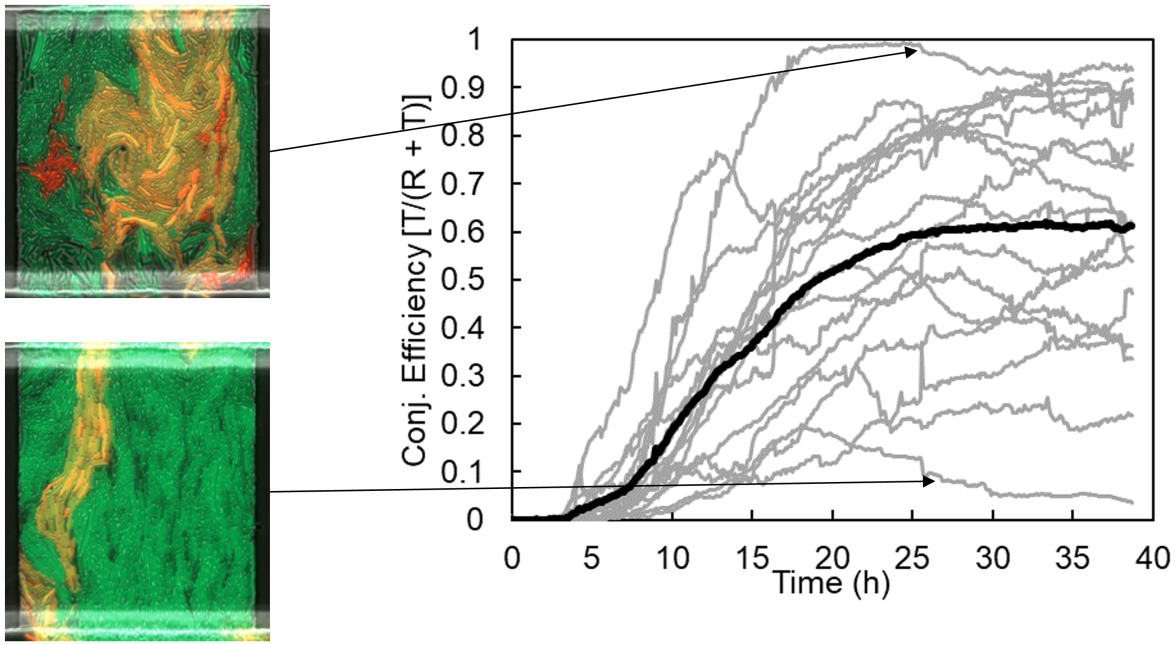

Figure 1.1: Despite starting with similar cell concentrations, the final results of conjugation experiments exhibit a wide range of conjugation efficiency (unpublished data, produced by Aaron Yip). The images on the left are snapshots of conjugation experiments, while the plot on the right shows the conjugation efficiency over time for multiple experiments. We conjecture that these differences could be explained by the physical dynamics of the underlying system.

The remainder of this thesis splits into four main sections. The rest of Chapter 1 will be devoted to reviewing liquid crystal theory and the previously published models that have applied this theory to the physics of bacterial growth. In Chapter 2, we derive the models that lie at the core of our work. Chapter 3 is devoted to the numerical implementation of these models, while Chapter 4 explores both the exact analytical solutions, as well as some results from numerical experiments. Avenues for future work are discussed in Chapter 5.

1.2 Liquid Crystals

This thesis seeks to apply hydrodynamic models of liquid crystals to study the microcolony dynamics of rod-shaped bacteria.

Liquid crystals are an intermediate state of matter, sharing, as the name suggests, qualities of both liquids and crystals. Whereas a liquid is a state of matter where the positions and orientations of its constituent particles have no long-range correlations, and a crystal is a state of matter where the positions and orientations of its constituent particles have strong long-range correlations, a liquid crystal is a state of matter which exhibits no correlation in particle position, but which can exhibit strong long-range correlation in particle orientation. For our purposes, we may think of a liquid crystal as a fluid composed of asymmetrically shaped particles (e.g. rods or disks).

Hydrodynamic models of liquid crystals are a class of PDE models that generalize the traditional Navier–Stokes equations. In addition to the usual quantities associated with fluid dynamics—density, velocity, pressure, etc.—liquid crystal models introduce new field variables that characterize the liquid crystal's micro-structure, such as particle orientation.

Bacteria such as *E. coli* are also asymmetrically shaped and can be treated as particles in a fluid. Liquid crystal models are therefore well-suited to describe the behaviour of bacterial colonies. We review the relevant liquid crystal theory below.

1.2.1 Order Parameters

Liquid crystals exhibit phase transitions. When density is low, the particles making up the crystal have enough space to move freely, and can assume any orientation. However, once they reach some critical density, the particles are forced to become aligned.[1] This alignment is quantified using order parameters [51], the simplest of which is the director $\vec{d}$, the unit vector that measures the average orientation in some small volume of space. I.e. $\vec{d} = \begin{bmatrix}\cos(\theta)\\ \sin(\theta)\end{bmatrix}$, where θ is the average angle. We may extend this measurement by introducing the scalar order parameter, S, which in two dimensions is defined to be:

$$S = \langle 2\cos^2(\bar{\theta}) - 1 \rangle$$

where $\bar{\theta} = \theta - \theta_i$ is the angle of the ith cell w.r.t. the director and $\langle\cdot\rangle$ denotes a statistical average.[2] Whereas $\vec{d}$ measures the mean orientation, S is a measure of orientation vari-

[1] Liquid crystals can also exhibit phase transitions based on the temperature of the system. Temperature can also impact the behaviour of bacteria (e.g. by changing their growth rate). We will avoid that particular can of worm, and focus here only on the effects of density.

[2] This average can be calculated in a number of different ways. If one knows the precise position and orientation of all the particles, we can calculate $S = \frac{1}{N}\sum_{i=1}^{N} 2\cos^2(\bar{\theta}_i) - 1$ where $\bar{\theta}_i$ is the angle w.r.t. the director of the ith particle in some small ball, B, containing $N \gg 1$ particles. This works well when the

ability, roughly analogous to the standard deviation. S takes the value 0 when the system is disordered, and 1 when it is completely ordered (see figure 1.2).

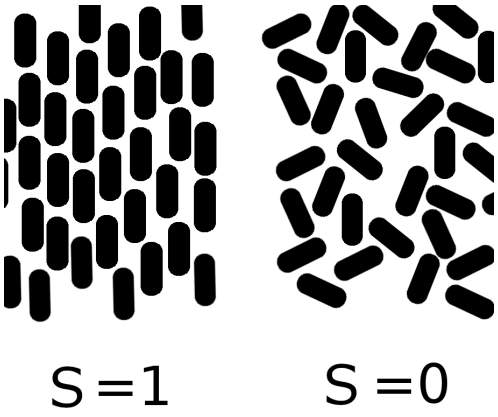

Figure 1.2: Behaviour of the scalar order parameter, $S = \langle 2\cos^2(\bar{\theta}) - 1 \rangle$.

Combining $\vec{d}$ and S, we obtain the tensor order parameter, $\mathbf{Q}$, which in 2D is defined by:

$$Q_{\alpha\beta} = 2S\left(d_\alpha d_\beta - \frac{1}{2}\delta_{\alpha\beta}\right)$$

where $Q_{\alpha\beta}$ denotes the $\alpha\beta$'th component of the matrix $\mathbf{Q}$. Similarly, d_α is the α'th component of $\vec{d}$. δ is the Kronecker delta:

$$\delta_{\alpha\beta} = \begin{cases} 1 & \text{if } \alpha = \beta \\ 0 & \text{otherwise} \end{cases}$$

Alternatively, we may write $\mathbf{Q} = 2S\left(\vec{d}\otimes\vec{d} - \frac{1}{2}\mathbf{I}\right)$.[3]

number of particles is large.

Alternatively, we may calculate $S = \int_B \int_0^{\frac{\pi}{2}} (\cos^2(\bar{\theta}) - 1) f(\bar{\theta})\, d\bar{\theta}\, dA$ where $f(\bar{\theta})$ is the statistical distribution of $\bar{\theta}$. This measurement is more robust, especially when the number of particles is small and the discrete sum has a large variance, but it requires us to estimate $f(\bar{\theta})$.

[3] A note of caution to the reader: some authors choose to omit the factor of two in the definition of $\mathbf{Q}$. We adopt the convention above because it eliminates several factors of $\frac{1}{2}$ from quantities related to $\mathbf{Q}$.

$\mathbf{Q}$ is a symmetric, traceless matrix. When written in terms of θ, $\mathbf{Q}$ takes the form

$$\mathbf{Q} = S \begin{pmatrix} \cos(2\theta) & \sin(2\theta) \\ \sin(2\theta) & -\cos(2\theta) \end{pmatrix}.$$

Furthermore $\mathbf{Q}$ has S as its largest eigenvalue, with corresponding eigenvector $\vec{d}$, and $\det(\mathbf{Q}) = -S^2$. Note also that $\mathbf{Q}$ is invariant under the symmetry $\vec{d} \to -\vec{d}$.

Admittedly, combining $\vec{d}$ and S in this way may seem like an odd thing to do. The director, $\vec{d}$, and scalar order parameter, S, have clear physical interpretations, whereas $\mathbf{Q}$ is less transparent. Indeed, as we will discuss below, this lack of transparency may have contributed to several authors creating mathematical models in which S can exceed one, which conflicts with its definition. In truth, the advantages of using the Q-tensor are most apparent when working in three dimensions. There, liquid crystals can exhibit orientational order along multiple axes. These complex physical configurations, and the transitions between them, are not easy to describe using directors. As such, a great deal of the liquid crystal literature has been developed using the Q-tensor description. So while the Q-tensor formalism is perhaps overkill for two-dimensional systems, there is nothing to be gained by developing a separate formalism.

For more information about liquid crystals and the order parameters discussed above, see [51] and [3].

1.2.2 Static Theory

Having defined the tensor order parameter, we can use it to derive a description of a liquid crystal's equilibrium state. Our derivation follows [35]. We will generalize this to a dynamical theory in the next section.

A liquid crystal's equilibrium can be derived from a quantity called the Landau-de Gennes free energy.[4] Landau theories are phenomenological descriptions of thermodynamic systems that are derived using a top-down approach. Rather than seeking to coarse-grain a detailed description of the microstates, they rest on three assumptions:

- There exists a scalar function, F, called the *Landau free energy*, which can fully characterize the macroscopic behaviour of the system for states near a phase transition.

[4]Named after Lev Landau, who introduced the general methodology, now called Landau theory, used to describe phase transitions, and Pierre-Gilles de Gennes, who applied this theory to the case of liquid crystals.

The value of this function depends on the system's order parameter (in our case, $\mathbf{Q}$). The equilibrium value of the order parameter is obtained by minimizing the free energy.

- F is analytic.
- F respects all the symmetries of the system.[5]

When applied to 2D liquid crystals, we obtain the Landau-de Gennes free energy. Expanding the free energy in terms of a power series and truncating higher order terms, we obtain the following (equivalent) approximations:

$$F(\mathbf{Q}) \approx F_0 + \frac{1}{2}AQ_{\alpha\beta}Q_{\alpha\beta} + \frac{1}{4}C(Q_{\alpha\beta}Q_{\alpha\beta})^2 \tag{1.1}$$

$$= F_0 + \frac{1}{2}A\mathrm{Tr}(\mathbf{Q}^2) + \frac{1}{4}C\mathrm{Tr}(\mathbf{Q}^2)^2 \tag{1.2}$$

$$= F_0 + AS^2 + \frac{1}{2}CS^4 \tag{1.3}$$

The series coefficients A and C are to be determined. Note that in equation 1.1 we are summing over repeated indices. I.e.:

$$Q_{\alpha\beta}Q_{\alpha\beta} = \sum_{\alpha=1}^{2}\sum_{\beta=1}^{2} Q_{\alpha\beta}Q_{\alpha\beta}$$

This is a convention we will use throughout this thesis.

Per the symmetry assumption, all terms in the power series that are not invariant under rotation must vanish. The series expansion of a general function of $\mathbf{Q}$ would also include, e.g., a term of the form BQ_{11}, but such terms cannot appear in the expansion of F. We can also notice that $\mathbf{Q}$ has only two degrees of freedom: S and θ. Of these, only S is invariant under rotations, so it should come as no surprise that F can be written as a function of S alone.

The unknown coefficients A and C are functions of the other thermodynamic parameters of our system, and in general it is difficult to determine which coefficient functions best

[5] One typically assumes that F respects the symmetries of the system's Hamiltonian, but this is itself predicated on the assumption that we can describe the microscopic dynamics of our system using Hamiltonian mechanics. This is not at all obvious in our case of growing bacteria given that neither mass nor energy are conserved.

model any given thermodynamic system. The assumptions of Landau theory can only take us so far; to make further progress, one would have to appeal to the microscopic description of the system. However, we can make several simplifying assumptions that reproduce the qualitative behaviour we expect of our system, namely that the system undergoes a phase transition at some critical density, b^*. Specifically, S should be identically zero when the density, b, is below b^*, and positive when $b > b^*$. Assuming that A takes the form $A_0(b^* - b)$ and that C is constant (or at the very least positive, to ensure the function is concave up) is enough to enforce the desired behaviour.[6] The fact that A changes sign allows the phase transition to occur, and a linear form is the simplest expression that allows for a sign change. The behaviour of this function is illustrated in Figure 1.3.

[6]Recall that Landau theory only assumes that F characterizes the states near a phase transition. Because the phase transition occurs when $A = 0$, taking A to be linear can be interpreted as a linearization of A, valid for densities close to the critical density.

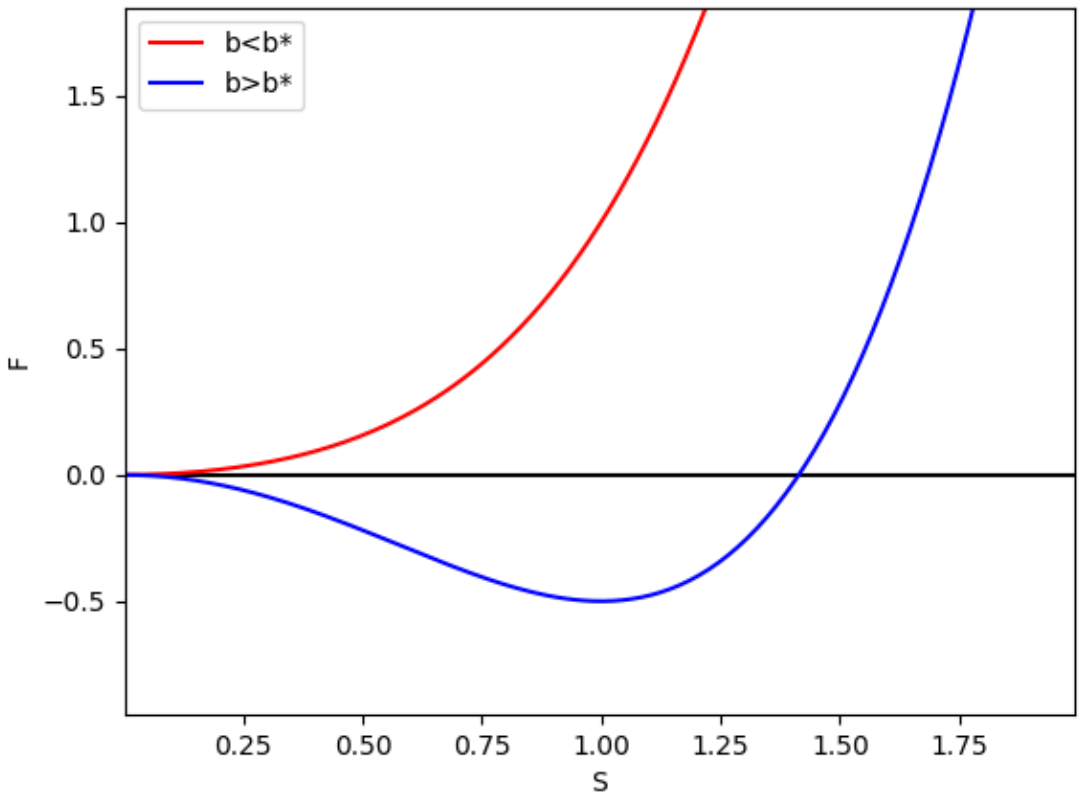

Figure 1.3: A plot of $F(S) = A_0(b^* - b)S^2 + \frac{1}{2}CS^4$. When $b < b^*$, in red, F has a minimum at $S = 0$. When $b > b^*$, in blue, F has a minimum at $S > 0$.

If we expect that spatial gradients should impact the behaviour of our system, equation 1.1 is extended to:

$$F(\mathbf{Q}) = F_0 + \frac{1}{2}AQ_{\alpha\beta}Q_{\alpha\beta} + \frac{1}{4}C(Q_{\alpha\beta}Q_{\alpha\beta})^2 + \frac{1}{2}K\partial_i Q_{\alpha\beta}\partial_i Q_{\alpha\beta} \tag{1.4}$$

where $i = x, y$. This last term is sometimes called the Frank elastic free energy, after Frederick Charles Frank.

The free energy function we have described thus far does produce the described phase

transition, but we require additional assumptions to guarantee that it predicts an equilibrium values for S between 0 and 1. (Recall that the predicted equilibrium value for S is the value that minimizes F.) In the absence of any spatial gradients, F takes the form:

$$\begin{aligned} F &= F_0 + AS^2 + \frac{1}{2}CS^4 \\ &= F_0 + A_0(b^* - b)S^2 + CS^4 \end{aligned}$$

This functions has two non-negative critical points: $S_{eq} = 0$, and $S_{eq} = \sqrt{-2A_0(b^* - b)/C}$. Following [72] and [32], we further assume that $C = 2A_0 b$, so the non-zero solution reduces to $S_{eq} = \sqrt{1 - \frac{b^*}{b}}$, guaranteeing that S_{eq} will remain in the desired range. See figure 1.4.

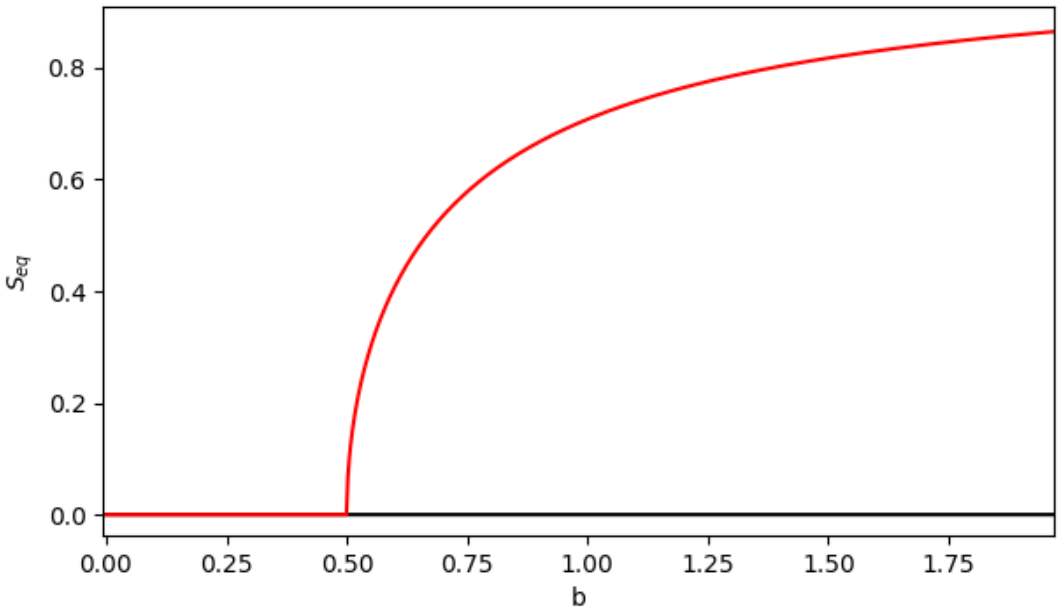

Figure 1.4: The non-zero S_{eq} value as a function of the density, b, with $b^* = 0.5$. $S_{eq} = 0$ when $b < b^*$, but when $b > b^*$ the system undergoes a phase transition, trending towards $S_{eq} = 1$ as $b \to \infty$.

Having derived the Landau-de Gennes free energy, we are almost ready to describe the hydrodynamic theory of liquid crystals that underlies the core of this thesis. Before we do so, we need to introduce one final quantity, **H**, called the molecular field/molecular tensor.

H is given by the functional derivative of the free energy, i.e.:

$$\begin{aligned} H_{\alpha\beta} &= -\frac{\delta}{\delta Q_{\alpha\beta}} \int F dA \\ &= -\left(A + \frac{1}{2} S^2 C\right) Q_{\alpha\beta} + K \Delta Q_{\alpha\beta} \\ &= A_0 b \left(1 - \frac{b^*}{b} - S^2\right) Q_{\alpha\beta} + K \Delta Q_{\alpha\beta} \\ &= A_0 b \left(S_{eq}^2 - S^2\right) Q_{\alpha\beta} + K \Delta Q_{\alpha\beta} \end{aligned}$$

H will enter our model as a gradient flow term. Where F tells us, by means of its minimum, the location of the equilibrium state, **H** tells us what direction we need to travel in order to reach it.

1.2.3 Dynamic Theory

Dynamical theories for liquid crystals split into two broad categories: director-based theories, epitomized by the Ericksen-Leslie equations [29, 30, 47], and Q-tensor theories. In contrast to Ericksen-Leslie theory, which to our knowledge has no real competitors, several competing Q-tensor formulations exist in the literature. (See [53] for a survey.) Among the existing Q-tensor models, the two most widely used in the context of bacterial dynamics are the Beris-Edwards equations [8] and the Olmsted-Goldbart equations [54].

The Beris-Edwards equations, developed in 1994 by Antony Beris and Brian Edwards in [8], were derived using a generalization of the Poisson-bracket method, suitably modified to account for dissipative forces. The Q-tensor component of the equations reads:

$$\begin{aligned} \left(\partial_t + \vec{v} \cdot \nabla\right) Q_{\alpha\beta} = &(\xi u_{\alpha\gamma} + \omega_{\alpha\gamma})(Q_{\gamma\beta} + \delta_{\gamma\beta}) + (Q_{\alpha\gamma} + \delta_{\alpha\gamma})(\xi u_{\gamma\beta} - \omega_{\gamma\beta}) \\ &- \frac{2\xi}{d}(Q_{\alpha\beta} + \delta_{\alpha\beta})\mathrm{tr}(\mathbf{Qu}) + \Gamma H_{\alpha\beta} \end{aligned} \tag{1.5}$$

In the above, $d = 2, 3$ is the dimension of the system, $\vec{v}$ is the velocity field, and $H_{\alpha\beta}$ is the molecular field introduced in the previous section. The parameter Γ is the rotational viscosity, which controls the rate at which the system tends towards thermodynamic equilibrium, and ξ is an alignment parameter that depends on the aspect ratio of the liquid crystal particles.

The quantities $\mathbf{u}$ and $\boldsymbol{\omega}$ are defined by:

$$u_{\alpha\beta} = \frac{\partial_\beta v_\alpha + \partial_\alpha v_\beta}{2} - \frac{1}{d}\partial_\gamma v_\gamma \delta_{\alpha\beta} \tag{1.6}$$

$$\omega_{\alpha\beta} = \frac{\partial_\beta v_\alpha - \partial_\alpha v_\beta}{2} \tag{1.7}$$

Again, we highlight the differing conventions in the liquid crystal literature. We are here using the definition $\mathbf{Q} = dS(\vec{d} \otimes \vec{d} - \frac{1}{d}\mathbf{I})$. If we omit the initial factor of d, equation 1.5 would contain several additional factors of $\frac{1}{d}$.

Strictly speaking, equation 1.5 is a generalization of the classical Beris-Edwards equations, which were originally formulated for incompressible flows. In that case, the definition of $\mathbf{u}$ simplifies to $u_{\alpha\beta} = (\partial_\beta v_\alpha + \partial_\alpha v_\beta)/2$, thus $\mathbf{u}$ and $\boldsymbol{\omega}$ are respectively the symmetric and skew-symmetric components of the strain-rate tensor. However, when $\nabla \cdot \vec{v} \neq 0$, this definition of $\mathbf{u}$ is not trace-free, and therefore equation 1.5 would not preserve the trace-free nature of $\mathbf{Q}$. Following [21], [72], and [59], we apply the correction defined in equation 1.7.

When $d = 2$, equation 1.5 can be simplified significantly. Expanding, we obtain:

$$\begin{aligned}(\partial_t + \vec{v} \cdot \nabla)\, Q_{\alpha\beta} = {} & 2\xi u_{\alpha\beta} + \omega_{\alpha\gamma} Q_{\gamma\beta} - Q_{\alpha\gamma}\omega_{\gamma\beta} + (u_{\alpha\gamma} Q_{\gamma\beta} + Q_{\alpha\gamma} u_{\gamma\beta} - \mathrm{tr}(\mathbf{Qu})\delta_{\alpha\beta}) \\ & - \xi Q_{\alpha\beta}\mathrm{tr}(\mathbf{Qu}) + \Gamma H_{\alpha\beta}\end{aligned}$$

This can be simplified further using the following lemma.

Lemma 1.2.1. *Given any two 2x2 symmetric trace-free matrices* $\mathbf{A}$ *and* $\mathbf{B}$*, the following identity holds:*

$$\mathbf{AB} + \mathbf{BA} = tr(\mathbf{AB})\mathbf{I}$$

Proof. A direct computation yields:

$$\begin{aligned}\mathbf{AB} + \mathbf{BA} &= \begin{pmatrix} a_{11} & a_{12} \\ a_{12} & -a_{11} \end{pmatrix}\begin{pmatrix} b_{11} & b_{12} \\ b_{12} & -b_{11} \end{pmatrix} + \begin{pmatrix} b_{11} & b_{12} \\ b_{12} & -b_{11} \end{pmatrix}\begin{pmatrix} a_{11} & a_{12} \\ a_{12} & -a_{11} \end{pmatrix} \\ &= \begin{pmatrix} 2a_{11}b_{11} + 2a_{12}b_{12} & 0 \\ 0 & 2a_{11}b_{11} + 2a_{12}b_{12} \end{pmatrix} \\ &= \mathrm{tr}(\mathbf{AB})\begin{pmatrix} 1 & 0 \\ 0 & 1 \end{pmatrix}\end{aligned}$$

□

Thus, because $\mathbf{u}$ and $\mathbf{Q}$ are both symmetric and trace-free, it follows that $u_{\alpha\gamma}Q_{\gamma\beta} + Q_{\alpha\gamma}u_{\gamma\beta} - \mathrm{tr}(\mathbf{Qu})\delta_{\alpha\beta} = 0$, and so 1.5 simplifies to:

$$(\partial_t + \vec{v}\cdot\nabla)\,Q_{\alpha\beta} = 2\xi u_{\alpha\beta} + \omega_{\alpha\gamma}Q_{\gamma\beta} - Q_{\alpha\gamma}\omega_{\gamma\beta} - \xi\mathrm{tr}(\mathbf{Qu})Q_{\alpha\beta} + \Gamma H_{\alpha\beta}{}^{7} \tag{1.8}$$

In contrast to the Beris-Edwards equations, which require an involved derivation based on their novel Poisson bracket formalism,[8] the Olmsted-Goldbart equation can be derived in just a few lines. The derivation, which may be found in [54] or [32], proceeds in much the same way as the derivation of Landau-de Gennes free energy seen in section 1.2.2. I.e.: we truncate a series expansion and discard all terms that are not of the correct form. Specifically, we posit that the interaction terms between the flow, $\vec{v}$, and the Q-tensor can be represented by an analytic function, f, of the relevant field variables ($\mathbf{u}$, $\boldsymbol{\omega}$, and $\mathbf{Q}$), which we expand to second order and discard all terms that are not symmetric and trace-free. In two dimensions, this procedure yields:

$$\begin{aligned}(\partial_t + \vec{v}\cdot\nabla)\,Q_{\alpha\beta} &= f(\mathbf{u},\boldsymbol{\omega},\mathbf{Q}) + \Gamma H_{\alpha\beta} \\ &= Au_{\alpha\beta} + B\left(\omega_{\alpha\gamma}Q_{\gamma\beta} - Q_{\alpha\gamma}\omega_{\gamma\beta}\right) + \Gamma H_{\alpha\beta}\end{aligned}$$

Comparing this equation to the Eriksen-Leslie theory, we find that $B = 1$. After relabeling $A = 2\xi$, we obtain:

$$(\partial_t + \vec{v}\cdot\nabla)\,Q_{\alpha\beta} = 2\xi u_{\alpha\beta} + \omega_{\alpha\gamma}Q_{\gamma\beta} - Q_{\alpha\gamma}\omega_{\gamma\beta} + \Gamma H_{\alpha\beta} \tag{1.9}$$

This equation is almost identical to equation 1.8. The only difference is the absence of the third-order term, $\xi\mathrm{tr}(\mathbf{Qu})Q_{\alpha\beta}$. Unfortunately, this term is required to ensure that S remains bounded between 0 and 1. Without it, S can take on unphysical values, as we will now show.

We now return to the problem we foreshadowed in section 1.2.1. It is not initially obvious that there should be anything wrong with equation 1.9, and this is in part due to

[7] If we rewrite the equation in the form

$$(\partial_t + \vec{v}\cdot\nabla)\,Q_{\alpha\beta} + Q_{\alpha\gamma}\omega_{\gamma\beta} - \omega_{\alpha\gamma}Q_{\gamma\beta} = 2\xi u_{\alpha\beta} - \xi\mathrm{tr}(\mathbf{Qu})Q_{\alpha\beta} + \Gamma H_{\alpha\beta}$$

then the LHS of this equation is the corotational time derivative, a generalization of the material derivative that accounts for both translation and rotation. The first two terms on the RHS represent the effects of shear while the last term represents relaxation to thermodynamic equilibrium.

[8] In their book, *Thermodynamics of Flowing System with Internal Microstructure*, Beris and Edwards take up the subject of liquid crystals after roughly 450 pages, at which point they state: "LC dynamics are the perfect test of the thesis of this book, and, in a sense, a mild climax, since in order to describe LCs we shall have to use nearly everything that we have learned thus far." [8]

the fact that $\mathbf{Q}$ has no obvious physical interpretation. It is difficult to tell at a glance what values $\mathbf{Q}$ can take, or how to interpret those values. Fortunately, there is a relatively straightforward procedure that allows us to decouple a dynamical equation for $\mathbf{Q}$ into dynamical equations for θ, the angle of the director, and S, the scalar order parameter. This procedure is found in an appendix to [32], a paper commonly cited by those using the Olmsted-Goldbart equation to model bacterial dynamics. We reproduce it below.

Recall that $\mathbf{Q} = S\begin{pmatrix}\cos 2\theta & \sin 2\theta \\ \sin 2\theta & -\cos 2\theta\end{pmatrix}$. We define the following matrices:

$$\boldsymbol{\sigma_p} = \begin{pmatrix}\cos 2\theta & \sin 2\theta \\ \sin 2\theta & -\cos 2\theta\end{pmatrix} = \frac{1}{S}\mathbf{Q}$$

$$\boldsymbol{\pi} = \begin{pmatrix}-\sin 2\theta & \cos 2\theta \\ \cos 2\theta & \sin 2\theta\end{pmatrix} = \frac{1}{2}\frac{d}{d\theta}\sigma_{\mathbf{p}}$$

Differentiating $\mathbf{Q}$, we obtain: $\frac{d\mathbf{Q}}{dt} = \frac{d}{dt}(S\boldsymbol{\sigma_p}) = \frac{dS}{dt}\boldsymbol{\sigma_p} + 2S\frac{d\theta}{dt}\boldsymbol{\pi}$. If we multiply this equation by $\boldsymbol{\sigma_p}$ and take the trace, we can isolate $\frac{dS}{dt}$.[9]

$$\begin{aligned}\operatorname{tr}\left[\boldsymbol{\sigma_p}\frac{d\mathbf{Q}}{dt}\right] &= \operatorname{tr}\left[\boldsymbol{\sigma_p}\frac{dS}{dt}\boldsymbol{\sigma_p} + \boldsymbol{\sigma_p}2S\frac{d\theta}{dt}\boldsymbol{\pi}\right] \\ &= \frac{dS}{dt}\operatorname{tr}\left[\boldsymbol{\sigma_p}\boldsymbol{\sigma_p}\right] + 2S\frac{d\theta}{dt}\operatorname{tr}\left[\boldsymbol{\sigma_p}\boldsymbol{\pi}\right] \\ &= 2\frac{dS}{dt}\end{aligned}$$

Applying this identity to equation 1.9 yields

$$\begin{aligned}2(\partial_t + \vec{v}\cdot\nabla)S &= \operatorname{tr}\left(2\xi\boldsymbol{\sigma_p}\mathbf{u} + \boldsymbol{\sigma_p}\boldsymbol{\omega}\mathbf{Q} - \boldsymbol{\sigma_p}\mathbf{Q}\boldsymbol{\omega} + \Gamma\boldsymbol{\sigma_p}\mathbf{H}\right) \\ &= \operatorname{tr}\left(2\xi\frac{1}{S}\mathbf{Q}\mathbf{u} + \frac{1}{S}\mathbf{Q}\boldsymbol{\omega}\mathbf{Q} - \frac{1}{S}\mathbf{Q}\mathbf{Q}\boldsymbol{\omega} + \Gamma\frac{1}{S}\mathbf{Q}\mathbf{H}\right) \\ &= \frac{2\xi}{S}\operatorname{tr}(\mathbf{Q}\mathbf{u}) + \frac{1}{S}\operatorname{tr}(\mathbf{Q}\omega\mathbf{Q}) - \frac{1}{S}\operatorname{tr}(\mathbf{Q}\mathbf{Q}\omega) + \frac{\Gamma}{S}\operatorname{tr}(\mathbf{Q}\mathbf{H}) \\ &= \frac{2\xi}{S}\operatorname{tr}(\mathbf{Q}\mathbf{u}) + \frac{\Gamma}{S}\operatorname{tr}(\mathbf{Q}\mathbf{H}) \qquad (1.10)\end{aligned}$$

Notice that the thermodynamic term, $\frac{\Gamma}{S}\operatorname{tr}(\mathbf{QH})$, does not depend explicitly on $\vec{v}$. Moreover, it is possible to construct velocity fields that cause the shear term, $\frac{2\xi}{S}\operatorname{tr}(\mathbf{Qu})$, to grow

[9] Similarly, we can isolate $\frac{d\theta}{dt}$ by multiplying by $\boldsymbol{\pi}$.

arbitrarily large. In such a case, there is nothing to guarantee that S will remain bounded. The S in the denominator does not help in this regard, as it cancels with the factor of S in the definition of $\mathbf{Q}$. Expanding the shear term, we obtain:

$$\frac{2\xi}{S}\text{tr}[\mathbf{Qu}] = 2\xi\cos(2\theta)(\partial_x v_x - \partial_y v_y) + 2\xi\sin(2\theta)(\partial_x v_y + \partial_y v_x)$$

For completeness, let us construct an explicit example. Consider a horizontally aligned liquid crystal, $\theta = 0$, that fills the xy-plane, subject to the velocity field $\vec{v} = [Ax, 0]^{\text{T}}$. It is easy to verify that such a liquid crystal will remain horizontally aligned. However, substituting $\vec{v}$ into the expression above yields:

$$\begin{aligned}\frac{2\xi}{S}\text{tr}[\mathbf{Qu}] &= 2\xi\cos(0)(\partial_x(Ax) - \partial_y 0) + 2\xi\sin(0)(\partial_x 0 + \partial_y Ax) \\ &= 2\xi A\end{aligned}$$

Thus, S will become larger than one provided that A is large enough to overcome the effects of the thermodynamic terms. Restricting ourselves to divergence-free velocity fields does not help; we observe the same behaviour with $\vec{v} = [Ax, -Ay]^{\text{T}}$ provided we drop the diffusion terms.

We can see hints of this problem throughout the literature. In [69], Volson *et al.* apply the Olmsted-Goldbart equations to study bacterial dynamics, but note in their supplementary material that dropping the thermodynamic terms causes S to exceed one.

By contrast, when we apply the same decoupling procedure to the Beris-Edwards equation, 1.8, we obtain the following:

$$\begin{aligned}2(\partial_t + \vec{v}\cdot\nabla)S &= \text{tr}\left(2\xi\boldsymbol{\sigma_p}\mathbf{u} + \boldsymbol{\sigma_p}\boldsymbol{\omega}\mathbf{Q} - \boldsymbol{\sigma_p}\mathbf{Q}\boldsymbol{\omega} - \boldsymbol{\sigma_p}\xi\text{tr}(\mathbf{Qu})\mathbf{Q} + \Gamma\boldsymbol{\sigma_p}\mathbf{H}\right) \\ &= \text{tr}\left(2\xi\frac{1}{S}\mathbf{Qu} + \frac{1}{S}\mathbf{Q}\boldsymbol{\omega}\mathbf{Q} - \frac{1}{S}\mathbf{QQ}\boldsymbol{\omega} - \frac{1}{S}\mathbf{Q}\xi\text{tr}(\mathbf{Qu})\mathbf{Q} + \Gamma\frac{1}{S}\mathbf{QH}\right) \\ &= \frac{2\xi}{S}\text{tr}(\mathbf{Qu}) + \frac{1}{S}\text{tr}(\mathbf{Q}\omega\mathbf{Q}) - \frac{1}{S}\text{tr}(\mathbf{QQ}\omega) - \frac{\xi}{S}\text{tr}(\mathbf{Qu})\text{tr}(\mathbf{QQ}) + \frac{\Gamma}{S}\text{tr}(\mathbf{QH}) \\ &= \frac{2\xi}{S}(1 - S^2)\text{tr}(\mathbf{Qu}) + \frac{\Gamma}{S}\text{tr}(\mathbf{QH})\end{aligned}$$

Unlike in Equation 1.10, the factor of $1 - S^2$ causes the shear terms to vanish as S approaches 1, as desired.

1.2.4 Defects and Charge Density

We conclude this section with a brief discussion of topological defects. Topological defects are points of discontinuity in the director field of a liquid crystal. From a purely mathematical perspective, these defects are important because they cannot be removed using continuous deformations, and thus they serve to characterize the qualitative/topological properties of a given liquid crystal configuration. In effect, they reduce the continuum description of a liquid crystal (the description in terms of field variables) into a discrete description characterizing the liquid crystal using a finite number of points. Studying the behaviour of topological defects acts as a convenient proxy for studying liquid crystals as a whole. We will adopt this approach in sections 4.3.1 and 4.3.2.

Given a Q-tensor, we may calculate the location of topological defects by finding peaks in the charge density [11]:

$$\partial_x(Q_{11}/S)\partial_y(Q_{12}/S) - \partial_x(Q_{12}/S)\partial_y(Q_{11}/S) \tag{1.11}$$

See Figure 1.5 for an example.

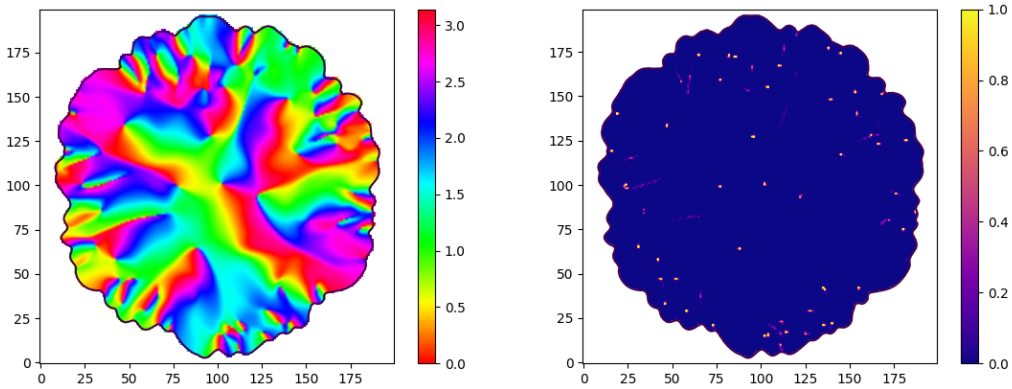

(a) Angle

(b) Charge density

Figure 1.5: Plot (a) depicts the director field for a (simulated) microcolony, using colour to visualize the angle of the director. Plot (b) depicts the corresponding charge density, as calculated by Equation 1.11. (The details of the underlying simulation will by given in Chapter 3.)

1.3 Previous Models

This thesis attempts to combine two families of mathematical models: incompressible models, where cell motion is driven entirely by growth, and liquid crystal models, where cell motion is driven by gradients in the relevant field variables.

Incompressibility is routinely assumed throughout the microcolony/biofilm modeling literature, not only in fluid-inspired models, but also in diffusion models such as [28].[10] As such, there is no coherent or self-contained literature on the subject, and a comprehensive review would be quite impossible. Instead, we will point to one line of research that has served as important inspiration for our work: the study of fingering instabilities in bacterial colonies undergoing nutrient-limited growth [42][27][38][33].

Very briefly (we will unpack this derivation in more detail in Chapter 2), these models begin with a (sometimes implicit, as in [42]) continuity equation for bacterial density:

$$\partial_t b + \nabla \cdot (b\vec{v}) = g \tag{1.12}$$

The term g in the above is a growth term, and $\vec{v}$ is the average velocity of the bacteria. Assuming incompressibility, i.e. $\partial_t b + \vec{v} \cdot \nabla b = 0$, equation 1.12 simplifies to $\nabla \cdot \vec{v} = g/b$.

These models then assume that $\vec{v}$ satisfies Darcy's law, $\vec{v} = -A\nabla p$, which, when combined with the incompressibility condition above, yields $-A\Delta p = g/b$. It is this equation that determines the velocity of the bacteria.

This core model is then extended by making g depend on a nutrient field, which is governed by its own set of equations. This line of research then proceeds to study the interplay between bacterial motion and nutrient depletion. We will not be pursuing such questions in this thesis.

In contrast to the sprawling zoo of incompressible models, there is self-contained literature on Beris-Edwards-type models for bacterial growth. These models are typically variations on the following system of PDEs:

$$\partial_t b + \nabla \cdot (b\vec{v}) = \lambda b \tag{1.13}$$

$$b(\partial_t + \vec{v} \cdot \nabla)\vec{v} = \nabla \cdot \boldsymbol{\sigma} - \mu b\vec{v} \tag{1.14}$$

$$(\partial_t + \vec{v} \cdot \nabla)Q_{\alpha\beta} = 2\xi u_{\alpha\beta} - \xi \mathrm{tr}(\mathbf{uQ})Q_{\alpha\beta} + \omega_{\alpha\gamma}Q_{\gamma\beta} - Q_{\alpha\gamma}\omega_{\gamma\beta} + \Gamma H_{\alpha\beta} \tag{1.15}$$

[10] It was shown in [41] that this diffusion model can be derived as the continuum limit of a discrete model in which one assumes that each point in space can contain only a finite amount of biomass.

From equation 1.14, we see that the only body force acting on the system is friction. The rest of the motion is governed by stress, which appears under a gradient. In particular, this means that only gradients of $\mathbf{Q}$, and not $\mathbf{Q}$ itself, will impact the colony's morphology.

In the following sections, we will summarize some foundational models from the current literature. In what follows, we have changed the notation used by the original authors (renaming constants and variables) for ease of readability and so that comparisons may be draw more easily.

1.3.1 Volfson *et al.*

The earliest example we are aware of for hydrodynamic Q-tensor models being applied to bacterial growth is the the 2008 paper by Volfson *et al.* [69]. In this paper, Volfson *et al.* demonstrate that monolayers of *E. coli* grown in semi-confined environments underwent a transition from a disordered state to one where all the cells were oriented in the same direction, and they investigate this behaviour with a PDE model.

They begin their model development with the Olmsted and Goldbart equation, 1.9, reviewed above, and a Cauchy momentum equation for velocity.

$$\begin{aligned}(\partial_t + \vec{v}\cdot\nabla)Q_{\alpha\beta} &= \xi u_{\alpha\beta} + \omega_{\alpha\gamma}Q_{\gamma\beta} - Q_{\alpha\gamma}\omega_{\gamma\beta} + \Gamma H_{\alpha\beta}\\ (\partial_t + \vec{v}\cdot\nabla)(bv_\alpha) &= \partial_\beta\sigma_{\alpha\beta} - \mu b v_\alpha\end{aligned}$$

Volfson *et al.* extend this by adding a third equation to model the evolution of density, including a growth term:

$$\partial_t b + \nabla\cdot(b\vec{v}) = \lambda b$$

So far, this model appears largely identical to equations 1.13-1.15, minus the trace term in the Beris-Edwards equation. There is another important difference: the $\boldsymbol{u}$ in their equations is not the trace-free version we have described previously, but rather the more traditional $u_{\alpha\beta} = (\partial_\beta v_\alpha + \partial_\alpha v_\beta)/2$, which does not preserve the trace-free property of $\mathbf{Q}$.

From this starting point, Volfson *et al.* apply a number of simplifications. They drop all thermodynamic terms (i.e. they drop all terms which depend on the free energy), and they set $\sigma_{\alpha\beta} = -p\delta_{\alpha\beta}$, where p is a pressure. Moreover, they assume p takes the form $p = p_0\exp(s(b-b_p))$, where b_p is the packing density and s is a model parameter controlling the steepness of p.

At this point in the derivation, they note that there is nothing in the equations that guarantees that $S < 1$.[11] They address this by multiplying the RHS of their Q-tensor equation by $1 - S^2$.

Thus, their model reads:

$$\begin{aligned} \partial_t b + \nabla \cdot (b\vec{v}) &= \lambda b \\ (\partial_t + \vec{v} \cdot \nabla)(bv_\alpha) &= -\partial_\alpha p - \mu b v_\alpha \\ (\partial_t + \vec{v} \cdot \nabla)Q_{\alpha\beta} &= (1 - S^2)\left(\xi u_{\alpha\beta} + \omega_{\alpha\gamma}Q_{\gamma\beta} - Q_{\alpha\gamma}\omega_{\gamma\beta}\right) \end{aligned}$$

Ultimately, Volfson *et al.* go on to simplify these equations further to obtain a 1-dimensional model representing growth in a straight open channel. They confirm that this model exhibits the same self-organizing behaviour that they observed in experiments.

1.3.2 Dell'Arciprete *et al.* and You *et al.*

In 2018, a pair of papers were published by Dell'Arciprete *et al.* [21] and You *et al.* [72] which expanded on the model proposed by Volfson *et al.* in several important ways.

Both papers model density using 1.13, though You *et al.* introduce a small diffusion term for regularization, $\partial_t b + \nabla \cdot (b\vec{v}) = \lambda b + D\Delta b$. Like Volfson *et al.*, the starting point for velocity evolution in Dell'Arciprete *et al.*'s and You *et al.*'s models is a Cauchy momentum equation with friction, as in 1.14. The specifics of the two models, however, are slightly different.

Dell'Arciprete *et al.* drop the inertial terms, which results in $\partial_\beta \sigma_{\alpha\beta} = \mu b v_\alpha$. Much like Volfson *et al.*, they ignore potential thermodynamic contributions and impose a relatively simple constitutive relation to close the system, though theirs is slightly more general:

$$\sigma_{\alpha\beta} = -p\delta_{\alpha\beta} - aQ_{\alpha\beta}$$

Here, $p = p_0 \max[(b/b_p - 1), 0]$ is a pressure term, and $a = a_0 b$ is proportional to density. Unlike Volfson *et al.*, the addition of the second term on the RHS introduces a coupling to the order parameter.

By contrast, You *et al.* keep the inertial terms[12] and introduce a much more general constitutive relation:

$$\sigma_{\alpha\beta} = -p\delta_{\alpha\beta} + aQ_{\alpha\beta} - \xi S H_{\alpha\beta} + Q_{\alpha\gamma}H_{\gamma\beta} - H_{\alpha\gamma}Q_{\gamma\beta}$$

[11] They attribute this to the lack of thermodynamic terms, though, as we have seen, this problem occurred much earlier.

[12] They do examine the non-inertial case in a later section of their paper.

You *et al.* choose $p = p_0 \left(\frac{b}{b_p} - 1\right)$ and $a = -a_0 \left(\frac{b}{b_p} - 1\right)$, continuing with the assumption that pressure is driven by density gradients.

Note that, despite their superficial differences, the pressure terms in these three models are very similar in spirit. They all assume that pressure will be low when density is below the packing density, b_p, and will rise above it.

When it comes to the Q-tensor dynamics, both Dell'Arciprete *et al.* and You *et al.* use the Olmstead-Goldbart equation, though they do improve over Volfson *et al.*'s model by using the trace-free version of $\mathbf{u}$.

Dell'Arciprete *et al.* and You *et al.* also differ significantly from Volfson *et al.* in terms of the behaviour they study. Whereas Volfson *et al.* was concerned with bacterial monolayers growing in a confined environment, Dell'Arciprete *et al.* and You *et al.* examine the dynamics of a freely expanding monolayer.

You *et al.* analyze the dynamics of expanding microcolonies by observing that cells tend to cluster into distinct patches with a well-defined local orientation. They observed that the size of these patches is distributed exponentially, and they identify K, the diffusion constant in the Q-tensor equation, as a key parameter controlling this size distribution.

Dell'Arciprete *et al.* focus not on ordered patches, but on the topological defects that form when such patches meet. They find that these topological defects are produced at a constant rate, and that they are produced within the bulk of the microcolony, not at its boundary.

Dell'Arciprete *et al.* plays a particularly important role in the context of this thesis because they were the first to single out growth-induced expansion as the key mechanism driving the physics of microcolonies. They analogized this to the expansion of space-time, and dubbed their system a "Hubble active nematic." Indeed, in the first section of their paper, they even consider an incompressible growth model that would center this Hubble mechanism, though they eventually discard it in favour of the model described above. This thesis can be seen as a continuation of that initial premise.

1.3.3 Doostmohammadi *et al.*

No discussion of this field would be complete without mentioning the work of Amin Doostmohammadi, who has published, along with his many collaborators, extensive and diverse papers in this area, including several review articles [23] [24] [4]. This work is too vast to describe in its entirety, but we will highlight some key results and modelling choices.

The first notable difference is that, in contrast to the models we have described so far, Doostmohammadi *et al.*'s models typically track the total density, including the surrounding fluid, nutrients, etc. and the velocity in their models represents the average velocity of the total fluid mass, which they typically assume to be conserved and incompressible. They represent the cell density as a fraction of the total density.

For example, in [25], their model reads:

$$\begin{aligned}
\partial_t b + \nabla \cdot (b\vec{v}) &= \lambda b + \kappa \Delta b \\
\partial_t \rho + \nabla \cdot (\rho \vec{v}) &= 0 \\
\rho(\partial_t + \vec{v} \cdot \nabla)\vec{v} &= \nabla \cdot \boldsymbol{\sigma} \\
(\partial_t + \vec{v} \cdot \nabla)Q_{\alpha\beta} &= (\xi u_{\alpha\gamma} + \omega_{\alpha\gamma})(Q_{\gamma\beta} + \delta_{\gamma\beta}/3) + (Q_{\alpha\gamma} + \delta_{\alpha\gamma}/3)(\xi u_{\gamma\beta} - \omega_{\gamma\beta}) \\
&\quad - 2\xi(Q_{\alpha\beta} + \delta_{\alpha\beta}/3)\mathrm{tr}(\mathbf{Qu}) + \Gamma H_{\alpha\beta}
\end{aligned}$$

Here, ρ is the total density. The cell density, b, is coupled to the rest of the system via their definition of $\mathbf{H}$, which they take to be $H_{\alpha\beta} = A_0 S^2(1-b)Q_{\alpha\beta} + K\Delta Q_{\alpha\beta}$.

The next thing to note is that Doostmohammadi *et al.* have in various papers used the Beris-Edwards equation, and not the Olmstead-Goldbart equation, to model Q-tensor dynamics (e.g. in [23]). However, this usage has not been consistent (e.g. [26] uses the Olmstead-Goldbart equation), and in some cases, they have cited the 3-dimensional Beris-Edwards equation when studying a 2-dimensional system, as in the model from [25] which we reproduced above.

Also noteworthy is the fact that Doostmohammadi *et al.* have demonstrated that Q-tensor theories can usefully describe the dynamics of mammalian cells [25][60]. This is because mammalian cells, despite their relatively symmetric shape, exert asymmetric forces on the surrounding tissue when they undergo cell division. Such work extends the potential scope of this research beyond microbiology and into such areas as wound healing and tumor growth.

Restricting our attention to bacterial cells, Doostmohammadi *et al.* have used insights from liquid crystal theory to arrive at several interesting and surprising results. In [49], they showed that, in crowded environments, slow-moving bacteria can out-compete their faster counterparts because excessive motility is a barrier to collective motion. In [26] they showed that topological defects interact with the boundary of a growing microcolony, resulting in changes in the microcolony's morphology.

1.3.4 Shortcomings

The work of Volfson *et al.*, Dell'Arciprete *et al.*, You *et al.*, and Doostmohammadi *et al.* have helped inspire a flurry of research. At time of writing, Doostmohammadi *et al.*'s 2018 review article on active nematics [23] has amassed some 400+ citations. Much of this work has been devoted to studying the behaviour of the models we have already discussed. See, for example, the work of Basaran *et al.* [5] studying the growth of annulus-shaped microcolonies, or the wide-ranging investigation of active nematics given in a recent PhD thesis by Prashant Mishra [50].

However, it seems to us that these models are not sufficient to describe the behaviour of growing bacteria. When we consider the dynamics of $\vec{v}$, we see that these models only differ from the traditional hydrodynamic models of passive liquid crystals by the presence of an active stress term, $a\mathbf{Q}$, which appears in $\boldsymbol{\sigma}$. In Equation 1.14, this term appears under a gradient, which means that a spatially homogeneous microcolony will not experience any forces due to growth.

As a thought experiment, consider a microcolony of uniform density where all the cells are aligned horizontally. What kind of motion should we expect from such a microcolony? Clearly, there ought to be a contribution from the Q-tensor. As the cells grow, they will push on their neighbours, exerting their influence most strongly in the horizontal direction. However, the models above predict no such effect. In the absence of any spatial gradients, the only force acting on the system is friction.

In this thesis, we will propose an alternative to the active stress term employed by previous models, an alternative that does not rely on spatial gradients. To this end, we will revisit the Hubble analogy proposed by Dell'Arciprete *et al.* If a microcolony is like a miniature expanding universe, what happens if this expansion is not uniform in space? How would we model this, and what behaviours would such a microcolony exhibit? These are the questions we seek to answer.

Chapter 2

Model Formulation

Our goal in this chapter is to develop an alternative description of active nematics that does not rely on gradients in the field variables to drive the dynamics of the system. To this end, we will focus only on the expansive forces that result from the interplay between growth and incompressibility, temporarily setting aside all other forces that could be acting on the system.

2.1 Uniform Spread

We would like to obtain a model of microcolony dynamics in which cell motion results directly from growth. To simplify matters, we first consider the case where cells spread uniformly, independent of their orientation.

We return to Equation 1.13, the continuity equation for bacterial density undergoing exponential growth. We wish to solve this equation on a bounded domain, $D \subset \mathbb{R}^d$ with $d = 1, 2$.[1] The boundary of the domain is divided into two sections, $\partial D = \Gamma_{D,w} \cup \Gamma_{D,o}$, where $\Gamma_{D,w}$ represents solid walls, and $\Gamma_{D,o}$ represents open boundaries. We assume that matter can leave the domain through the open boundary, but not enter it.[2]

Equation 1.13 can be rewritten as follows:

$$(\partial_t + \vec{v} \cdot \nabla) b = (\lambda - \nabla \cdot \vec{v})\, b \tag{2.1}$$

[1] The case $d = 3$ is significantly more complicated. For one thing, we must consider how gravity impacts the dynamics. Moreover, much of the relevant physics, such as those governing the planar-to-bulk transition, are driven by elastic forces which our incompressible model neglects. See, e.g., [9][36][73][48].

[2] This replicates the behaviour of an idealized microchemostat as in, e.g., Figure 1.1.

The LHS of this equation is the material derivative of density, which represents the rate of change we would observe using a frame of reference that moves with velocity $\vec{v}$ (in contrast to $\partial_t b$, which represents the rate of change at a fixed point).

We reason as follows: cell density at a point represents the average cell volume over some suitably small region of space (large enough to capture many cells, but not so large as to lose all spatial information). When the cells are not densely packed, the only motion comes from cells nudging their neighbours as they grow. This motion will be on a much smaller scale than the region over which we are averaging. Moreover, we have no *a priori* reason to expect this small-scale motion to have any preferred direction. For these reasons, we expect the macroscopic, averaged motion to be zero when cell density is below the packing density, b_p.[3] Conversely, when the packing density is reached, we expect the colony to act as an incompressible fluid; once the cells reach the packing density, they will remain at packing density. In this case, the material derivative is zero. This gives, from equation 2.1, $(\partial_t + \vec{v} \cdot \nabla)b = 0 \implies \nabla \cdot \vec{v} = \lambda$, which leads to the system:

$$\begin{aligned} \partial_t b + \nabla \cdot (b\vec{v}) &= \lambda b \\ \nabla \cdot \vec{v} &= \lambda \qquad \text{when } b = b_p \\ \vec{v} &= 0 \qquad \text{when } b < b_p \end{aligned}$$

We are now faced with a problem. The equations above do not specify a unique velocity profile.

We can make some headway towards addressing this issue by imposing boundary conditions. Let $\Omega \subset D$ be the subset of the domain where $b = b_p$ (we will refer to this as the *close-packed region*). We split the boundary of Ω into two disjoint subsets, $\partial\Omega = \Gamma_{\Omega,w} \cup \Gamma_{\Omega,f}$, where $\Gamma_{\Omega,w} = \partial\Omega \cap \Gamma_{D,w}$ are walls and $\Gamma_{\Omega,f}$ are open/free boundaries. We will require that $\Gamma_{\Omega,f}$ be non-empty.[4] There is no flow through walls, i.e. $\vec{v} \cdot \hat{n} = 0$, where $\hat{n}$ is the outward-pointing vector normal to $\Gamma_{D,w}$. In other words, we expect the velocity field to solve the

[3] The packing density is the density at which no more bacteria can be added to a region without compressing the cells. In general, this is a function of cell shape, and it will fluctuate slightly as cells grow and divide, but for simplicity we will take it to be a constant.

[4] If the close-packed region is bounded on all sides by walls, there is nowhere for new cell matter to go. Mathematically, this manifests as a contradiction when we try to apply the divergence theorem:

$$\lambda|\Omega| = \int_\Omega \lambda dA = \int_\Omega \nabla \cdot \vec{v} dA = \int_{\partial\Omega} \vec{v} \cdot \hat{n} ds = \int_{\Gamma_{\Omega,w}} \vec{v} \cdot \hat{n} ds = 0$$

In the real world, this would be resolved by, e.g., a cessation of growth or by buckling into the third dimension.

following Poisson problem:

$$\begin{aligned} \nabla \cdot \vec{v} &= \lambda \qquad \text{on } \Omega \\ \vec{v} \cdot \hat{n} &= 0 \qquad \text{on } \Gamma_{\Omega,w} \end{aligned} \tag{2.2}$$

Unfortunately, this is not enough to specify a unique solution. For any $\vec{v}$ satisfying 2.2, we can add a divergence-free vector field (provided it also has no flux on the walls) and obtain another solution. Moreover, there is no simple boundary condition we can impose on the open boundary, $\Gamma_{\Omega,f}$. We must look elsewhere for additional constraints.

In one dimension, we can argue by symmetry. Here, close-packed regions are intervals, and the equation for velocity reduces to $\partial_x v = \lambda \implies v = \lambda x + v_0$. If the close-packed region is bounded on one side by a wall, that boundary condition is enough to uniquely determine v_0. If the close-packed region has two free boundaries, then by symmetry the velocity must have equal magnitude at both boundaries (equivalently, the velocity is zero in the middle of the interval), which is again enough to specify a unique solution.

The two dimensional case is more complicated,[5] and requires assumptions stronger than simple symmetry. In Duddu *et al.*'s incompressible model of nutrient-limited growth [27], a unique solution is obtained by assuming that the velocity field is irrotational. This implies the velocity has a scalar potential, $\vec{v} = -\nabla p$. They further assume that $p = 0$ on $\Gamma_{\Omega,f}$, so that setting $p = 0$ on the rest of the domain yields a continuous function. This is enough to guarantee that the velocity, if one exists, is unique. However, these assumptions do not suggest any way to modify the system to account for cell orientation, and it is not clear why the boundary condition on p is physically appropriate.

We propose an alternative: choose the velocity that minimizes the total kinetic energy, $K(\vec{v}) = \frac{1}{2} b_p \int_\Omega \vec{v} \cdot \vec{v}\, dA$. To avoid having to qualify all future statements, we will restrict K to be defined on the set of solutions to 2.2. Thus, when we talk about, e.g., stationary points of K, we refer to stationary points on the set of solutions to 2.2.

We will show in Proposition 2.1.4 that minimizing K is equivalent to the choice made by [27]. Crucially, this formulation will later allow us to modify the system to account for the effects of cell orientation.

We begin by characterizing the stationary points of K. We add a divergence free vector

[5] Indeed, this is precisely where Dell'Arciprete *et al.* [21] pivot away from their "Hubble flow" mechanism and adopt an elastic model.

field, $\vec{u}$, with $\vec{u} \cdot \hat{n} = 0$ on $\Gamma_{\Omega,w}$.

$$\begin{aligned} K_\epsilon &\equiv K(\vec{v} + \epsilon\vec{u}) \\ &= \frac{1}{2} b_p \int_\Omega (\vec{v} + \epsilon\vec{u}) \cdot (\vec{v} + \epsilon\vec{u}) dA \\ &= \frac{1}{2} b_p \int_\Omega (\vec{v} \cdot \vec{v} + 2\epsilon\vec{v} \cdot \vec{u} + \epsilon^2 \vec{u} \cdot \vec{u}) dA \end{aligned}$$

Therefore the functional derivative of K is given by:

$$\lim_{\epsilon \to 0} \left(K_\epsilon - K(\vec{v}) \right) / \epsilon = b_p \int_\Omega \vec{v} \cdot \vec{u} dA$$

Thus, we have the following:

Proposition 2.1.1. *The vector field $\vec{v}$ is a stationary point of K iff $\int_\Omega \vec{v} \cdot \vec{u} dA = 0$ for every divergence-free vector field $\vec{u}$ with $\vec{u} \cdot \hat{n} = 0$ on $\Gamma_{\Omega,w}$.*

However, we can make a stronger claim: any solution satisfying the condition in Proposition 2.1.1 is a global minimum of K. To show this, we will prove that K is a strictly convex functional evaluated on a convex set. We begin with the latter claim.

Proposition 2.1.2. *The set of vector fields satisfying 2.2 is convex.*

Proof. Suppose $\vec{v}_1$ and $\vec{v}_2$ are two solutions to 2.2. Then their difference, $\vec{w} = \vec{v}_1 - \vec{v}_2$, satisfies:

$$\begin{aligned} \nabla \cdot \vec{w} &= 0 \qquad \text{on } \Omega \\ \vec{w} \cdot \hat{n} &= 0 \qquad \text{on } \Gamma_{\Omega,w} \end{aligned} \tag{2.3}$$

In other words, all solutions of 2.2 can be written in the form $\vec{v}_1 + \vec{w}$, where $\vec{v}_1$ is a particular solution and $\vec{w}$ satisfies (2.3). To see that this set is convex, we will take a convex combination and show that it remains within the set. Let $\vec{v}_2 = \vec{v}_1 + \vec{w}_2$ and $\vec{v}_3 = \vec{v}_1 + \vec{w}_3$ be two solutions to 2.2, and let t be a real number with $0 < t < 1$.

$$\begin{aligned} t\vec{v}_2 + (1-t)\vec{v}_3 &= t\vec{v}_1 + t\vec{w}_2 + (1-t)\vec{v}_1 + (1-t)\vec{w}_3 \\ &= \vec{v}_1 + (t\vec{w}_2 + (1-t)\vec{w}_3) \end{aligned}$$

By the linearity of ∇ and the bilinearity of the dot product, the vector field $t\vec{w}_2 + (1-t)\vec{w}_3$ satisfies (2.3), and therefore $t\vec{v}_2 + (1-t)\vec{v}_3$ satisfies 2.2, as desired. □

Proposition 2.1.3. *The functional K is strictly convex.*

Proof. We let $\vec{v}$ and $\vec{u}$ be two vector fields, and let t again be a real number satisfying $0 \leq t \leq 1$. We wish to show that

$$tK(\vec{v}) + (1-t)K(\vec{u}) \geq K(t\vec{v} + (1-t)\vec{u}).$$

with equality iff $t = 0$ or $t = 1$.

To simplify the argument, we will instead prove the equivalent statement:

$$tK(\vec{v}) + (1-t)K(\vec{u}) - K(t\vec{v} + (1-t)\vec{u}) \geq 0.$$

We expand $K(t\vec{v} + (1-t)\vec{u})$ using the definition of K, and rearrange.

$$\begin{aligned} tK(\vec{v}) + (1-t)K(\vec{u}) - K(t\vec{v} + (1-t)\vec{u}) &= tK(\vec{v}) + (1-t)K(\vec{u}) \\ &\quad - t^2K(\vec{v}) - (1-t)^2K(\vec{u}) \\ &\quad - 2t(1-t)b_p \int_\Omega \vec{v}\cdot\vec{u}dA \\ &= t(1-t)\left(K(\vec{v}) - 2b_p\int_\Omega \vec{v}\cdot\vec{u}dA + K(\vec{u})\right) \\ &= t(1-t)K(\vec{v}-\vec{u}) \end{aligned}$$

Because the dot product satisfies $(\vec{v}-\vec{u})\cdot(\vec{v}-\vec{u}) \geq 0$, and only vanishes when $\vec{v} = \vec{u}$, and because $0 \leq t \leq 1$, the result follows. □

Thus, because K is a strictly convex functional evaluated on a convex set, it has a single stationary point, and that stationary point is a global minimum.

So far we have shown that if solutions exists to equations (2.2), then minimizing K is enough to specify a unique velocity field. Moreover, the velocity field in question will satisfy $\int_\Omega \vec{v}\cdot\vec{u}dA = 0$ for every divergence-free vector field $\vec{u}$ that satisfies equations (2.3). We will now show that this condition is equivalent to the conditions defined by Duddu *et al.* in [27].

Proposition 2.1.4. *Suppose there exists*[6] *a function p that solves the following Poisson problem:*

$$\begin{aligned} \Delta p &= -\lambda \quad && \text{on } \Omega \\ p &= 0 && \text{on } \Gamma_{\Omega,f} \\ \nabla p\cdot\hat{n} &= 0 && \text{on } \Gamma_{\Omega,w} \end{aligned} \tag{2.4}$$

[6] Existence is addressed at the end of section 2.3.

Then the velocity field $\vec{v} = -\nabla p$ satisfies 2.2. Moreover, this choice of $\vec{v}$ is the unique solution of 2.2 that minimizes the kinetic energy.

Proof. It is clear that $\vec{v}$ satisfies 2.2. Recall that $\vec{v}$ is a minimum of K if $\int_\Omega \vec{v} \cdot \vec{u} dA = 0$ for every vector field $\vec{u}$ satisfying 2.3. A direct computation using 2.4 yields:

$$\begin{aligned}
\int_\Omega \vec{v} \cdot \vec{u}\, dA &= -\int_\Omega \nabla p \cdot \vec{u}\, dA \\
&= -\int_\Omega \left(\nabla \cdot (p\vec{u}) - p\nabla \cdot \vec{u}\right)\, dA \\
&= -\int_{\partial\Omega} p\vec{u} \cdot \hat{n}\, ds + \int_\Omega p\nabla \cdot \vec{u}\, dA \qquad \text{by the divergence theorem} \\
&= -\int_{\Gamma_{\Omega,w}} p\vec{u} \cdot \hat{n}\, ds - \int_{\Gamma_{\Omega,f}} p\vec{u} \cdot \hat{n}\, ds + \int_\Omega p\nabla \cdot \vec{u}\, dA \\
&= 0
\end{aligned}$$

The first integral vanishes because $\vec{u} \cdot \hat{n} = 0$ on walls, the second because $p = 0$ on free/open boundaries, and the third because $\vec{u}$ is divergence-free. □

Combining Equation 1.13 with Proposition 2.1.4, we arrive at the following system:

$$\begin{aligned}
\partial_t b + \nabla \cdot (b\vec{v}) &= \lambda b \\
\vec{v} &= \begin{cases} -\nabla p & \text{on } \Omega \\ 0 & \text{on } D \setminus \Omega \end{cases} \\
\Delta p &= -\lambda \qquad \text{on } \Omega \\
p &= 0 \qquad \text{on } \Gamma_{\Omega,f} \\
\nabla p \cdot \hat{n} &= 0 \qquad \text{on } \Gamma_{\Omega,w}
\end{aligned} \tag{2.5}$$

We can interpret the function p as a pressure. If we were to model the velocity using a Cauchy momentum equation where the only forces are pressure and friction, we might obtain an equation like: $b\frac{D\vec{v}}{Dt} = -\nabla\tilde{p} - \mu\vec{v}$, where μ is a coefficient of friction. Dropping the inertial terms, we obtain a balance of forces between friction and pressure: $\mu\vec{v} = -\nabla\tilde{p}$. Incompressibility fixes $\mu\lambda = -\Delta\tilde{p}$. Finally, rescaling the pressure using $p = \frac{\tilde{p}}{\mu}$, we recover the formulation of $\vec{v}$ above (though further assumptions are required to derive the associated boundary conditions).

Again, we wish to emphasize that Equations 2.5 are not themselves novel. As we discussed in the introduction, [27] and others have extended this basic model by making the growth rate, λ, a function of nutrient. At this point, it may appear that we have done nothing but complicated the derivation. The advantages of the kinetic energy formulation will become clearer in Section 2.3, when we use it to derive a model that couples velocity to cell orientation. Before we do so, we will briefly examine how Equations 2.5 behave in one dimension.

2.2 The 1D Model

To better understand the behaviour of equations 2.5, we return to the 1-dimensional case we briefly discussed early in Section 2.1. In this case, we can fully describe the solutions of the system.

The close-packed region, Ω, consists of disjoint intervals. Outside of these intervals, the evolution equation for density reduces to $\partial_t b = \lambda b$, which has the closed-form solution $b(x,t) = b(x,0)e^{\lambda t}$. In these regions, the velocity is zero, and pressure is left undefined by Equations 2.5.[7]

On the interior of the close-packed intervals, the material derivative of density is zero, and thus the density remains constant, $b = b_p$.[8] On each of these close-packed intervals, say $[x_1, x_2]$, the pressure is $p = -\frac{\lambda}{2}(x - x_1)(x - x_2)$, therefore the velocity is $v = \frac{\lambda}{2}(x - x_1) + \frac{\lambda}{2}(x - x_2)$.

The only part of the solution left to characterize is the evolution of the boundary that separates the close-packed region from the rest of the domain. In one dimension, this boundary is a collection of isolated points, the boundary points of the close-packed intervals.

Without loss of generality, let $[x_0, x_1]$ be an interval containing a single such boundary point, $x_0 < x_b(t) < x_1$, such that $b(x,t) < b_p$ for $x_0 < x < x_b(t)$ and $b(x,t) = b_p$ for

[7] If we want the pressure to be a continuous function defined on the entire domain, we may define pressure to be 0 outside the close-packed region. This, however, is not required.

[8] While it is possible to contrive initial conditions where $b > b_p$, such solutions are non-physical. Any solution where density begins at or below the packing density will remain at or below the packing density.

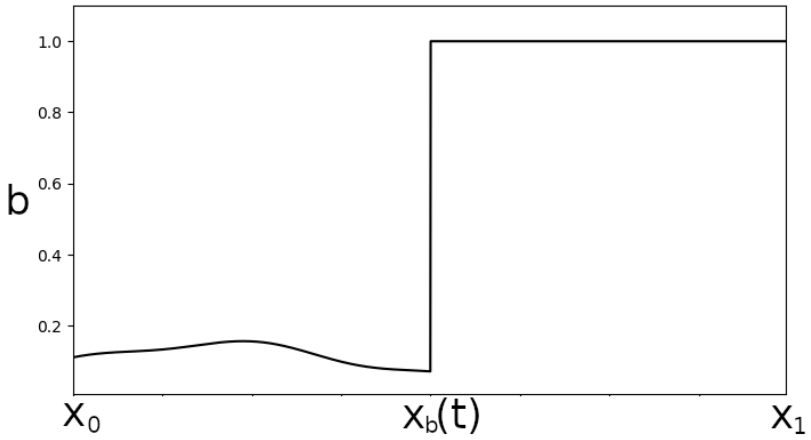

Figure 2.1: A portion of a solution, $b(x,t)$, containing a boundary point, $x_b(t)$, that separates the close-packed region on the right from the rest of the domain.

$x_b(t) < x < x_1$ (see Figure 2.1). By conservation of mass, the following holds:

$$\begin{aligned}\frac{d}{dt}\int_{x_0}^{x_1} b(x,t)\,dx &= \lambda\int_{x_0}^{x_1} b(x,t)\,dx + v(x_0,t)b(x_0,t) - v(x_1,t)b(x_1,t)\\ &= \lambda\int_{x_0}^{x_1} b(x,t)\,dx - v(x_1,t)b_p \end{aligned} \tag{2.6}$$

We have used the fact that the velocity is zero outside the close-packed region, so $v(x_0) = 0$.

We can rewrite the LHS by splitting it into two integrals and applying the Leibniz integral rule to each:

$$\begin{aligned}
\frac{d}{dt}\int_{x_0}^{x_1} b(x,t)\,dx &= \frac{d}{dt}\int_{x_0}^{x_b(t)} b(x,t)\,dx + \frac{d}{dt}\int_{x_b(t)}^{x_1} b(x,t)\,dx \\
&= b(x_b(t)^-,t)\frac{d}{dt}x_b(t) + \int_{x_0}^{x_b(t)} \partial_t b(x,t)\,dx \\
&\quad - b(x_b(t)^+,t)\frac{d}{dt}x_b(t) + \int_{x_b(t)}^{x_1} \partial_t b(x,t)\,dx \\
&= \left(b(x_b(t)^-,t) - b_p\right)\frac{d}{dt}x_b(t) + \int_{x_0}^{x_b(t)} \partial_t b(x,t)\,dx \\
&= \left(b(x_b(t)^-,t) - b_p\right)\frac{d}{dt}x_b(t) + \lambda\int_{x_0}^{x_b(t)} b(x,t)\,dx \qquad (2.7)
\end{aligned}$$

Where $b(x_b(t)^-,t) = \lim_{x\to x_b(t)^-} b(x,t)$, likewise for the right limit, $b(x_b(t)^+,t)$, which in this case is equal to b_p. In the above, we have used the fact that $\partial_t b = 0$ on $[x_b(t), x_1]$ and $\partial_t b = \lambda b$ on $[x_0, x_b(t)]$.

Thus, in the limit $x_1 \to x_b(t)^+$, combining 2.6 and 2.7, we find that

$$\begin{aligned}
\left(b(x_b(t)^-,t) - b_p\right)\frac{d}{dt}x_b(t) + \lambda\int_{x_0}^{x_b(t)} b(x,t)\,dx &= \lambda\int_{x_0}^{x_b(t)} b(x,t)\,dx - v(x_b(t)^+,t)b_p \\
\left(b_p - b(x_b(t)^-,t)\right)\frac{d}{dt}x_b(t) &= v(x_b(t)^+,t)b_p \\
\frac{d}{dt}x_b(t) &= \frac{b_p}{b_p - b(x_b(t)^-,t)}v(x_b(t)^+,t)
\end{aligned}$$

In other words, the velocity of the front separating the close-packed region from the rest of the domain is proportional to the velocity on the interior of the close-packed region, and inversely proportional to the jump in density at the boundary.[9]

This inverse proportionality to the jump in density has a straightforward physical interpretation. When the external density is zero, $\frac{b_p}{b_p - b(x_b(t)^-,t)} = 1$, so we find that the front

[9]Note that a very similar derivation can be done in the two-dimensional case by integrating over a thin rectangle perpendicular to the boundary of the close-packed region. In the limit as the rectangle becomes infinitely thin, the fluxes on the long sides of the rectangle cancel and we recover the same result. We omit the details of the calculation, as they do not meaningfully differ from the 1-dimensional case.

advances with the same velocity as the advective velocity of the close-packed region. When $b(x_b(t)^-, t) \neq 0$, the biomass outside the close-packed region gets added to the advancing front, causing it to expand faster. In the limit when the external density approaches the packing density, the amount of new biomass required to advance the front shrinks to zero, and thus the front velocity diverges.

Example: Suppose we solve the 1-D system 2.5 on the interval $[0, L]$ where $x = 0$ is a wall and $x = L$ is an open boundary. Let $b_p = \lambda = 1$, and take the following as the initial condition:

$$b(x, 0) = \begin{cases} 1 & \text{if } x \in [0, x_b(0)] \\ 0.1 & \text{if } x \in (x_b(0), L] \end{cases}$$

Outside the close-packed region, i.e. when $x \in (x_b(t), L]$, the density is given by $b(x, t) = 0.1e^t$. The velocity inside the close-packed region is $v = \lambda x = x$, and therefore the close-packed region expands with a front velocity determined by $x_b'(t) = \frac{1}{1-0.1e^t} x_b(t)$. This can be solved exactly, yielding the solution:

$$b(x, t) = \begin{cases} 1 & \text{if } x \in [0, x_b(t)] \\ 0.1e^t & \text{if } x \in (x_b(t), L] \end{cases}$$

$$x_b(t) = x_b(0) \frac{9e^t}{10 - e^t}$$

At first glance, it might appear that this solution allows for densities above the packing density. However, $0.1e^t > 1$ only when $t > \ln(10)$, and $x_b(t)$ has a vertical asymptote at $t = \ln(10)$. Thus, the close-packed region will always grow to encompass the entire domain before the density in any other part can exceed the packing density.

2.3 Non-uniform Spread: Coupling Velocity to Cell Orientation

We now turn to the task of coupling the velocity to cell order and orientation. Recall from Section 1.2.1 that we characterize the order of a colony using two quantities: the director, $\vec{d}$, which measures the average local orientation, and the scalar order parameter, S, which measures the degree of alignment between neighbouring cells. These quantities are combined to form the Q-tensor, $\mathbf{Q} = 2S\left(\vec{d} \otimes \vec{d} - \frac{1}{2}\mathbf{I}\right)$.

In Section 2.1, we specified a unique velocity field solving 2.2 by minimizing the total kinetic energy, $K(\vec{v}) = \frac{1}{2} b_p \int_\Omega \vec{v} \cdot \vec{v} \, dA$, which we showed to be equivalent to the pressure formulation by Duddu *et al.*. This choice did not treat any direction of motion preferentially, and the resulting solutions have bacteria spreading uniformly in space.

To incorporate the effects of cell orientation, instead of seeking a $\vec{v}$ to minimize kinetic energy, we will seek a vector field to minimize the following.

$$K_\perp(\vec{v}) = \frac{1}{2} b_p \int_\Omega \vec{v} \cdot \vec{v} + 2\gamma S(\vec{v}_\perp \cdot \vec{v}_\perp) \, dA \tag{2.8}$$

Here, we have adopted the notation $\vec{v}_\parallel = (\vec{v} \cdot \vec{d})\vec{d}$ for the component of the velocity parallel to $\vec{d}$, and $\vec{v}_\perp = \vec{v} - \vec{v}_\parallel$ for the perpendicular component. The parameter γ is a non-negative constant that controls the coupling of the flow to cell orientation.[10]

In other words, we impose a further penalty for motion perpendicular to $\vec{d}$. This penalty is proportional to S. When $S = 0$, the colony is completely disordered, so there should be no effect from cell orientation. When $S = 1$, the colony is maximally ordered, so the effect of orientation should be at its strongest. We will show in Section 2.3.1 and throughout Chapter 4 that the addition of this penalty term will cause microcolonies to spread preferentially in the direction the cells are pointing.

Recall from Proposition 2.1.4 that we could find the velocity field minimizing the kinetic energy by solving a PDE. We will apply the same approach to $K_\perp$, and turn this minimization condition into an equivalent PDE (see Proposition 2.3.3). To this end, we begin by rewriting $K_\perp$, which in 2.8 depends on $\vec{v}_\perp$, in terms of $\mathbf{Q}$. This will make it easier to derive results analogous to those in Section 2.1.

$\mathbf{Q}$ is a matrix, so we can ask how it acts as a linear transformation.

$$\begin{aligned}
\mathbf{Q}\vec{v} &= 2S\left(\vec{d} \otimes \vec{d} - \frac{1}{2}\mathbf{I}\right)\vec{v} \\
&= 2S(\vec{d} \otimes \vec{d})\vec{v} - S\vec{v} \\
&= 2S(\vec{d} \cdot \vec{v})\vec{d} - S\vec{v}
\end{aligned}$$

[10] The factor of 2 is added to simplify the algebra later on.

Taking the dot product of the above with $\vec{v}$, we obtain the following:

$$\begin{aligned}(\mathbf{Q}\vec{v})\cdot\vec{v} &= 2S(\vec{d}\cdot\vec{v})(\vec{d}\cdot\vec{v}) - S\vec{v}\cdot\vec{v} \\ &= 2S(\vec{d}\cdot\vec{v})(\vec{d}\cdot\vec{v})(\vec{d}\cdot\vec{d}) - S\vec{v}\cdot\vec{v} \\ &= 2S\left((\vec{d}\cdot\vec{v})\vec{d}\right)\cdot\left((\vec{d}\cdot\vec{v})\vec{d}\right) - S\vec{v}\cdot\vec{v} \\ &= 2S\vec{v}_{\parallel}\cdot\vec{v}_{\parallel} - S\vec{v}\cdot\vec{v}\end{aligned}$$

Finally, starting with the Pythagorean Theorem (in vector form), we obtain:

$$\begin{aligned}\vec{v}\cdot\vec{v} &= \vec{v}_{\parallel}\cdot\vec{v}_{\parallel} + \vec{v}_{\perp}\cdot\vec{v}_{\perp} \\ 2S\vec{v}\cdot\vec{v} &= 2S\vec{v}_{\parallel}\cdot\vec{v}_{\parallel} + 2S\vec{v}_{\perp}\cdot\vec{v}_{\perp} \\ S\vec{v}\cdot\vec{v} - 2S\vec{v}_{\perp}\cdot\vec{v}_{\perp} &= 2S\vec{v}_{\parallel}\cdot\vec{v}_{\parallel} - S\vec{v}\cdot\vec{v} \\ S\vec{v}\cdot\vec{v} - 2S\vec{v}_{\perp}\cdot\vec{v}_{\perp} &= (\mathbf{Q}\vec{v})\cdot\vec{v} \\ S\vec{v}_{\perp}\cdot\vec{v}_{\perp} &= \frac{1}{2}S\vec{v}\cdot\vec{v} - \frac{1}{2}(\mathbf{Q}\vec{v})\cdot\vec{v}\end{aligned}$$

Using the identity above, we can rewrite $K_{\perp}$ as follows:

$$\begin{aligned}K_{\perp}(\vec{v}) &= \frac{1}{2}b_p\int_{\Omega}\vec{v}\cdot\vec{v} + 2S\gamma\vec{v}_{\perp}\cdot\vec{v}_{\perp}\,dA \\ &= \frac{1}{2}b_p\int_{\Omega}\vec{v}\cdot\vec{v} + \gamma\left(S\vec{v}\cdot\vec{v} - (\mathbf{Q}\vec{v})\cdot\vec{v}\right)\,dA \\ &= \frac{1}{2}b_p\int_{\Omega}(1+\gamma S)\,\vec{v}\cdot\vec{v} - \gamma\,(\mathbf{Q}\vec{v})\cdot\vec{v}\,dA \\ &= \frac{1}{2}b_p\int_{\Omega}\left(\left[(1+\gamma S)\,\mathbf{I} - \gamma\mathbf{Q}\right]\vec{v}\right)\cdot\vec{v}\,dA\end{aligned}$$

For notational convenience, let $\mathbf{M}^{-1} = (1+\gamma S)\,\mathbf{I} - \gamma\mathbf{Q}$.[11] This allows us to write $K_{\perp}(\vec{v}) = \frac{1}{2}b_p\int_{\Omega}(\mathbf{M}^{-1}\vec{v})\cdot\vec{v}\,dA$.

Having rewritten $K_{\perp}$ in this form, we can now follow the same procedure we followed in Section 2.1 to obtain analogous results for $K_{\perp}$. We begin by characterizing the extrema of $K_{\perp}$, much as we did for K in Proposition 2.1.1.

[11] The reason for the inverse will become apparent towards the end of this section.

Let $\vec{u}$ be a divergence free vector field on Ω with $\vec{u} \cdot \hat{n} = 0$ on $\Gamma_{\Omega,w}$. To arrive at the functional derivative of $K_\perp$, we begin by evaluating $K_\epsilon = K_\perp(\vec{v} + \epsilon\vec{u})$.

$$\begin{aligned} K_\epsilon =& \frac{1}{2} b_p \int_\Omega \left(\mathbf{M}^{-1}(\vec{v} + \epsilon\vec{u})\right) \cdot (\vec{v} + \epsilon\vec{u}) \, dA \\ =& \frac{1}{2} b_p \int_\Omega \left(\mathbf{M}^{-1}\vec{v}\right) \cdot \vec{v} + \epsilon \left(\mathbf{M}^{-1}\vec{v}\right) \cdot \vec{u} + \epsilon \left(\mathbf{M}^{-1}\vec{u}\right) \cdot \vec{v} + o(\epsilon^2) \, dA \\ =& K_\perp(\vec{v}) + \epsilon b_p \int_\Omega \left(\mathbf{M}^{-1}\vec{v}\right) \cdot \vec{u} \, dA + o(\epsilon^2) \end{aligned}$$

Note, we have used the fact $(\mathbf{M}^{-1}\vec{u}) \cdot \vec{v} = (\mathbf{M}^{-1}\vec{v}) \cdot \vec{u}$, which follows from the symmetry of $\mathbf{M}^{-1}$.

We then calculate the functional derivative of $K_\perp$.

$$\lim_{\epsilon \to 0} \left(K_\epsilon - K_\perp(\vec{v})\right) / \epsilon = b_p \int_\Omega \left(\mathbf{M}^{-1}\vec{v}\right) \cdot \vec{u} \, dA$$

This provides us with the following characterization:

Proposition 2.3.1. *The vector field $\vec{v}$ is a stationary point of $K_\perp$ iff $\int_\Omega (\mathbf{M}^{-1}\vec{v}) \cdot \vec{u} \, dA = 0$ for all $\vec{u}$ satisfying 2.3.*

We would like a result analogous to proposition 2.1.3, showing that $K_\perp$ is strictly convex.

Proposition 2.3.2. *$K_\perp$ is strictly convex.*

Proof. Following the same proof as 2.1.3, we obtain:

$$tK_\perp(\vec{v}) + (1-t)K_\perp(\vec{u}) - K_\perp(t\vec{v} + (1-t)\vec{u}) = t(1-t)K_\perp(\vec{v} - \vec{u})$$

Notice from the definition of $K_\perp$ (Equation 2.8) that $K_\perp(\vec{v}) \geq K(\vec{v})$. Applying this inequality, we obtain:

$$tK_\perp(\vec{v}) + (1-t)K_\perp(\vec{u}) - K_\perp(t\vec{v} + (1-t)\vec{u}) \geq t(1-t)K(\vec{v} - \vec{u})$$

The result then follows using the same argument as proposition 2.1.3. □

Combining the results from Propositions 2.3.2, 2.1.2, and 2.3.1, we have shown that $K_\perp$ has a unique minimum, and that this minimum is the unique solution to 2.3 that satisfies $\int_\Omega (\mathbf{M}^{-1}\vec{v}) \cdot \vec{u} \, dA = 0$ for all $\vec{u}$ satisfying 2.3. We can now prove the analogue of proposition 2.1.4.

Proposition 2.3.3. *Suppose there exists a function p that solves the following Poisson problem:*

$$\begin{aligned} \nabla \cdot (\mathbf{M}\nabla p) &= -\lambda \quad && \text{on } \Omega \\ p &= 0 && \text{on } \Gamma_{\Omega,f} \\ (\mathbf{M}\nabla p) \cdot \hat{n} &= 0 && \text{on } \Gamma_{\Omega,w} \end{aligned} \tag{2.9}$$

Then the velocity field $\vec{v} = -\mathbf{M}\nabla p$ satisfies 2.2. Moreover, this $\vec{v}$ is the velocity that minimizes $K_\perp$ over all solutions of 2.2.

Proof. It is clear that $\vec{v}$ satisfies 2.2. Recall that $\vec{v}$ is a minimum of $K_\perp$ if $\int_\Omega (\mathbf{M}^{-1}\vec{v})\cdot\vec{u}\, dA = 0$ for every vector field $\vec{u}$ satisfying 2.3. A direct computation yields:

$$\begin{aligned} \int_\Omega \left(\mathbf{M}^{-1}\vec{v}\right) \cdot \vec{u}\, d &= -\int_\Omega \nabla p \cdot \vec{u}\, dA \\ &= -\int_\Omega \left(\nabla \cdot (p\vec{u}) - p\nabla \cdot \vec{u}\right)\, dA \\ &= -\int_{\partial\Omega} p\vec{u} \cdot \hat{n}\, ds + \int_\Omega p\nabla \cdot \vec{u}\, dA \qquad \text{by the divergence theorem} \\ &= -\int_{\Gamma_{\Omega,w}} p\vec{u} \cdot \hat{n}\, ds - \int_{\Gamma_{\Omega,f}} p\vec{u} \cdot \hat{n}\, ds + \int_\Omega p\nabla \cdot \vec{u}\, dA \\ &= 0 \end{aligned}$$

The first integral vanishes because $\vec{u}\cdot\hat{n} = 0$ on walls, the second because $p = 0$ on free/open boundaries, and the third because $\vec{u}$ is divergence-free. □

The only remaining concern is the existence of solutions to 2.9 (and, by extension, 2.4). We begin by computing $\mathbf{M}$ explicitly.

$$\begin{aligned} \mathbf{M} &= \left((1+S\gamma)\,\mathbf{I} - \gamma\mathbf{Q}\right)^{-1} \\ &= \begin{bmatrix} 1+S\gamma-\gamma Q_{11} & -\gamma Q_{12} \\ -\gamma Q_{21} & 1+S\gamma-\gamma Q_{22} \end{bmatrix}^{-1} \\ &= \frac{1}{\det\left(\mathbf{M}^{-1}\right)} \begin{bmatrix} 1+S\gamma-\gamma Q_{22} & \gamma Q_{12} \\ \gamma Q_{21} & 1+S\gamma-\gamma Q_{11} \end{bmatrix} \\ &= \frac{1}{\det\left(\mathbf{M}^{-1}\right)} \left((1+S\gamma)\,\mathbf{I} + \gamma\mathbf{Q}\right) \end{aligned}$$

where

$$\begin{aligned}
\det\left(\mathbf{M}^{-1}\right) &= (1+S\gamma-\gamma Q_{11})(1+S\gamma-\gamma Q_{22})-\gamma^2 Q_{12}Q_{21} \\
&= (1+S\gamma-\gamma Q_{11})(1+S\gamma+\gamma Q_{11})-\gamma^2 Q_{12}^2 \\
&= (1+S\gamma)^2-\gamma^2 Q_{11}^2-\gamma^2 Q_{12}^2 \\
&= (1+S\gamma)^2-\gamma^2\left(Q_{11}^2+Q_{12}^2\right) \\
&= (1+S\gamma)^2-\gamma^2 S^2 \\
&= 1+2S\gamma
\end{aligned}$$

Note in particular that because $S \in [0,1]$ and γ is non-negative, it follows that $\mathbf{M}$ is always well-defined.

Next, notice that $\mathbf{M}$ is symmetric and satisfies the *uniform ellipticity condition* [67], i.e.:

Lemma 2.3.4. *There exists a constant $c>0$ s.t. for all $\xi \in \mathbb{R}^2$, $M_{ij}\xi_i\xi_j \geq c(\xi_1^2+\xi_2^2)$.*

Proof.

$$\begin{aligned}
M_{ij}\xi_i\xi_j &= \left(\frac{1+S\gamma}{1+2S\gamma}+\frac{S\gamma}{1+2S\gamma}\cos(2\theta)\right)\xi_1^2+\frac{2S\gamma}{1+2S\gamma}\sin(2\theta)\xi_1\xi_2 \\
&\quad+\left(\frac{1+S\gamma}{1+2S\gamma}-\frac{S\gamma}{1+2S\gamma}\cos(2\theta)\right)\xi_2^2 \\
&= \frac{1+S\gamma}{1+2S\gamma}(\xi_1^2+\xi_2^2)+\frac{S\gamma}{1+2S\gamma}\left((\xi_1^2-\xi_2^2)\cos(2\theta)+2\xi_1\xi_2\sin(2\theta)\right) \\
&= \frac{1+S\gamma}{1+2S\gamma}(\xi_1^2+\xi_2^2)+\frac{S\gamma}{1+2S\gamma}(\xi_1^2+\xi_2^2)\cos(2\theta+\omega) \\
&\geq \frac{1+S\gamma}{1+2S\gamma}(\xi_1^2+\xi_2^2)+\frac{S\gamma}{1+2S\gamma}(\xi_1^2+\xi_2^2)(-1) \\
&= \frac{1}{1+2S\gamma}(\xi_1^2+\xi_2^2) \\
&\geq \frac{1}{1+2\gamma}(\xi_1^2+\xi_2^2)
\end{aligned}$$

The first equality follows from the definition of $\mathbf{M}$, using the fact that $\mathbf{Q} = S\begin{bmatrix}\cos(2\theta) & \sin(2\theta)\\ \sin(2\theta) & -\cos(2\theta)\end{bmatrix}$ where θ is the angle of the director, $\vec{q}$. □

Thus, we can apply Theorem 2.7 from [67]. The following is a restatement of the Theorem, simplified to match our specific problem.

Theorem 2.3.5. *Consider the following boundary value problem:*

$$\begin{aligned} -\nabla \cdot (\mathbf{M}\nabla p) &= f \quad \text{on } \Omega \\ \hat{n} \cdot (\mathbf{M}\nabla p) &= g \quad \text{on } \Gamma_1 \\ p &= 0 \quad \text{on } \Gamma_0 \end{aligned}$$

where $\Omega \subset \mathbb{R}^n$ is a bounded Lipschitz domain with boundary $\partial\Omega = \Gamma_1 \cup \Gamma_0$, s.t. $|\Gamma_0| > 0$, and where $\mathbf{M}$ is symmetric and defines a uniformly elliptic operator. Then for all $f \in L^2(\Omega)$ and $g \in L^2(\Gamma_1)$, the boundary value problem has a unique weak solution $p \in \{y \in H^1(\Omega) \mid y_{|\Gamma_0} = 0\}$. Moreover, the following inequality holds:

$$||p||_{H^1(\Omega)} \leq c_M \left(||f||_{L^2(\Omega)} + ||g||_{L^2(\Gamma_1)} \right)$$

where $c_M > 0$ is a constant which does not depend on f or g.[12]

In our case, $f = \lambda$ and $g = 0$, so every condition is satisfied except for the requirement that Ω be a Lipschitz domain. This is not a very strong constraint, but proving that the close-packed region remains a Lipschitz domain is beyond the scope of this thesis.

Combining Proposition 2.3.3 with equations 1.13 and 1.15, we obtain the following system of equations:

$$\begin{aligned} \partial_t b + \nabla \cdot (b\vec{v}) &= \lambda b \\ \vec{v} &= \begin{cases} -\mathbf{M}\nabla p & \text{on } \Omega \\ 0 & \text{on } D \setminus \Omega \end{cases} \\ \nabla \cdot (\mathbf{M}\nabla p) &= -\lambda && \text{on } \Omega \\ p &= 0 && \text{on } \Gamma_{\Omega,f} \\ \mathbf{M}\nabla p \cdot \hat{n} &= 0 && \text{on } \Gamma_{\Omega,w} \end{aligned} \tag{2.10}$$

$$\mathbf{M} = \frac{1 + S\gamma}{1 + 2S\gamma}\mathbf{I} + \frac{\gamma}{1 + 2S\gamma}\mathbf{Q}$$

Where $\mathbf{Q}$ evolves according to the Beris-Edwards equation:

$$(\partial_t + \vec{v} \cdot \nabla)Q_{\alpha\beta} = 2\xi u_{\alpha\beta} + \omega_{\alpha\eta}Q_{\eta\beta} - Q_{\alpha\eta}\omega_{\eta\beta} - \xi \text{tr}(\mathbf{uQ})Q_{\alpha\beta} + H_{\alpha\beta}$$

[12] We will not use this latter inequality, except to note here that it constrains the magnitude of $\vec{v}$.

W.l.o.g. we will rescale b and t such that $b_p = \lambda = 1$.

This model is our main contribution to the literature. In particular, note that the matrix $\mathbf{M}$ (which is a function of $\mathbf{Q}$) appears *outside* the gradient in $\vec{v} = -\mathbf{M}\nabla p$. This will allow cell orientation to have an impact on the microcolony dynamics even in the absence of gradients in the Q-tensor.

The rest of this thesis will be devoted to studying this model.

2.3.1 Effect of γ on $\vec{v}$

Notice that the governing equations for $\vec{v}$ in 2.10 do not depend explicitly on time. If we choose values for $\mathbf{Q}$ and Ω at some time t, we can solve the equations for $\vec{v}$ at that time point. In this section, we perform one such calculation to demonstrate how the perpendicular penalty impacts the velocity.

Consider an elliptical microcolony, $\Omega = \left\{(x,y) \in \mathbb{R}^2 \middle| \frac{x^2}{a_1^2} + \frac{y^2}{a_2^2} \leq 1\right\}$, where the cells are aligned horizontally and where S is constant throughout the domain, i.e. $\mathbf{Q} = S\begin{bmatrix} 1 & 0 \\ 0 & -1 \end{bmatrix}$. We wish to solve the following Poisson problem:

$$\begin{aligned} \nabla \cdot \mathbf{M}\nabla p &= -\lambda \qquad \text{on } \Omega \\ p &= 0 \qquad \text{on } \partial\Omega \end{aligned}$$

Note that in this case $\mathbf{M}$ simplifies as follows,

$$\begin{aligned} \mathbf{M} &= \frac{1+S\gamma}{1+2S\gamma}\mathbf{I} + \frac{\gamma}{1+2S\gamma}\mathbf{Q} \\ &= \frac{1+S\gamma}{1+2S\gamma}\mathbf{I} + \frac{S\gamma}{1+2S\gamma}\begin{bmatrix} 1 & 0 \\ 0 & -1 \end{bmatrix} \\ &= \begin{bmatrix} 1 & 0 \\ 0 & \frac{1}{1+2S\gamma} \end{bmatrix} \end{aligned}$$

The Poisson equation reduces to $\partial_x^2 p + \frac{1}{1+2S\gamma}\partial_y^2 p = -\lambda$, which admits the unique solution:

$$p = -\frac{\lambda}{2}\frac{a_1^2 a_2^2(1+2S\gamma)}{a_1^2 + a_2^2(1+2S\gamma)}\left(\frac{x^2}{a_1^2} + \frac{y^2}{a_2^2} - 1\right)$$

The corresponding velocity field is:

$$\vec{v} = -\mathbf{M}\nabla p = \frac{\lambda}{a_1^2 + a_2^2(1+2S\gamma)} \begin{bmatrix} a_2^2(1+2S\gamma)x \\ a_1^2 y \end{bmatrix} \tag{2.11}$$

When $\gamma = 0$ and $a_1 = a_2$, the solution corresponds to uniform radial spread. As $\gamma \to \infty$, the solution converges to $\begin{bmatrix} \lambda x \\ 0 \end{bmatrix}$, i.e. the velocity field aligns with the cells. In other words, increasing γ causes new biomass to spread preferentially in the direction of the director.

We will extend this to a full analytic solution to 2.10 in Chapter 4.

2.4 Near-incompressible Formulation

We noted at the end of Section 2.1 that the uniform spread model, 2.5, could be interpreted as the non-inertial limit of a system governed by a Cauchy momentum equation. The same is true of the model of non-uniform spread, 2.10.

Suppose we start from a momentum equation of the form:

$$\frac{D(b\vec{v})}{Dt} = -\nabla p - \mu b \mathbf{M}^{-1}\vec{v}$$

As we did in Section 2.1, we drop the inertial term to obtain an equation balancing friction against pressure: $\mu b \mathbf{M}^{-1}\vec{v} = -\nabla p$. Rescaling pressure, $\frac{p}{\mu b_p} \to p$, yields $\mathbf{M}^{-1}\vec{v} = -\frac{b_p}{b}\nabla p$. The incompressibility constraint then recovers the equation $\nabla \cdot \frac{b_p}{b}\mathbf{M}\nabla p = -\lambda$, which when $b = b_p$ is identical to the pressure equation in 2.10.

This suggests an alternative formulation of 2.10. Instead of applying the incompressibility constraint, we could follow [69], [21], and [72], and posit an explicit form for p, e.g. $p = \max\left(A\left(b - b_p\right), 0\right)$. For sufficiently large values of A, this approximates incompressibility: pressure is zero unless the density exceeds the packing density, in which case it rises rapidly.

This leads to an inertial formulation that converges to 2.10 in the non-inertial, incompressible limit:

$$\begin{aligned} \partial_t b + \nabla \cdot (b\vec{v}) &= \lambda b \\ (\partial_t + \vec{v}\cdot\nabla)(b\vec{v}) &= -\nabla p - \mu b \mathbf{M}^{-1}\vec{v} \\ (\partial_t + \vec{v}\cdot\nabla)Q_{\alpha\beta} &= 2\xi u_{\alpha\beta} + \omega_{\alpha\gamma}Q_{\gamma\beta} - Q_{\alpha\gamma}\omega_{\gamma\beta} - \xi \mathrm{tr}(\mathbf{uQ})Q_{\alpha\beta} + \Gamma H_{\alpha\beta} \end{aligned} \tag{2.12}$$

where $p = \max\left(A\left(b - b_p\right), 0\right)$ or, slightly more generally, $p = \begin{cases} A\left(b - b_p\right)^k & \text{if } b \geq b_p \\ 0 & \text{if } b < b_p \end{cases}$.

Note, however, that 2.10 can also be recovered in the non-inertial, incompressible limit if we adopt the following momentum equation:

$$(\partial_t + \vec{v} \cdot \nabla)(b\vec{v}) = -\mathbf{M}\nabla p - \mu b\vec{v} \tag{2.13}$$

Equations 2.12 and 2.13 have different physical interpretations. The term $\mu b\mathbf{M}^{-1}\vec{v}$ in Equation 2.12 can be interpreted as an anisotropic friction term that depends on cell orientation. A term of the form $\mathbf{M}\nabla p$ on the other hand, suggests that the system has a preferred direction along which to resolve pressure/density gradients. This seems to us to better match our intuitive understanding of the system, namely that it is driven by asymmetric forces of expansion produced by growth. Fortunately, both 2.12 and 2.13 behave similarly for appropriate parameter values (see Chapter 4).

In any case, 2.12 and 2.13 can be made equivalent by dropping the inertial term, leading to the following non-inertial, near-incompressible formulation (note that μ has been absorbed into the A in the definition of p).

$$\begin{aligned} \partial_t b + \nabla \cdot (b\vec{v}) &= \lambda b \\ b\vec{v} &= -\mathbf{M}\nabla p \\ (\partial_t + \vec{v} \cdot \nabla)Q_{\alpha\beta} &= 2\xi u_{\alpha\beta} + \omega_{\alpha\gamma}Q_{\gamma\beta} - Q_{\alpha\gamma}\omega_{\gamma\beta} - \xi \mathrm{tr}(\mathbf{uQ})Q_{\alpha\beta} + \Gamma H_{\alpha\beta} \end{aligned} \tag{2.14}$$

These formulations have certain advantages. For one, they are similar in form to the models of [69], [21], and [72], making a direct comparison easier. Moreover, they admit much simpler numerical implementations, as we will see in Section 3.3. On the other hand, positing an explicit form for pressure seems to us to be a much stronger assumption than incompressibility. And, as we will see in Chapter 4, these near-incompressible models exhibit behaviours that deviate from those of 2.10 in unexpected ways.

Chapter 3

Model Implementation

We outline numerical implementations for three models described thus far: the 1-dimensional model discussed in section 2.2, the incompressible model in two dimensions (Equations 2.10). We will also outline a simple implementation of the near-incompressible approximation (Equations 2.12-2.13) to compare with the behaviour of the incompressible model.

3.1 Numerical Implementation of the 1D Model

Recall the 1-dimensional system from Section 2.2:

$$\begin{aligned} \partial_t b + \partial_x(bv) &= \lambda b \\ v &= \begin{cases} -\partial_x p & \text{on } \Omega \\ 0 & \text{on } D \setminus \Omega \end{cases} \\ \partial_x^2 p &= -\lambda && \text{on } \Omega \\ p &= 0 && \text{on } \Gamma_{\Omega,f} \\ \partial_x p &= 0 && \text{on } \Gamma_{\Omega,w} \end{aligned} \tag{3.1}$$

$D \subset \mathbb{R}$ is the system's domain, $\Omega \subset D$ is the subset of the domain where $b \geq b_p$, $\Gamma_{\Omega,w} \subset \partial\Omega$ is the subset of Ω's boundary which coincides with any walls bounding D, and $\Gamma_{\Omega,f} = \partial\Omega \setminus \Gamma_{\Omega,w}$ is the free portion of Ω's boundary. In what follows, we will assume D is a finite domain, which, w.l.o.g., we can take to be $D = [0, 1]$.

We will simulate the model using a finite difference scheme. Let $h > 0$ be a scale parameter characterizing the coarseness of the spatial discretization. Let $x_0 = 0$ be the leftmost point of the domain, then $x_i = x_0 + ih$. We choose $h = 1/N$ for some positive integer N, such that $x_N = 1$ coincides with the rightmost point of the domain. We approximate the functions b, v, and p using vectors b_h, v_h, and p_h, where each component of these vectors approximates the corresponding function's value at a specific point in space. E.g. $b_h = [b^0, b^1, ..., b^N]$, $b^i \approx b(x_i)$.

We discretize the time derivatives with the forward Euler method, where the timestep is determined by a CFL condition[1] with $\Delta t_{max} = 0.01$:

$$\Delta t = \min\left(\Delta t_{max}, \frac{h}{4||v_h||_\infty}\right).$$

We discretize the spatial derivatives of p using a central difference scheme that we complement with a staggered grid representation. The vectors $b_h = [b^0, b^1, ..., b^N]$ and $p_h = [p^0, p^1, ..., p^N]$ approximate the values of b and p at integer multiples of h, whereas the vector $v_h = [v^{1/2}, v^{1+1/2}, ..., v^{N-1/2}]$ is staggered by a half step.

Concretely, we approximate $v = -\partial_x p$ using $v^{i+1/2} = -\frac{p^{i+1} - p^i}{h}$. We approximate $\partial_x(bv)$ using the following discretization:

$$\partial_x(bv)(x_i) \approx \frac{b_u^{i+1/2} v^{i+1/2} - b_u^{i-1/2} v^{i-1/2}}{h}$$

In the above, b_u is the upwind density, $b_u^{i+1/2} \equiv \begin{cases} b^i & \text{if } v^{i+1/2} \geq 0 \\ b^{i+1} & \text{if } v^{i+1/2} < 0 \end{cases}$.

It only remains to discretize the equation for pressure, $\partial_x^2 p = -\lambda$. As discussed in section 2.2, this equation can be solved analytically, provided we know Ω. Unfortunately, using this pressure with the discretization discussed above does not result in a satisfactory numerical model, because nothing in the implementation prevents b_h from exceeding the packing density, b_p. In the exact model, the divergence constraint on the velocity, $\partial_x v = \lambda$, ensures that this never occurs. In the numerical implementation, however, inaccuracies in the computation, particularly at the boundary of Ω, where $\partial_x v$ is discontinuous, cause b_h to exceed the packing density. Once this occurs, there is no mechanism to correct this error.

[1] The CFL condition was first introduced by Courant Friedrichs and Lewy in [17], translated in [18]. See [19] for a modern discussion of the topic.

There are many ways to tackle this issue. We will see alternatives in later sections, but for the 1D case it is sufficient to relax the incompressibility condition and introduce an elastic restoring force.

We replace the original pressure equation, $\partial_x^2 p = -\lambda$ with the equation $\partial_x^2 p = k\left(1 - \frac{b}{b_p}\right)$ where k is a positive constant. It may not be initially clear that these two equations should lead to qualitatively similar results, but this is indeed the case. If we rewrite the evolution equation for density in its material derivative form, we obtain:

$$\begin{aligned}
\partial_t b + \partial_x(bv) &= \lambda b \\
\partial_t b + v\partial_x b &= -b\partial_x v + \lambda b \\
&= b\partial_x^2 p + \lambda b \\
&= kb\left(1 - \frac{b}{b_p}\right) + \lambda b \\
&= kb\left(1 + \frac{\lambda}{k} - \frac{b}{b_p}\right)
\end{aligned}$$

The RHS is a logistic growth term which converges to the steady state $b = b_p\left(1 + \frac{\lambda}{k}\right)$. When b is in steady state, we recover the incompressible pressure equation.

$$\begin{aligned}
\partial_x^2 p &= k\left(1 - \frac{b_p\left(1 + \frac{\lambda}{k}\right)}{b_p}\right) \\
&= k\left(1 - 1 - \frac{\lambda}{k}\right) \\
&= -\lambda
\end{aligned}$$

In the limit as $k \to \infty$, we recover the steady state $b = b_p$ in the close-packed region, and the convergence to this steady state via the logistic term becomes instantaneous. I.e. we recover the incompressible system.

With this modification to the pressure equation in place, we can describe our numerical scheme.

$t = T_{initial}$
while $t < T_{final}$ **do**
Extract Ω using the threshold $b_h > b_p$
Solve[a] the boundary value problem:

$$\begin{aligned} \partial_x^2 p &= k\left(1 - \frac{b}{b_p}\right) && \text{on } \Omega \\ p &= 0 && \text{on } \Gamma_{\Omega,f} \\ \partial_x p &= 0 && \text{on } \Gamma_{\Omega,w} \end{aligned}$$

for $x_{i+1/2}$ in D **do**
if $x_{i+1/2} \in \Omega$ **then**
$v^{i+1/2} = -\frac{p^{i+1} - p^i}{h}$
else
$v^{i+1/2} = 0$
end if
end for
$\Delta t = \min\left(\Delta t_{max}, \frac{h}{4||v_h||_\infty}\right)$
for i in $\{0, 1, ..., N\}$ **do**
$b^i \mathrel{+}= \Delta t\left(\lambda b^i - \frac{b_u^{i+1/2} v^{i+1/2} - b_u^{i-1/2} v^{i-1/2}}{h}\right)$
end for
$t \mathrel{+}= \Delta t$
end while

[a] We solve this using the boundary value problem solver `solve_bvp` from the Python library `scipy.integrate`.

The results of this scheme are analyzed in Chapter 4, where we will show that the scheme reproduces the desired behaviour, converging to the true solution at a rate linear in h.

3.2 Numerical Implementation of the 2D Model

Recall equations 2.10:

$$\begin{aligned}
\partial_t b + \nabla \cdot (b\vec{v}) &= \lambda b \\
(\partial_t + \vec{v} \cdot \nabla)\mathbf{Q} &= 2\xi \mathbf{u} + \boldsymbol{\omega}\mathbf{Q} - \mathbf{Q}\boldsymbol{\omega} - \xi \mathrm{tr}(\mathbf{u}\mathbf{Q})\mathbf{Q} + \Gamma \mathbf{H} \\
\vec{v} &= \begin{cases} -\mathbf{M}\nabla p & \text{on } \Omega \\ 0 & \text{on } D \setminus \Omega \end{cases} \\
\nabla \cdot (\mathbf{M}\nabla p) &= -\lambda \quad \text{on } \Omega \\
p &= 0 \quad \text{on } \Gamma_{\Omega,f} \\
\mathbf{M}\nabla p \cdot \hat{n} &= 0 \quad \text{on } \Gamma_{\Omega,w}
\end{aligned}$$

$$\mathbf{M} = \frac{1 + S\gamma}{1 + 2S\gamma}\mathbf{I} + \frac{\gamma}{1 + 2S\gamma}\mathbf{Q}$$

In two spatial dimensions, the close-packed region, Ω, can have irregular boundaries. This makes the pressure equation, $\nabla \cdot (\mathbf{M}\nabla p) = -\lambda$, difficult to solve using a finite-difference scheme. This motivates us to use finite element methods. However, we will not seek to recast the whole problem into a finite element framework. Instead, we will use a hybrid scheme, combining finite difference methods and finite element methods, similar to [27]. This is primarily because the Beris-Edwards equation is highly non-linear, and does not easily lend itself to a finite element formulation. We discuss a possible implementation in Section 5.3.

In a typical solution to 2.10, the bacterial density, b, will have a jump discontinuity at the boundary of Ω. Inside the close-packed region, it is equal to the packing density, b_p. Outside the close-packed region, it grows exponentially. The interface separating these regions moves proportionally to the velocity, $\vec{v}$, and inversely proportionally to the jump in density across the interface boundary.

In the 1-dimensional system, we were able to replicate this behaviour using a single function to describe density and directly solving the evolution equation for density (1.13). For the 2-dimensional system, we will adopt a different approach.

Instead of using a single vector, b^h, to represent density, will directly incorporate the piecewise nature of the solutions into our numerical scheme. We define two functions, b_{out} and ϕ. The first, b_{out}, represents the density outside of the closed-packed region,

$b_{out}(x, y, t) = b_{out}(x, y, 0)e^{\lambda t}$.[2] The second function, ϕ, describes the boundary, $\Gamma \equiv \partial\Omega$, via its zero-level set, i.e. $\{(x, y) \in D | \phi(x, y) = 0\} = \Gamma$. It will evolve according to $\partial_t \phi + \vec{v}_{ext} \cdot \nabla\phi = 0$, for some velocity, $\vec{v}_{ext}$, to be specified later. Representing a boundary in this way, by means of a level set, is the central tool at the core of a class of numerical schemes called *level set methods* which we will briefly review in the next section.

3.2.1 Level Set Methods

Level set methods [55] are a class of numerical methods that use the level sets of scalar functions to describe curves, surfaces, and their higher-dimensional analogues. They find applications in numerous fields, including image processing [56], optimization [68], and computational fluid dynamics [64]. One advantage of level set methods over direct parametrization is the ease with which they can represent changes in a curve's topology. This is particularly relevant to our problem, because microcolonies can and do merge together as they grow.

When constructing the level set function, ϕ, we are only constrained by the location of the zero-level set, so there is a lot of freedom in the choice of function. Any sufficiently well-behaved function will do, but it is common to require that ϕ be a *signed distance function*, that is, a function whose value is the shortest distance to the zero-level set and whose sign indicates whether a point is inside (positive) or outside (negative) the close-packed region. From this definition, it follows that signed distance functions satisfy the eikonal equation:

$$|\nabla\phi| = 1 \tag{3.2}$$

Maintaining the signed-distance property ensures that ϕ will never be overly shallow or overly steep. For an overly shallow function, the location of the level set will be susceptible to small changes in magnitude (e.g. from rounding errors and other inaccuracies in the numerics), while an overly steep function results in large gradients. Maintaining the signed-distance property also ensures that no spurious zero-level sets are created, provided that our velocity is also sufficiently well behaved.

Recall that ϕ evolves according to a continuity equation, which in general will not guarantee that ϕ maintains the signed-distance property. There are two ways to ensure that ϕ remains a signed distance function: reinitialization and velocity extension. Our implementation will make use of both.

Reinitialization entails periodically pausing the main loop of our numerical scheme to recalculate ϕ, updating its values while preserving the same zero levelset. We perform

[2] In practice, we will only consider the special case where $b_{out}(x, y, 0) = 0$, which allows us to ignore the dynamics of b_{out}.

reinitialization by solving the eikonal equation 3.2, coupled with the condition $\phi_{new}(x) = \phi_{old}(x)$ for $x \in \Gamma$. This boundary, Γ, is on the interior of the domain, so special techniques are required to solve the problem. There are several such techniques available, including methods for FEM schemes, e.g. [6]. We will use the *fast marching method*, first proposed by James Sethian in [63].

There is a balance to be struck here. If we reinitialize too infrequently, ϕ may become distorted enough to introduce spurious level sets. However, we also do not wish to reinitialize too often (e.g. after every time step) because (a) it would be computationally expensive and (b) each reinitialization introduces small errors in the location of the zero-level set, which can compound if done too frequently.

Velocity extension entails choosing a velocity field, $\vec{v}_{ext}$, such that, when we evolve ϕ using the continuity equation $\partial_t \phi + \vec{v}_{ext} \cdot \nabla \phi = 0$, the signed-distance property is preserved. In order for the zero-level set to evolve correctly, $\vec{v}_{ext}$ must have the same value on Γ as the velocity defined by our original system of PDEs, 2.9.[3] Finding this velocity field will require us to solve a PDE, which we derive as follows.

We seek a velocity that leaves $|\nabla \phi|$ unchanged. I.e. a velocity such that $\partial_t |\nabla \phi| = 0$, or, equivalently, $\partial_t |\nabla \phi|^2 = 0$. Expanding, we obtain:

$$\begin{aligned} 0 &= \partial_t |\nabla \phi|^2 \\ &= \partial_t (\nabla \phi \cdot \nabla \phi) \\ &= 2 \nabla \phi \cdot \nabla \partial_t \phi \\ &= -2 \nabla \phi \cdot \nabla (\vec{v}_{ext} \cdot \nabla \phi) \end{aligned}$$

We only care about the evolution of the levelsets of ϕ, so we may neglect any velocity tangent to the level set. This allows us to write $\vec{v}_{ext} = F \nabla \phi$ for some scalar field, F. This simplifies the condition above significantly.

$$\begin{aligned} 0 &= -2 \nabla \phi \cdot \nabla (F \nabla \phi \cdot \nabla \phi) \\ &= -2 \nabla \phi \cdot \nabla (F |\nabla \phi|^2) \\ &= -2 \nabla \phi \cdot \nabla F \end{aligned}$$

Thus, if we select a velocity $\vec{v}_{ext} = F \nabla \phi$ such that $\nabla \phi \cdot \nabla F = 0$, and such that $\vec{v}_{ext}$ has the correct value on Γ, this will ensure that the evolution of ϕ preserves the signed-distance property while correctly advancing the zero-level set. We will solve the equation $\nabla \phi \cdot \nabla F = 0$ using a variation of the fast marching method.[1]

[3] This process of velocity extension has another benefit: it provides a natural way to define the velocity field outside the close-packed region.

3.2.2 The Fast Marching Method

The fast marching method is a finite difference method used to solve problems of the form $|\nabla\phi| = \frac{1}{f(x)}$ with $\phi(x) = 0$ on some boundary $x \in \Gamma$.[4] The method can be seen as a multi-dimensional extension of the finite difference schemes that are used to solve 1-dimensional initial value problems, such as Euler's method. The key difference is that instead of advancing the solution in one dimension—forward in time from a single initial point—it advances the solution in two (or more) dimensions, radially outward from a set of initial points.

We will begin by describing the algorithm for velocity extension. We wish to solve the following PDE:

$$\begin{aligned} \nabla\phi \cdot \nabla F &= 0 \quad \text{on } D \\ F &= F_0 \quad \text{on } \Gamma \end{aligned} \tag{3.3}$$

Where $F_0 = \frac{b_p}{b_p - b_{out}} \left(\vec{v} \cdot \frac{\nabla\varphi}{||\nabla\varphi||} \right)$ is the component of $\vec{v}$ perpendicular to the level sets of φ, rescaled to account for jump in density at the boundary, as in Section 2.2. It is this boundary condition that causes the zero-level set of φ to coincide with the boundary of the close-packed region.

1-dimensional systems have an important property that makes them easier to solve than multi-dimensional systems: the underlying space is a totally ordered set. When solving an ODE using a typical finite difference scheme, each step consists of choosing the smallest time point for which no value has been computed, and then computing its value using the values at previous time points. The local geometry at each step looks the same. We know the values at times $t_i, t_{i-1}, t_{i-2}, ...$ and we don't know the values at times $t_{i+1}, t_{i+2}, t_{i+3}, ...$ This allows us to use the same finite difference operator at every iteration.

If we attempt to extend this process to two dimensions, we will need to address the following questions at each step:

- Which value should we calculate next?
- Having chosen the next value to calculate, which finite difference operator should we use to approximate our PDE?

Signed distance functions provide an elegant way to answer the first question: starting from a set of initial points (i.e. the zero-level set of our signed distance function), we order

[4] We are only interested in the case $f(x) = 1$.

all the points in our spatial discretization based on their distance to the initial points. This gives us an easy way to choose the next value to calculate. Unfortunately, the local geometry will not necessarily be the same for every point, so we cannot approximate ∇F using a fixed finite difference operator. Fortunately, the signed distance function provides a way to choose a difference operator on-the-fly.

The algorithm to solve 3.3 is as follows:

Initialization: For points (x_i, y_j) "on" Γ, let $F(x_i, y_j) = F_0$ and add the points (x_i, y_j) to the set **Solved**. All other points in the domain are added to the set **Unsolved**.

while Unsolved $\neq \emptyset$ **do**

Find the point $(x_i, y_j) \in$ **Unsolved** closest to Γ, i.e. that minimizes $|\phi(x_i, y_j)|$.

Find the smallest **Solved** neighbour to (x_i, y_j) in the x direction (as measured by ϕ) and use it to approximate $\partial_x F(x_i, y_j)$ and $\partial_x \phi(x_i, y_j)$. If (x_i, y_j) has no solved neighbours in the x direction, let $\partial_x F(x_i, y_j) = 0$. Written explicitly:

$$\left.\frac{\partial F}{\partial x}\right|_{(x_i,y_j)} \approx \begin{cases} 0 & \phi(x_{i+1}, y_j) = \phi(x_{i-1}, y_j) = \infty \\ \frac{F(x_{i+1},y_j) - F(x_i,y_j)}{\Delta x} & \phi(x_{i+1,j}) \leq \phi(x_{i-1,j}) \\ \frac{F(x_i,y_j) - F(x_{i-1},y_j)}{\Delta x} & \phi(x_{i+1,j}) > \phi(x_{i-1,j}) \end{cases}$$

Where by convention $\phi(x, y) = \infty$ if $(x, y) \in$ **Unsolved**.

Find the smallest **Solved** neighbour to (x_i, y_j) in the y direction (as measured by ϕ) and use it to approximate $\partial_y F(x_i, y_j)$ and $\partial_y \phi(x_i, y_j)$. If (x_i, y_j) has no solved neighbours in the y direction, let $\partial_y F(x_i, y_j) = 0$.

Calculate $F(x_i, y_j)$ by discretizing $\nabla\phi \cdot \nabla F = 0$ using the difference operators defined above and isolating $F(x_i, y_j)$.

Remove (x_i, y_j) from **Unsolved** and add it to **Solved**

end while

We can improve the accuracy of this method in a number of ways, for instance by choosing higher order finite difference operators, or by choosing more accurate initialization methods, as in [16].

The method outlined above requires that we already have a signed distance function available to assist the calculation. This is sufficient for velocity extension, but not for reinitialization, where constructing the signed distance function is the goal. As we next show, the fast marching method does not make this assumption. Instead, it builds a partial and approximate signed distance function, and uses it to construct the "true" signed distance function. It does this by introducing a third set of points, **TentativelySolved**, in addition to **Solved** and **Unsolved**, as follows.

Every unsolved point which neighbours a solved point is assigned a tentative ϕ value. This creates a border between the solved region and the unsolved region. We can take advantage of this new class of points to revisit the algorithm so that each iteration now consists of two steps. First, we choose the point with the smallest tentative ϕ value and move that point to the solved set. Next, we (re)calculate tentative ϕ values for all its neighbouring points.

The fast marching algorithm for reinitialization proceeds as follows:

For points (x_i, y_j) "on" Γ, let $\phi(x_i, y_j) = 0$ and add the points (x_i, y_j) to the set **Solved**.

For each point adjacent to a **Solved** point, use its solved neighbours to assign it a tentative ϕ value by solving $|\nabla\phi| = 1$. Add these points to the set **TentativelySolved**.

Add all remaining points to the set **Unsolved**.

while Unsolved $\neq \emptyset$ **do**

Find the point $(x_i, y_j) \in$ **TentativelySolved** closest to Γ, i.e. that minimizes $|\phi(x_i, y_j)|$, and move it to **Solved**.

For each point adjacent to (x_i, y_j) not in **Solved**, use the neighbouring **Solved** values to (re)calculate tentative ϕ values and move the points to **TentativelySolved** if they were previously in **Unsolved**

end while

In practice, it is simpler to use the above method to calculate an *unsigned distance function*[5] and then correct the sign. As before, the method can be made more accurate by choosing higher order finite difference operators or by improving the accuracy of the initialization.

[5]I.e. a distance function that is everywhere positive.

3.2.3 The Poisson Problem

The velocity extension method we have described in the previous section presumes that we know the velocity of the boundary. In this section, we describe how we calculate this velocity.

Recall that the velocity in 2.10 is given by the following Poisson problem:

$$\nabla \cdot (\mathbf{M}\nabla p) = -\lambda \quad \text{on } \Omega \tag{3.4}$$

$$p = 0 \quad \text{on } \Gamma_{\Omega,f} \tag{3.5}$$

$$\mathbf{M}\nabla p \cdot \hat{n} = 0 \quad \text{on } \Gamma_{\Omega,w} \tag{3.6}$$

We will solve this problem using a variation of the fictitious domain finite element scheme outlined in [45]: the Dirichlet boundary terms are implemented using Nitsche's method [52] with ghost penalty stabilization terms added to handle small cuts [13], and a mesh transformation is used to map Ω to a domain defined by a piecewise linear level set function, allowing us to simplify the numerical integration without sacrificing higher-order accuracy. We briefly define each of these terms below.

Finite element methods [12] are a class of numerical methods that discretize the weak formulation of PDEs. We obtain a weak formulation of the Poisson equation by multiplying Equation 3.4 by a function, q, and applying the divergence theorem. This yields:

$$\int_\Omega (\mathbf{M}\nabla p) \cdot \nabla q dA - \int_{\Gamma_{\Omega,f}} q\,(\mathbf{M}\nabla p) \cdot \hat{n} dS = \int_\Omega \lambda q dA \tag{3.7}$$

Whereas the strong Poisson problem entails finding a twice-differentiable function p that solves 3.4, the weak version of the Poisson problem entails finding a function $p \in V$ such that Equation 3.7 holds for all $q \in V$, where V is some function space which will typically depend on the boundary conditions of the PDE (we will explain how below). For the Poisson problem, we will take V to be some subspace[6] of $H^1(\Omega)$, i.e. the space of weakly differentiable functions f on Ω such that f, $\partial_x f$, and $\partial_y f$ are all square-integrable. Note that p is not required to be twice-differentiable as it was in the original Poisson problem. This is a general feature of weak formulations: they admit a larger set of potential solutions. It is possible that a weak formulation may admit solutions that the original PDE does not.

Finite element methods discretize the weak formulation of a PDE by approximating V with a finite-dimensional function space. This is done by decomposing the domain Ω

[6] It is also possible to use functions that are not within a subspace of $H^1(\Omega)$, but which can approximate functions in $H^1(\Omega)$ to arbitrary accuracy. See, e.g., discontinuous Galerkin methods [22].

into several small subdomains[7], usually by triangulating the domain, and approximating V by a set of functions, V_h, defined piecewise on these subdomains. E.g.: If V is the set of continuous functions, we might replace V by the set of continuous functions that are piecewise polynomial on mesh elements. The fact that V_h is a finite-dimensional vector space means that instead of solving the weak problem for all $q \in V$, it suffices to solve the problem for all basis functions in V_h. This amounts to solving a large system of linear equations, i.e. inverting a matrix.

The particular problem we wish to solve involves a subdomain, Ω, embedded in a larger domain, D. We could, in principle, restrict our attention to Ω, using a *fitted* finite element scheme. This would provide us with a simple method to handle the boundary term in equation 3.7. If we choose $V = \{y \in H^1(\Omega) : y|_{\Gamma_{\Omega,f}} = 0\}$, the boundary term vanishes and the Dirichlet boundary conditions are satisfied automatically.

However, because Ω changes over time, this would require us to construct a new triangulation of Ω at every time step. This would be both computationally expensive and would require a not-inconsiderable amount of coding to define the geometry.[8] Instead, we use an *unfitted* approach. We construct a single triangulation of D, and solve a modified version of the Poisson problem on a subset $\Omega^e \subset D$. Note that a typical subdomain Ω will partially overlap certain mesh elements. Therefore, instead of solving the problem on Ω directly, we choose an extended subdomain $\Omega \subset \Omega^e$ such that Ω^e is composed of whole elements. The goal is to find a function p^e on Ω^e such that $p = p^e$ on Ω. This approach (solving a related problem on an extended domain Ω^e that restricts to the correct solution on Ω) is known as a *fictitious domain method*.

The fictitious domain method allows us to reuse the mesh throughout the dynamics. Unfortunately, because the boundary $\partial\Omega$ lies inside the domain Ω^e, we can no longer enforce the boundary conditions by choosing a suitable function space. Instead, we employ Nitsche's method [52]. We modify Equation 3.7, and solve the related problem:

$$\int_{\Omega^e} (\mathbf{M}\nabla p) \cdot \nabla q dA - \int_{\Gamma_{\Omega,f}} q\hat{n} \cdot (\mathbf{M}\nabla p) + p\hat{n} \cdot (\mathbf{M}\nabla q) + \gamma_N pq \, dS = \int_{\Omega^e} \lambda q dA \qquad (3.8)$$

Comparing with Equation 3.7, two terms have been added: the term $p\hat{n}\cdot(\mathbf{M}\nabla q)$ ensures that the bilinear form defined by the LHS symmetric, while the $\gamma_N pq$ term guarantees that it is coercive provided γ_N is large enough.[9] If we can also show that the bilinear form

[7] These subdomains are the "elements" from which the method gets its name.

[8] Finite element software typically includes easy-to-use tools to create simple domains like circles, rectangles, etc. but irregular domains must be custom-built.

[9] Choosing a suitable value for γ_N requires some care. We refer readers to [20].

is bounded, this is enough to apply the Lax–Milgram theorem and guarantee a unique solution.[10]. We may think of the constant γ_N as a penalty parameter. The intuition is this: if γ_N is large, and because q is arbitrary, we require p to be small at the boundary to ensure that the $\gamma_N pq$ term does not dominate.

The method we have described thus far will often produce adequate solutions, but it can occasionally fail. In particular, if the domain Ω has a very small overlap with one of the elements in Ω^e, the matrix we obtain by discretizing 3.8 can have a large condition number. To counteract this, we add a ghost penalty stabilization term to the LHS, as described by [58]. These terms take the form

$$\sum_{T_1 \cap T_2 \neq \emptyset} \gamma_g \int_{T_1 \cup T_2} h^{-2}[[p]][[q]]dA$$

where the T_i are defined as follows. Let F_{inner} be the set of elements strictly contained in Ω, and let F_{bdry} the set of elements in $\Omega^e \setminus F_{inner}$ (i.e. the set of elements intersected by $\partial\Omega$). We sum and integrate over all (adjacent) pairs $T_1 \in F_{inner}$, $T_2 \in F_{bdry}$. $[[f]]$ denotes the jump operator obtained by extending the piecewise polynomial components of f to neighbouring facets and taking the difference between the two, i.e. if f_i is a polynomial (defined on all of D) such that $f_i = f|_{T_i}$, then $[[f]] = f_1 - f_2$.

Intuitively, the effect of the ghost penalty term is to ensure that the part of the solution defined on the extended domain (i.e. inside Ω^e but outside Ω), is a smooth continuation of the solution defined on the interior of Ω. I.e. it prevents us from solving the problem by introducing large deviations in parts of the domain that we ultimately don't care about.

Finally, we note that the boundary integrals in 3.8 are, in general, defined on curves. There are not, to our knowledge, any off-the-shelf FEM tools capable of calculating such integrals. However, ngsolve [61], and in particular, the XFEM addon, ngsxfem [46], provides a way to approximate these integrals using integrals defined on a piecewise linear boundary (which is much easier to integrate). It does this by applying a mesh deformation that curves the piecewise linear boundary into a curved boundary that approximates $\partial\Omega$. We refer the reader to [44].

3.2.4 2D algorithm

We can now outline the basic 2D scheme to solve 2.10:

[10] This is a standard technique in the theory of PDEs. See, e.g., [12]

$t = T_{initial}$
while $t < T_{final}$ **do**
Convert the finite difference representations of ϕ, Q_{11}, and Q_{12} to FEM representations.[a]
Use the FEM representations of ϕ to partition the FEM domain into sections.
Solve[b] the boundary value problem:

$$\begin{aligned} \nabla \cdot (\mathbf{M}\nabla p) &= -\lambda && \text{on } \Omega \\ p &= 0 && \text{on } \partial\Omega \end{aligned}$$

Use p to calculate finite difference representations of $\vec{v}$, $\mathbf{u}$ and $\boldsymbol{\omega}$.
Let $\Delta t = \min\left(\Delta t_{max}, \frac{h}{4||v_h||_\infty}\right)$
Use a linear upwind differencing scheme to calculate the transport terms for ϕ, Q_{11}, and Q_{12}.
Advance the transport equation for ϕ and the Beris-Edwards equations for Q_{11} and Q_{12} using a forward Euler scheme.
$t \mathrel{+}= \Delta t$
end while

[a] We use the VoxelCoefficient class from ngsolve [61].
[b] We solve this using the ngsolve [61] with the ngsxfem add-on [46], using the scheme described in 3.2.3

3.3 Near-incompressible Model

Recall the near-incompressible model(s), i.e. equations 2.12, 2.13, and 2.14. We will outline a simple numerical implementation of the following system. The other variations are treated similarly.

$$\begin{aligned} \partial_t b + \nabla \cdot (b\vec{v}) &= \lambda b \\ (\partial_t + \vec{v} \cdot \nabla)(b\vec{v}) &= -\mathbf{M}\nabla p - \mu b\vec{v} \\ (\partial_t + \vec{v} \cdot \nabla)Q_{\alpha\beta} &= 2\xi u_{\alpha\beta} + \omega_{\alpha\gamma}Q_{\gamma\beta} - Q_{\alpha\gamma}\omega_{\gamma\beta} - \xi \mathrm{tr}(\mathbf{uQ})Q_{\alpha\beta} + \Gamma H_{\alpha\beta} \end{aligned}$$

where $p = \begin{cases} A\,(b - b_p)^k & \text{if } b \geq b_p \\ 0 & \text{if } b < b_p \end{cases}$.

Unlike the incompressible system, this system can be implemented using only elementary finite difference methods. One could devise a more sophisticated scheme, but as our

goal is merely to compare/contrast these near-incompressible models to model 2.10, the following will suffice. We use the forward Euler method to discretize the time derivatives, and the central difference method to discretize most spatial derivatives. The only exception to this are the transport terms in the momentum and Beris-Edwards equations, which we treat using a linear upwind differencing scheme.

For ease of implementation, we treat momentum, $b\vec{v}$, as a single variable, rather than the velocity, $\vec{v}$. When the velocity is needed (e.g. for the advection terms), we compute $\vec{v} = b\vec{v}/b$, except when b is small (10% of b_p), in which case we set $\vec{v}$ to zero. We also add a small diffusion term to the evolution equation for density, which is required for numerical stability.

The only unusual feature of our discretization are the boundary conditions. The no-flux boundary conditions on the walls are treated in the standard way, but the absorbing boundary conditions on the open face(s) require more care. We apply staggered boundary conditions. Each open boundary is padded with an extra region. At the "true" boundary, we treat diffusion terms as if there was a wall present, but we allow the advection terms to extend beyond the true domain into the extended region. At the end of each time step, we manually set the values of b, $b\vec{v}$, and $\mathbf{Q}$ to be zero in the padded region.

Define coordinates for the extended domain, $D_{ext} = D \cup Padd$, where $Padd$ is a set of thin regions that extend the original domain beyond the open boundaries.
Initialize b, $b\vec{v}$, and $\mathbf{Q}$
$t = T_{initial}$
while $t < T_{final}$ **do**
  Calculate $\vec{v} = b\vec{v}/\max(b, 0.1)$
  Calculate $\Delta t = \min\left(\Delta t_{max}, \frac{h}{4||v_h||_\infty}\right)$
  Calculate $\nabla \cdot (b\vec{v})$, ∇p, $\mathbf{u}$, and $\boldsymbol{\omega}$ on the extended domain, D_{ext} using central difference operators, applying no-flux boundary conditions on all boundaries. Calculate Δb and $\Delta Q_{\alpha\beta}$ using central difference operators on the true domain, D, applying reflecting boundary conditions to all boundaries.
  Calculate $\vec{v} \cdot \nabla(b\vec{v})$ and $\vec{v} \cdot \nabla\mathbf{Q}$ using linear upwind differencing.
  Update b, $b\vec{v}$, and $\mathbf{Q}$ using a forward Euler scheme.
  Set b, $b\vec{v}$, and $\mathbf{Q}$ to zero in $Padd$.
  $t \mathrel{+}= \Delta t$
end while

Having described numerical implementations for each of the models we have proposed in this thesis, we are now adequately equipped to investigate their behaviour.

Chapter 4

Model Behaviour

In this section, we discuss the behaviour of the models we developed in Chapter 2. We first examine exact solutions, expanding on the observations about moving boundaries made in Section 2.2 and the effects of γ in Section 2.3.1, and use these to verify the numerical implementation(s) proposed in Chapter 3. Finally, we will use the numerical models to explore more complex scenarios where exact solutions are lacking. We find that the model exhibits several of the phenomena observed in real microcolonies: spontaneous organization in confined domains, fingering at the boundary, and defect generation.

4.1 1D Dynamics

We begin with an examination of the 1-dimensional incompressible system (i.e. equations 3.1). The dynamics of this model are significantly less rich than its 2-dimensional counterpart, in large part due to the absence of directional dependence. Nevertheless, it can illustrate one of the key features of our system: cell motion caused by the combination of growth and incompressibility.

We saw in Section 2.2 that we could find exact solutions to the 1D incompressible growth system. In general, the domain splits into intervals where the density is either fully packed ($b(x,t) = b_p$) or growing exponentially ($b(x,t) = b(x,0)e^{\lambda t}$). The boundary points of these intervals obey differential equations of the form

$$x_i'(t) = \frac{b_p}{b_p - b(x_i^{\pm})} v(x_i^{\mp})$$

where $v(x_i^{\mp})$ is the velocity at the boundary of the packed interval, and the denominator, $b_p - b(x_i^{\pm})$, is the density jump at x_i.

In particular, we saw that for domain $D = [0, L]$ with a wall at $x = 0$, an open boundary at $x = L$, and $b_p = 1$, given the initial condition

$$b(x, 0) = \begin{cases} 1 & \text{if } x \in [0, x_b(0)] \\ 0.1 & \text{if } x \in (x_b(0), L] \end{cases}$$

the following solution holds:

$$b(x, t) = \begin{cases} 1 & \text{if } x \in [0, x_b(t)] \\ 0.1e^t & \text{if } x \in (x_b(t), L] \end{cases}$$

$$p(x, t) = \begin{cases} -\frac{\lambda}{2}x^2 & \text{if } x \in [0, x_b(t)] \\ 0 & \text{if } x \in (x_b(t), L] \end{cases}$$

$$v(x, t) = \begin{cases} \lambda x & \text{if } x \in [0, x_b(t)] \\ 0 & \text{if } x \in (x_b(t), L] \end{cases}$$

$$x_b(t) = x_b(0)\frac{9e^t}{10 - e^t}$$

The top plot in Figure 4.1 shows the numerical solution of the above problem, calculated using the scheme from Section 3.1, plotted against the exact solution. The bottom plot of the same figure illustrates the squared difference between the exact and the computed solution. Table 4.1 compiles the average errors over the duration of the simulation for each of the three regions of the domain: the close-packed region, the non-packed region, and the boundary between the two. We define the boundary region to be the interval

$$[\min(x_b(t), x_{b,approx}(t)) - 5\Delta x, \max(x_b(t), x_{b,approx}(t)) + \Delta x]$$

where $x_{b,approx}(t)$ is the location of the boundary in the simulation.

All regions display the same linear rate of convergence. Notice, however, that in the close-packed region, the error does not drop significantly between $n = 1000$ and $n = 2000$. This is because our numerical implementation depends on a second parameter that acts as a bottleneck to further convergence. Recall that in the numerical implementation described in Section 2.2, we modified the pressure equation by introduced a restoring force that depended on a parameter k. As a result, the density in the close-packed region converges to $b_p(1 + \lambda k)$, and not to b_p as in the exact model. The errors in Table 4.1 were obtained

using $k = 50$. In order to achieve further accuracy in the close-packed region, we must increase k.

Of the three regions, the boundary is the largest source of error. This highlights the need to treat it with special care. In the following sections, we will turn our attention to the 2-dimensional system. In our numerical implementation of this system, the density in the close-packed region is equal to b_p by definition (in contrast to the 1-dimensional implementation where the density in the close-packed region is computed). In addition, we will restrict our attention to cases where the density outside the close-packed region is zero. Therefore, the only sources of error we will consider are the location of the boundary, $\partial\Omega$, and the value of the Q-tensor.

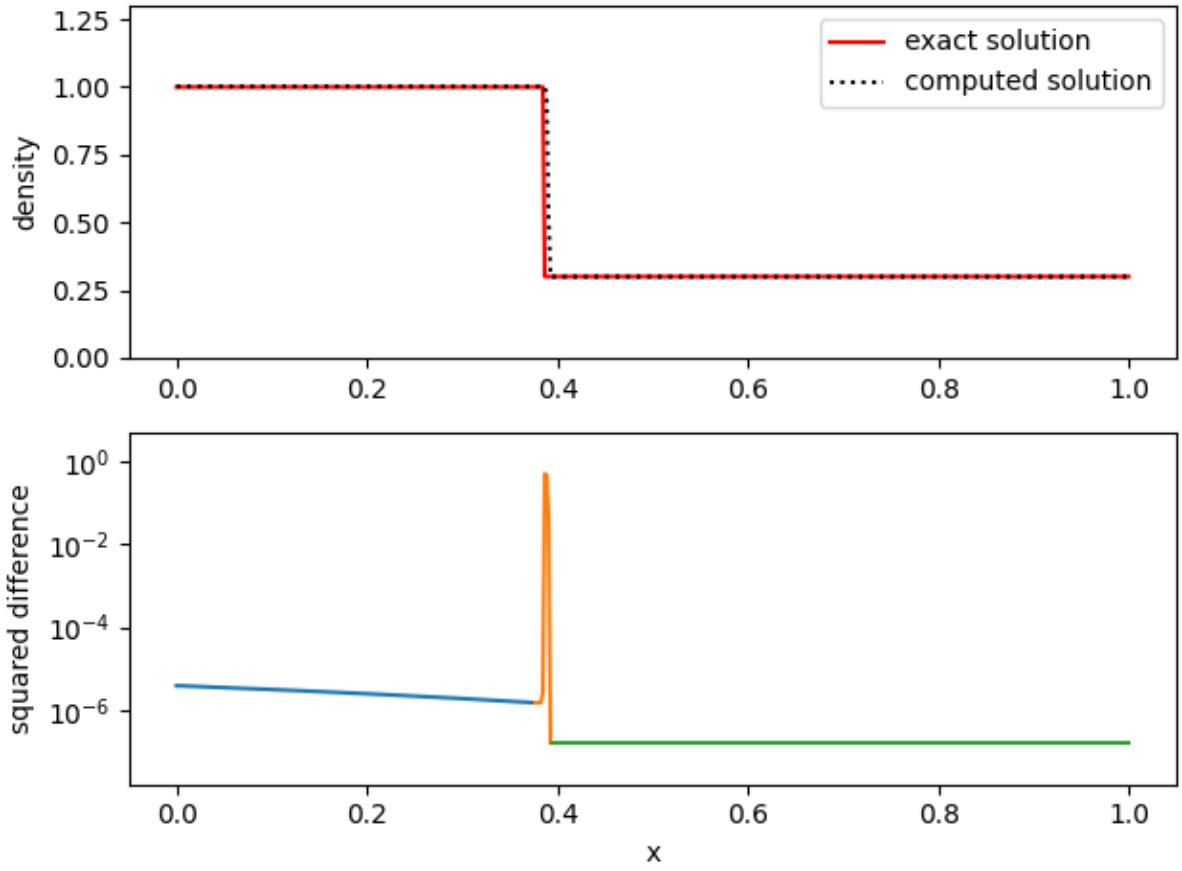

Figure 4.1: (a) Computed vs exact solution for $n = 500$, $k = 50$, $t = 1.1$. (b) Squared difference in the exact and computed solutions in figure (a) colour coded by region: close-packed region (blue), the boundary region (orange), and the non-packed region (green).

n	L_2 error in packed region	L_2 error in boundary region	L_2 error in non-packed region
250	1.4108e-4 ± 2.0125e-4	2.6996e-3 ± 1.6427e-3	2.6517e-5 ± 2.9166e-5
500	4.9053e-5 ± 5.5621e-5	1.2886e-4 ± 7.6738e-4	1.0740e-5 ± 8.7385e-6
1000	2.7828e-5 ± 6.3282e-6	5.8669e-4 ± 2.9562e-4	3.4076e-6 ± 2.0065e-6
2000	2.0998e-5 ± 6.2681e-6	2.4908e-4 ± 8.9798e-5	1.1774e-6 ± 6.9986e-7

Table 4.1: L_2 errors between the computed and exact solution in each of the three solution regions. Errors were averaged over time for a simulation lasting from $t = 0$ until either $x_b(t)$ or $x_{b,approx}(t)$ leaves the domain, $t \approx 1.5$. Errors bars represent the corresponding standard deviation.

4.2 2D Validation

Before looking at the dynamics of the full 2-dimensional model, we should verify that our implementation is working as intended, beginning with the pressure calculation, as described in Section 3.2.3, and moving on to some simple cases where we can describe the dynamics of the full system exactly.

4.2.1 2D Velocity Calculation

We begin by isolating the velocity calculation from the rest of the model dynamics. The method we outlined in Section 3.2.3 differs from [45] by the presence of the matrix $\mathbf{M}$, so we should verify that this does not invalidate the method.

Recall from Section 2.3.1, that when cells are uniformly aligned horizontally (i.e. when $\mathbf{Q} = S\begin{bmatrix} 1 & 0 \\ 0 & -1 \end{bmatrix}$ for some constant value of S), the Poisson problem

$$\begin{aligned} \nabla \cdot \mathbf{M}\nabla p &= -\lambda && \text{on } \Omega \\ p &= 0 && \text{on } \partial\Omega \\ \Omega &= \left\{ (x,y) \in \mathbb{R}^2 \middle| \frac{x^2}{a^2} + \frac{y^2}{b^2} \leq 1 \right\} \end{aligned}$$

admits the solution $p = -\frac{\lambda}{2}\frac{a^2b^2(1+2S\gamma)}{a^2+b^2(1+2S\gamma)}\left(\frac{x^2}{a^2}+\frac{y^2}{b^2}-1\right)$. The corresponding velocity field is:

$$\vec{v} = \frac{\lambda}{a^2+b^2(1+2S\gamma)}\begin{bmatrix} b^2(1+2S\gamma)x \\ a^2 y \end{bmatrix}$$

Figure 4.2 shows the computed values for p (panel a) and $\vec{v}$ (panel b), calculated on a circular domain (i.e. $a = b$ in the above) using the method presented in Section 3.2.3. Figure 4.3 illustrates the L_2 error in the computed value of p as a function of the mesh resolution. All calculations were performed using continuous, piecewise quadratic functions. We see from Figure 4.3 that the method displays the same rate of convergence regardless of the value of γ[1], providing evidence that our extension of [45] is sound.

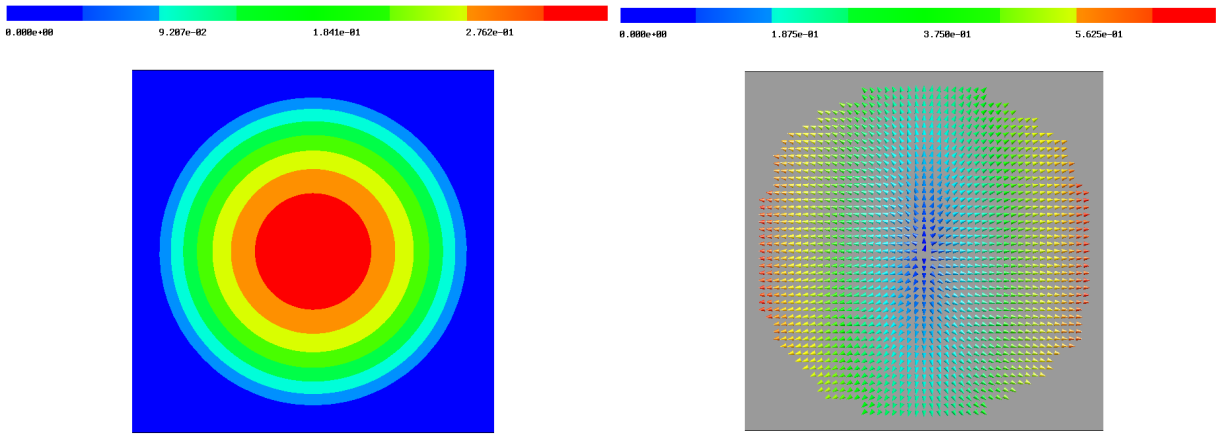

(a) (b)

Figure 4.2: Computed values for (a) p and (b) $\vec{v}$ for a circular microcolony of horizontally aligned cells. Model parameters are $\gamma = \lambda = 1$. Note that $\vec{v}$ is plotted on the extended/fictitious domain.

[1]Recall that $\mathbf{M} = \frac{1+S\gamma}{1+2S\gamma}\mathbf{I} + \frac{\gamma}{1+2S\gamma}\mathbf{Q}$, so γ controls the degree to which $\mathbf{M}$ deviates from the identity matrix. In effect, γ measures how much our implementation deviates from the original scheme proposed in [45].

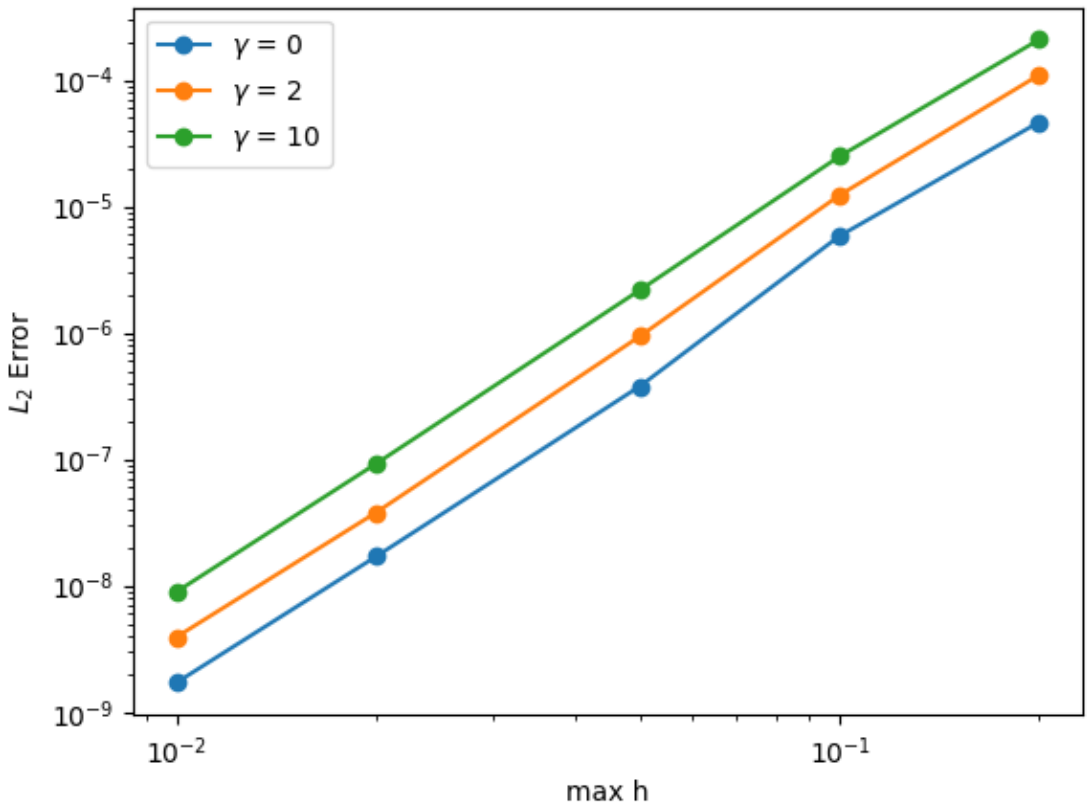

Figure 4.3: L_2 difference between the exact solution and the numerical solution for circle of radius 1 with $\lambda = 1$. The x-axis, max h, represents the maximal element size. We observe the same $O(h^3)$ convergence reported in [45].

4.2.2 Elliptical Solutions

The results from the previous section only concern the calculation of the velocity field at a single time point. In order to confirm that the full implementation works as expected, we need a solution to the full system, i.e. Equations 2.10. To this end, we will extend the velocity profile from Section 2.3.1.

Proposition 4.2.1. *The following*

$$b(x,y,t) = \begin{cases} b_p & (x,y) \in \Omega \\ 0 & \textit{otherwise} \end{cases}$$

$$\vec{v} = \frac{\lambda}{a_1^2 + a_2^2(1+2S\gamma)} \begin{bmatrix} a_2^2(1+2S\gamma)x \\ a_1^2 y \end{bmatrix}$$

$$\mathbf{Q}(t,x,y) = S(t) \begin{bmatrix} 1 & 0 \\ 0 & -1 \end{bmatrix}$$

$$\Omega(t) = \left\{ (x,y) \in \mathbb{R}^2 \middle| \frac{x^2}{a_1(t)^2} + \frac{y^2}{a_2(t)^2} \leq 1 \right\}$$

is a solution to Equations 2.10, provided that $S(t)$, $a_1(t)$, and $a_2(t)$ satisfy the following system of differential equations:

$$S' = \xi\lambda \frac{a_2^2(1+2S\gamma) - a_1^2}{a_2^2(1+2S\gamma) + a_1^2}(1-S^2) + A_0 b_p (S_{eq}^2 - S^2)S \tag{4.1}$$

$$a_1' = \lambda \frac{a_1 a_2^2 (1+2S\gamma)}{a_1^2 + a_2^2(1+2S\gamma)} \tag{4.2}$$

$$a_2' = \lambda \frac{a_1^2 a_2}{a_1^2 + a_2^2(1+2S\gamma)} \tag{4.3}$$

Proof. It is easy to verify that the first two equations, for b and $\vec{v}$, satisfy 2.10 for $\mathbf{Q}$ and Ω stated above, so we need only check that $\mathbf{Q}$ satisfies the Beris-Edwards Equation 1.8 and that the evolution of Ω is compatible with the velocity field $\vec{v}$. We begin with $\mathbf{Q}$. Recall the Beris-Edwards equation:

$$\partial_t \mathbf{Q} = -\vec{v} \cdot \nabla \mathbf{Q} + 2\xi \mathbf{u} + \boldsymbol{\omega}\mathbf{Q} - \mathbf{Q}\boldsymbol{\omega} - \xi \mathrm{tr}(\mathbf{u}\mathbf{Q})\mathbf{Q} + A_0 b_p (S_{eq}^2 - S^2)\mathbf{Q} + K\Delta\mathbf{Q}$$

We calculate $\mathbf{u}$, $\boldsymbol{\omega}$, and $\mathrm{tr}(\mathbf{uQ})$.

$$\mathbf{u} = \begin{bmatrix} \frac{\lambda}{2}\frac{a_2^2(1+2S\gamma)-a_1^2}{a_2^2(1+2S\gamma)+a_1^2} & 0 \\ 0 & \frac{\lambda}{2}\frac{a_1^2-a_2^2(1+2S\gamma)}{a_1^2+a_2^2(1+2S\gamma)} \end{bmatrix}$$

$$\boldsymbol{\omega} = \begin{bmatrix} 0 & 0 \\ 0 & 0 \end{bmatrix}$$

$$\begin{aligned} \mathrm{tr}(\mathbf{uQ}) &= (u_{11} - u_{22})Q_{11} + 2u_{12}Q_{12} \\ &= \lambda \frac{a_2^2(1+2S\gamma) - a_1^2}{a_2^2(1+2S\gamma) + a_1^2} S \end{aligned}$$

Substituting the above into the RHS of the Beris-Edwards equation, along with $\mathbf{Q} = S(t)\begin{bmatrix} 1 & 0 \\ 0 & -1 \end{bmatrix}$, we obtain:

$$\begin{aligned} RHS &= -\vec{v}\cdot\nabla\mathbf{Q} + 2\xi\mathbf{u} + \boldsymbol{\omega}\mathbf{Q} - \mathbf{Q}\boldsymbol{\omega} - \xi\,\mathrm{tr}(\mathbf{uQ})\mathbf{Q} + A_0 b_p(S_{eq}^2 - S^2)\mathbf{Q} + K\Delta\mathbf{Q} \\ &= 0 + \xi\lambda\frac{a_2^2(1+2S\gamma) - a_1^2}{a_2^2(1+2S\gamma) + a_1^2}\begin{bmatrix} 1 & 0 \\ 0 & -1 \end{bmatrix} + 0 - 0 \\ &\quad - \xi\lambda\frac{a_2^2(1+2S\gamma) - a_1^2}{a_2^2(1+2S\gamma) + a_1^2}S^2\begin{bmatrix} 1 & 0 \\ 0 & -1 \end{bmatrix} + A_0 b_p(S_{eq}^2 - S^2)S\begin{bmatrix} 1 & 0 \\ 0 & -1 \end{bmatrix} + 0 \\ &= \left(\xi\lambda\frac{a_2^2(1+2S\gamma) - a_1^2}{a_2^2(1+2S\gamma) + a_1^2}(1-S^2) + A_0 b_p(S_{eq}^2 - S^2)S\right)\begin{bmatrix} 1 & 0 \\ 0 & -1 \end{bmatrix} \end{aligned}$$

Substituting into the LHS of the Beris-Edwards equation yields

$$LHS = S'(t)\begin{bmatrix} 1 & 0 \\ 0 & -1 \end{bmatrix}$$

Thus, $\mathbf{Q} = S(t)\begin{bmatrix} 1 & 0 \\ 0 & -1 \end{bmatrix}$ is a solution to the Beris-Edwards equation compatible with $\vec{v}$, provided that S evolves according to 4.1.

It remains to be shown that the evolving elliptical domain is also compatible with $\vec{v}$. Suppose $a_1(t)$ and $a_2(t)$ are, for now, arbitrary functions of time, and consider the path

of a point $(x(t), y(t)) \in \mathbb{R}^2$ subject to a velocity field of the form 2.11. In other words, suppose $x(t)$ and $y(t)$ satisfy

$$x'(t) = \lambda \frac{a_2^2(1+2S\gamma)}{a_1^2 + a_2^2(1+2S\gamma)} x$$
$$y'(t) = \lambda \frac{a_1^2}{a_1^2 + a_2^2(1+2S\gamma)} y$$

By separation of variables, we find

$$x(t) = x(0) e^{\lambda \int_0^t \frac{a_2^2(1+2S\gamma)}{a_1^2+a_2^2(1+2S\gamma)} d\tau}$$
$$y(t) = y(0) e^{\lambda \int_0^t \frac{a_1^2}{a_1^2+a_2^2(1+2S\gamma)} d\tau}$$

Or, written in matrix form:

$$\begin{bmatrix} x(t) \\ y(t) \end{bmatrix} = \begin{bmatrix} e^{\lambda \int_0^t \frac{a_2^2(1+2S\gamma)}{a_1^2+a_2^2(1+2S\gamma)} d\tau} & 0 \\ 0 & e^{\lambda \int_0^t \frac{a_1^2}{a_1^2+a_2^2(1+2S\gamma)} d\tau} \end{bmatrix} \begin{bmatrix} x(0) \\ y(0) \end{bmatrix}$$

This linear transformation corresponds to a rescaling of the x and y axes. Applying this linear transformation to an ellipse of the form $\frac{x^2}{A^2} + \frac{y^2}{B^2} = 1$ will yield a new ellipse given by:

$$\frac{x^2}{\left(A e^{\lambda \int_0^t \frac{a_2^2(1+2S\gamma)}{a_1^2+a_2^2(1+2S\gamma)} d\tau} \right)^2} + \frac{y^2}{\left(B e^{\lambda \int_0^t \frac{a_1^2}{a_1^2+a_2^2(1+2S\gamma)} d\tau} \right)^2} = 1 \tag{4.4}$$

We showed in Section 2.3.1 that an elliptical domain filled with horizontal cells will induce a velocity field of the form 2.11, and we have just shown that a velocity field of the form 2.11 will leave horizontal cells horizontal and elliptical domains elliptical. However, if we want a valid solution to equations 2.10, we require that Ω and $\vec{v}$ be self-consistent. I.e. we require that the denominators in equation 4.4 correspond to the as yet unspecified functions $a_1(t)$ and $a_2(t)$ in $\vec{v}$.

In this case we find that $a_1(t) = a_1(0) e^{\lambda \int_0^t \frac{a_2^2(1+2S\gamma)}{a_1^2+a_2^2(1+2S\gamma)} d\tau}$ and $a_2(t) = a_2(0) e^{\lambda \int_0^t \frac{a_1^2}{a_1^2+a_2^2(1+2S\gamma)} d\tau}$. Differentiating the equations, we recover equations 4.2 and 4.3, as desired. □

Equations 4.1-4.3 admit a particularly simple solution in the case where the ellipse maintains a fixed eccentricity. Differentiating a_1/a_2, we obtain:

$$\begin{aligned}\left(\frac{a_1}{a_2}\right)' &= \frac{a_1' a_2 - a_2' a_1}{a_2^2} \\ &= \frac{\lambda \frac{a_1 a_2^2(1+2S\gamma)}{a_1^2+a_2^2(1+2S\gamma)} a_2 - \lambda \frac{a_1^2 a_2}{a_1^2+a_2^2(1+2S\gamma)} a_1}{a_2^2} \\ &= \lambda \frac{a_1}{a_2} \frac{a_2^2(1+2S\gamma) - a_1^2}{a_2^2(1+2S\gamma) + a_1^2}\end{aligned}$$

Thus, the eccentricity is constant if $\frac{a_1}{a_2} = \sqrt{1+2S\gamma}$. The RHS of this equation is constant if and only if S is constant. However, when $a_1 = a_2\sqrt{1+2S\gamma}$, equation 4.1 simplifies to $S' = A_0 b_p (S_{eq}^2 - S^2)S$. Therefore, fixed eccentricity solutions will also satisfy either $S = 0$ (the trivial, circular solution), $S = S_{eq}$, or $A_0 = 0$.

Notice also that a_1 and a_2 will, in general, satisfy the following:

$$\begin{aligned}(\ln(a_1 a_2))' &= \frac{a_1'}{a_1} + \frac{a_2'}{a_2} \\ &= \lambda \frac{a_2^2(1+2S\gamma)}{a_1^2 + a_2^2(1+2S\gamma)} + \lambda \frac{a_1^2}{a_1^2 + a_2^2(1+2S\gamma)} \\ &= \lambda\end{aligned}$$

Solving this ODE yields $a_1(t)a_2(t) = a_1(0)a_2(0)e^{\lambda t}$. Combining this identity with the constant eccentricity conditions derived above, we arrive at exact solutions for a_1 and a_2.

$$\begin{aligned}a_1(t) &= a_1(0)e^{\frac{\lambda}{2}t} \\ a_2(t) &= a_2(0)e^{\frac{\lambda}{2}t}\end{aligned}$$

For the above to be valid we require that the initial condition satisfies $a_1(0) = a_2(0)\sqrt{1+2\gamma S}$.

Figure 4.4a shows simulation results for the evolution of the elliptical solution using the numerical method outlined in Section 3.2.4. Figure 4.4b shows the values of $a_1(t)$, $a_2(t)$, and $S(t)$ extracted from the simulated elliptical solution, plotted against the values predicted by equations 4.1-4.3.

Table 4.2 shows the error between the exact and computed solution as a function of the resolution of the finite difference mesh. The rate of convergence is not clear, though the error in a_1 suggests an approximately linear trend for that component. Curiously,

the error in a_2 increases from $n = 200$ to $n = 400$. This may be due to more frequent reinitialization. As in the 1-dimensional case, the analysis is complicated by the presence of other parameters that can influence the accuracy of the simulation, including the resolution of the finite element mesh (max h in figure 4.3) and the frequency of level set reinitialization.

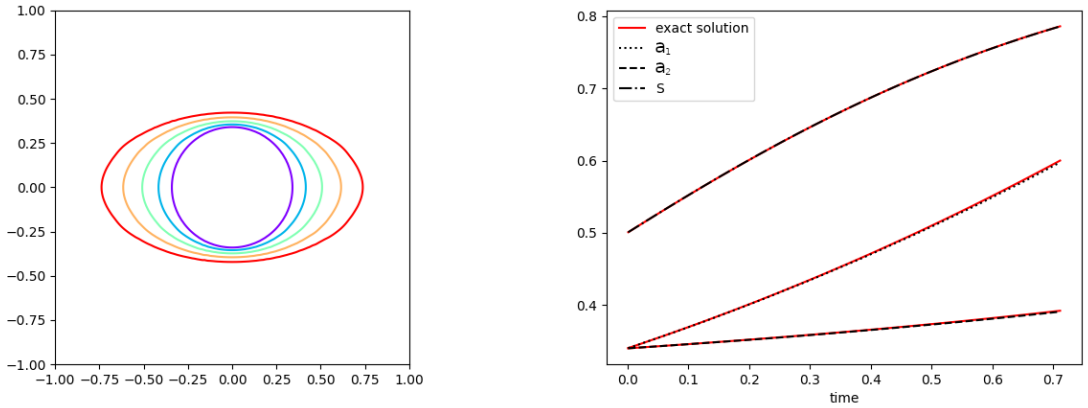

(a) (b)

Figure 4.4: (a) General elliptical solution, sampled at intervals of approximately $\Delta t = 0.25$. Simulation parameters are $\gamma = 4$, $\xi = 0.5$, $A_0 = 1$, $S_{eq} = 0.9$, $b_p = 1$, and $K = 0.001$. (b) $a_1(t)$, $a_2(t)$, and $S(t)$ in the general case plotted against the values predicted by equations 4.1-4.3. The simulated value of S was measured in the center of the domain.

n	Error in $a_1(0.25)$	Error in $a_2(0.25)$	Error in $S(0.25)$
100x100	2.0237e-3	3.8488e-4	8.1018e-4
200x200	1.1571e-3	2.1303e-4	4.3664e-4
400x400	2.7887e-4	2.7990e-4	3.9149e-5
n	Error in $a_1(0.5)$	Error in $a_2(0.5)$	Error in $S(0.5)$
100x100	4.8483e-3	1.1456e-3	1.6076e-3
200x200	2.8167e-3	6.3920e-4	6.5378e-4
400x400	1.3920e-3	6.4778e-4	7.1634e-5

Table 4.2: The values of $a_1(t)$, $a_2(t)$, and $S(t)$ were extracted from a simulation of the elliptical solution. This table presents the magnitude of the difference between these extracted values and the exact solution obtained by solving equations 4.1-4.3.

These checks provide some confidence that our numerical implementation is sound. All the basic features—the evolution of the boundary, the dynamics of $\mathbf{Q}$, and the coupling of velocity to the Q-tensor—behave as expected. The only significant blind spot in our analysis regards inhomogeneities in the Q-tensor. We have only considered spatially homogeneous solutions. Unfortunately, we have no exact solutions in the inhomogeneous case, so this marks the end of our model validation.

4.3 2D Dynamics

While real microcolonies often display local order, they are seldom globally homogeneous. In this section, we investigate the evolution of inhomogeneous solutions to 2.10.

4.3.1 Spontaneous Alignment in Semi-confined Domains

Experiments show that rod-shaped bacteria grown in semi-confined environments exhibit spontaneous global alignment, tending towards a uniform steady-state [69][15]. Volfson *et al.* [69] were able to replicate this behaviour with their 1-dimensional model. Our model also replicates this behaviour, as we will show in this section.

We begin by considering the case $\gamma = 0$. In this case, we can obtain an analytic description of the solution of 2.10 in rectangular domains, as we will now show.[2]

Proposition 4.3.1. *Let $D = [0, L] \times [0, 1]$ be a domain of length L with walls at $x = 0$, $y = 0$, and $y = 1$, and an open boundary at $x = L$. Suppose $\gamma = 0$ (i.e. $\mathbf{M} = \mathbf{I}$), and suppose the domain is fully packed (i.e. $\Omega = D$).*

In the absence of thermodynamic terms (i.e. $A_0 = K = 0$), the uniformly horizontal steady state $\mathbf{Q} = \begin{bmatrix} 1 & 0 \\ 0 & -1 \end{bmatrix}$ is globally asymptotically stable.

Proof. In this case, $\vec{v} = [\lambda x, 0]^{\mathrm{T}}$, from which it follows that

$$\mathbf{u} = \begin{pmatrix} \frac{\lambda}{2} & 0 \\ 0 & -\frac{\lambda}{2} \end{pmatrix}$$

[2] We can also interpret these results as descriptions of the *local* behaviour of solutions in parts of the domain where the vorticity is small. When $\boldsymbol{\omega} \approx 0$, cells will tend to align with the flow.

$$\boldsymbol{\omega} = \begin{pmatrix} 0 & 0 \\ 0 & 0 \end{pmatrix}$$

and therefore the Beris-Edwards equations simplify to the following.

$$\partial_t Q_{11} + \lambda x \partial_x Q_{11} = \xi\lambda(1 - Q_{11}^2)$$
$$\partial_t Q_{12} + \lambda x \partial_x Q_{12} = -\xi\lambda Q_{11} Q_{12}$$

Along streamlines, the Q_{11} equation ensures that Q_{11} will tend towards 1 at a rate determined by $\xi\lambda$. Once Q_{11} enters the positive range, the Q_{12} equation then causes Q_{12} to exponentially decay at a rate of $\xi\lambda Q_{11}$. (This rate tends towards $\xi\lambda$ as Q_{11} tends to 1.) Thus, the system converges towards the uniformly horizontal steady state. □

If we add the thermodynamic terms but set the elastic/diffusion terms to zero ($K = 0$), the qualitative behaviour is similar, but the steady state value of S is different.

Proposition 4.3.2. *Let $D = [0, L] \times [0, 1]$ be a domain of length L with walls at $x = 0$, $y = 0$, and $y = 1$, and an open boundary at $x = L$. Suppose $\gamma = 0$ (i.e. $\mathbf{M} = \mathbf{I}$), and suppose the domain is fully packed (i.e. $\Omega = D$).*

If $K = 0$, the uniformly horizontal steady state $\mathbf{Q} = S^{ss} \begin{bmatrix} 1 & 0 \\ 0 & -1 \end{bmatrix}$ is the unique locally stable steady state, for some constant $S_{eq} \leq S^{ss} \leq 1$.

Proof. As before, $\vec{v} = [\lambda x, 0]^{\mathrm{T}}$. In this case, the Beris-Edwards equations read:

$$\partial_t Q_{11} + \lambda x \partial_x Q_{11} = \xi\lambda(1 - Q_{11}^2) + A_0 b_p (S_{eq}^2 - S^2) Q_{11}$$
$$\partial_t Q_{12} + \lambda x \partial_x Q_{12} = -\xi\lambda Q_{11} Q_{12} + A_0 b_p (S_{eq}^2 - S^2) Q_{12}$$

Relabelling $A_0 b_p = A$ and expanding $S^2 = Q_{11}^2 + Q_{12}^2$, we obtain:

$$\begin{aligned} \partial_t Q_{11} + \lambda x \partial_x Q_{11} &= \xi\lambda(1 - Q_{11}^2) + A(S_{eq}^2 - Q_{11}^2 - Q_{12}^2) Q_{11} \\ &= \xi\lambda + \left(A(S_{eq}^2 - Q_{11}^2 - Q_{12}^2) - \xi\lambda Q_{11}\right) Q_{11} \end{aligned}$$

$$\begin{aligned} \partial_t Q_{12} + \lambda x \partial_x Q_{12} &= -\xi\lambda Q_{11} Q_{12} + A(S_{eq}^2 - Q_{11}^2 - Q_{12}^2) Q_{12} \\ &= \left(A(S_{eq}^2 - Q_{11}^2 - Q_{12}^2) - \xi\lambda Q_{11}\right) Q_{12} \end{aligned}$$

For clarity, let $f(\mathbf{Q}) = A(S_{eq}^2 - Q_{11}^2 - Q_{12}^2) - \xi\lambda Q_{11}$. We rewrite the system above as follows.

$$\partial_t Q_{11} + \lambda x \partial_x Q_{11} = \xi\lambda + f(\mathbf{Q})Q_{11} \tag{4.5}$$
$$\partial_t Q_{12} + \lambda x \partial_x Q_{12} = f(\mathbf{Q})Q_{12} \tag{4.6}$$

Again, we look for steady-state solutions following the flow. We see from equation 4.5 that there are no steady state solutions when $f(\mathbf{Q}) = 0$. Thus, from equation 4.6, the steady-state solutions require that $Q_{12} = 0$, i.e. the cells are aligned horizontally.

We could also write equation 4.5 as $\partial_t Q_{11} + \lambda x \partial_x Q_{11} = g(Q_{11}) - AQ_{12}^2 Q_{11}$ where $g(x) = \xi\lambda + AS_{eq}^2 x - \xi\lambda x^2 - Ax^3$. Therefore, finding the steady state Q_{11} value amounts to finding the root(s) of g.

We see that $g(0) = \xi\lambda > 0$ and $g(1) = -A(1 - S_{eq}^2)$. Because $1 > S_{eq}$ by definition, it follows that g has at least one root in the interval $(0, 1)$. Moreover, by Descartes' rule of signs, this is the only positive root (call it S^{ss}).

We can narrow the location of this root even further. Note that

$$\begin{aligned} g(S_{eq}) &= \xi\lambda + AS_{eq}^3 - \xi\lambda S_{eq}^2 - AS_{eq}^3 \\ &= \xi\lambda(1 - S_{eq}^2) \\ &> 0 \end{aligned}$$

so the root of g is between S_{eq} and 1.

The polynomial g may also have negative roots. However, as we will now show, these (nonphysical) solutions are unstable.

The Jacobian matrix associated to equations 4.5 and 4.6 is

$$\begin{bmatrix} g'(Q_{11}) - AQ_{12}^2 & -2AQ_{11}Q_{12} \\ Q_{12}\frac{\partial f(\mathbf{Q})}{\partial Q_{12}} & \frac{g(Q_{11})-\xi\lambda}{Q_{11}} - 3AQ_{12}^2 \end{bmatrix}$$

In each of the three possible steady states, $Q_{12} = 0$, so the matrix simplifies to

$$\begin{bmatrix} g'(Q_{11}) & 0 \\ 0 & \frac{g(Q_{11})-\xi\lambda}{Q_{11}} \end{bmatrix}$$

The fact that $Q_{11} = S^{ss}$ yields the only locally stable steady state follows from the properties of g: negative roots of g satisfy $\frac{g(Q_{11})-\xi\lambda}{Q_{11}} = -\frac{\xi\lambda}{Q_{11}} > 0$.

Therefore, there is exactly one steady-state solution that is locally stable, namely $(Q_{11}, Q_{12}) = (S^{ss}, 0)$, or, written as a matrix, $\mathbf{Q} = S^{ss}\begin{bmatrix} 1 & 0 \\ 0 & -1 \end{bmatrix}$. □

We lack exact solutions when $\gamma \neq 0$, but we can investigate the behaviour of the system numerically. The system still converges to the uniformly horizontal steady state (see Figures 4.7b and 4.7c), but the transient behaviour of the system differs depending on the size of the coupling strength, γ. Figures 4.6a, 4.6b, and 4.6c demonstrate the behaviour of the model in this transient stage. The coupling of the flow to the Q-tensor has the effect of splitting the domain into patches of local order.

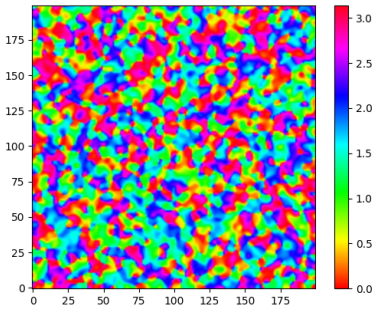

Figure 4.5: Random initial conditions for figures 4.6a-4.7c. This was generated by selecting random values for Q_{11} and Q_{12} everywhere in the domain and then smoothing. The colour represents the angle of the director.

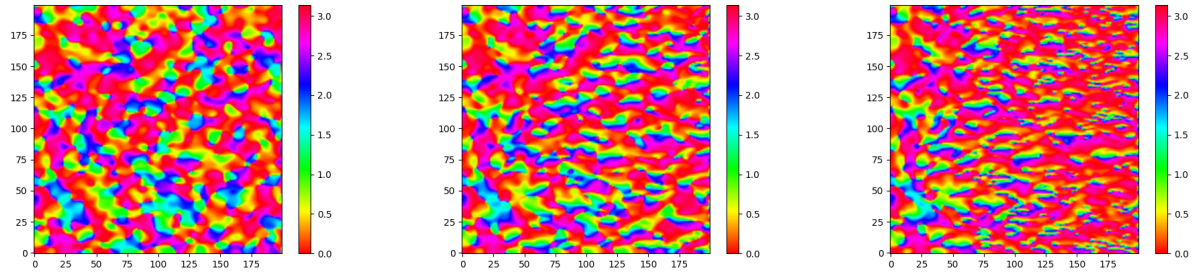

(a) $\gamma = 0$ (b) $\gamma = 0.5$ (c) $\gamma = 2$

Figure 4.6: Simulation results with $\xi = 0.5$, $\lambda = b_p = 1$, $K = 0.001$, $A_0 = 0$, and $\gamma = 0, 0.5$, and 2 at $t = 0.2$. The colour represents the angle of the director. When $\gamma = 0$, the dynamics are dominated by a combination of diffusion and the convergence described in propositions 4.3.1 and 4.3.2. As γ increases, the domain splits into two types of region: a large region of horizontally aligned cells with coherent flow (red in the images) and several small islands of cells aligned perpendicularly to the flow (teal in the images). The typical length scale of the inhomogeneities decreases as γ increases.

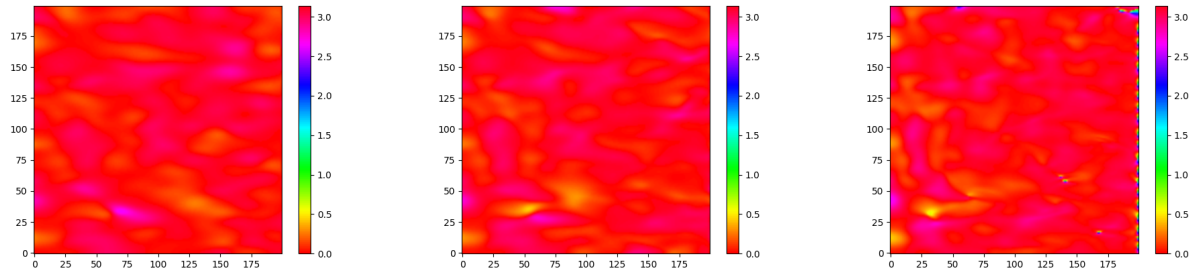

(a) $\gamma = 0$ (b) $\gamma = 0.5$ (c) $\gamma = 2$

Figure 4.7: Continuation of the simulation results in Figure 4.6 to $t = 1$. In all cases, the long-term behaviour of the simulation is the same: all inhomogeneities are either ejected from the domain by the flow or smoothed out by the effects of diffusion and shear alignment.

We may use the number of topological defects as a proxy for the number of regions observed in the images above. Defects are counted using the charge density (see Section 1.2.4). Peaks in the charge density correspond to topological defects. As we see in figure 4.8, increasing γ causes a corresponding increase in the number of topological defects.

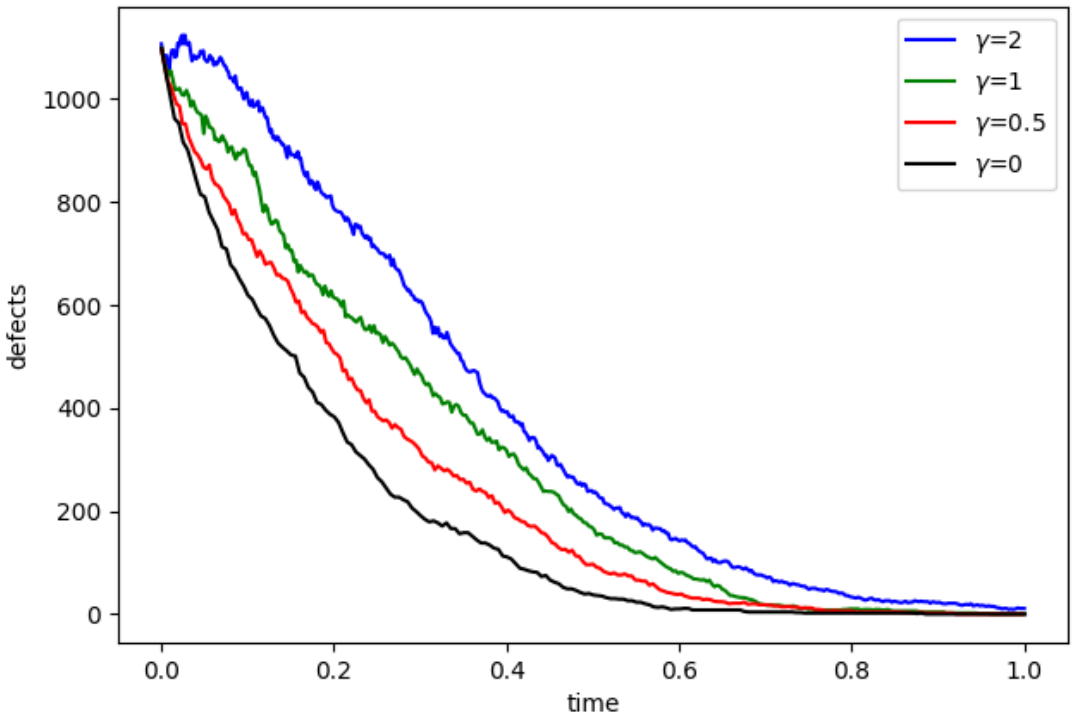

Figure 4.8: Number of defects as a function of time for microcolonies growing in a square domain, as in Figure 4.6. As γ increases, the typical length scale of the spatial inhomogeneities in $\mathbf{Q}$ decreases. This correlates with a rise in the corresponding number of topological defects.

This observation complements the findings of [72], who observed that the scale of the spatial patterning in their model could be controlled by the strength of the diffusive forces (specifically, the magnitude of K). In our model, we see an analogous behaviour, this time arising from the advective forces.

4.3.2 Inhomogeneous Solutions and Defect Formation

The two special cases treated thus far—expanding microcolonies of uniformly ordered cells and fully packed domains of disordered cells—exhibit relatively simple behaviour. The

more general case of an expanding microcolony with mixed cell orientations has much more complex behaviour, and we lack analytical solutions. We can, however, make some empirical observations.

The first observation relates to the smoothness of the boundary. Figure 4.9 shows the evolution of an expanding microcolony (using initial conditions as in 4.5) for different values of γ. As γ increases, the boundary grows increasingly asymmetric. This observation complements previous work done on fingering instabilities. In the work on nutrient limited growth we discussed in Chapter 1 ([42][27][38][33]), the inhomogeneities at the boundary was driven gradients in the nutrient field. Here, we have provided a purely physical mechanism that could lead to similar behaviour even when nutrient is plentiful.

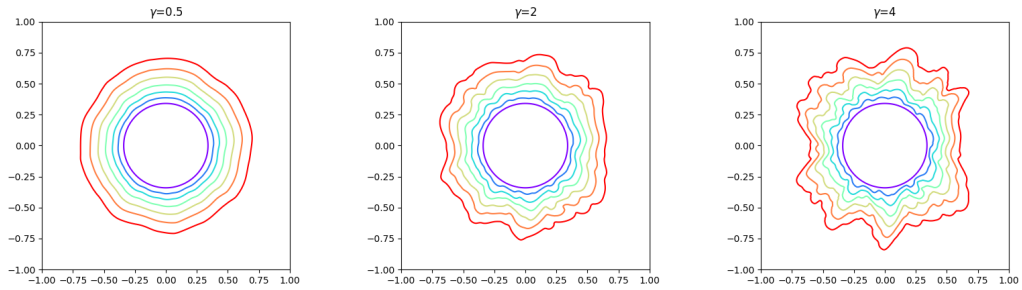

(a) $\gamma = 0.5$ (b) $\gamma = 2$ (c) $\gamma = 4$

Figure 4.9: The contour plots (a)-(c) represent the boundary of a growing microcolony sampled at increments of $\Delta t \approx 0.25$, with $\xi = 0.5$, $\lambda = 1$, $b_p = 1$, $S_{eq} = 0.9$, $A_0 = 1$, and $K = 0.001$. Initial conditions are as in figure 4.5. As the parameter γ increases, the microcolony boundary becomes increasingly irregular.

The second observation relates to defect formation. In contrast to previous models where defect generation was primarily a bulk phenomenon (e.g. as in [21]), defects in our model are generated at the boundary of the colony. In particular, our simulations suggest that they form at local minima in the signed curvature of $\partial\Omega$, and their ability to persist is greatly influenced by the magnitude of S.

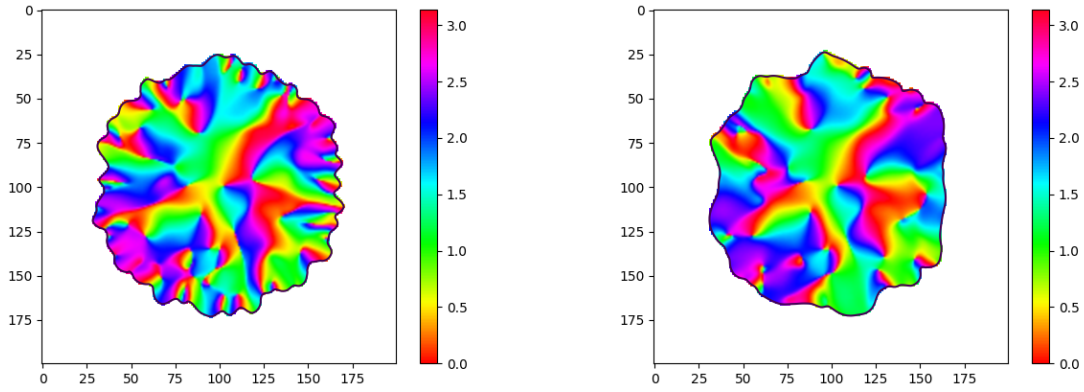

(a) $A_0 = 0$ (b) $A_0 = 1$

Figure 4.10: Snapshots of two simulations starting from identical initial conditions ($\mathbf{Q}$ as in figure 4.5, starting with a circular microcolony). The colour represents the angle of the director. Model parameters are $\xi = 0.5$, $\gamma = 2$, $\lambda = b_p = 1$, $S_{eq} = 0.9$, and $K = 0.001$. In (a), $A_0 = 0$, and there is persistent defect formation at the boundary, causing boundary irregularities. In (b), $A_0 = 1$. The corresponding thermodynamic effects increase S (not shown), which appears to suppress the ability of new defects to persist once formed.

4.4 Near-incompressible Model

We conclude this chapter with an examination of the near-incompressible models we proposed in Section 2.4, specifically equations 2.12 and 2.13, which we reproduce below:

$$(\partial_t + \vec{v} \cdot \nabla)(b\vec{v}) = -\nabla p - \mu b \mathbf{M}^{-1}\vec{v} \tag{2.12}$$

$$(\partial_t + \vec{v} \cdot \nabla)(b\vec{v}) = -\mathbf{M}\nabla p - \mu b\vec{v} \tag{2.13}$$

where $p = \begin{cases} A\,(b - b_p)^k & \text{if } b \geq b_p \\ 0 & \text{if } b < b_p \end{cases}$.

Unless otherwise stated, all simulations in this section use the following parameter values: $\lambda = 0.2$, $\mu = 25$, $\gamma = 2$, $\xi = 0.5$, $b_p = 1$, $A = 5$, $k = 3$, $A_0 = 0$, $K = 0.001$, and $D_b = 0.001$ where D_b is the diffusion rate of b (recall that we added a small diffusion term to the continuity equation for density to improve the stability of the numerics).

As we see in Figure 4.11, equations 2.12 and 2.13 yield near-identical results on elliptical solutions.

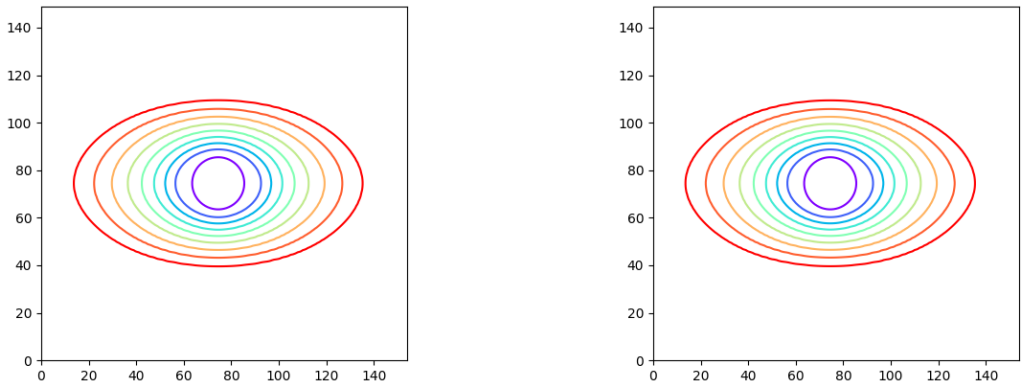

(a) Elliptical contours obtained using 2.12 (b) Elliptical contours obtained using 2.13

Figure 4.11: $b = 1$ contours for simulations of 2.12 and 2.13, starting from uniformly horizontal initial conditions ($Q_{11} = 0.75$, $Q_{12} = 0$), sampled at intervals of $\Delta t = 1.5$. Results are indistinguishable to the naked eye.

At first glance, both methods appear to reproduce the correct qualitative behaviour. However, further investigation reveals that when S is small, cells near the boundary will reorient themselves to lie tangent to the boundary (see Figure 4.12). We do not observe this behaviour in 2.10.

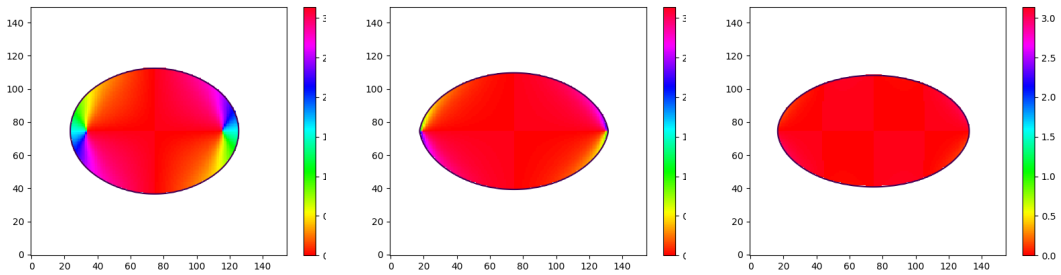

(a) $S = 0.25$ (b) $S = 0.5$ (c) $S = 0.75$

Figure 4.12: Snapshots of simulations of 2.13 at $t = 11.5$, after initialization with a horizontal director field (results for 2.12 are similar). Colour represents the angle of the director, and is only plotted in the close-packed region. The black curve is the contour $b = 1$. We observe the formation of a boundary layer, increasing in size as we shrink S.

This boundary layer appears to dramatically reduce the fingering at the microcolony boundary. Comparing Figure 4.13 with Figure 4.10a, we find that the former microcolony has a much rounder profile despite starting with similar initial conditions and using exactly the same parameter values where the models had parameters in common (the only parameter that differs between the two is λ). It appears that the only source of distortion to the boundary in Figure 4.13 is caused by the incursion of a topological defect near the bottom left of the microcolony. This behaviour matches the behaviour observed by [26].

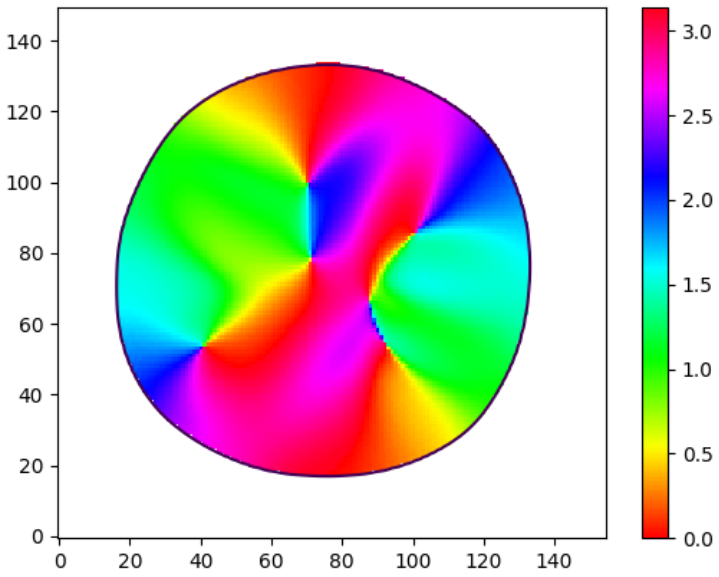

Figure 4.13: Simulation results for 2.13, starting with a circular microcolony with a randomly orientated director field. The boundary $b = 1$ remains remarkably round despite the large value of γ. The most noticeable deviation from circularity occurs near the bottom left, where a topological defect has drifted close to the boundary.

Chapter 5

Discussion and Conclusion

We began Chapter 2 by narrowing our focus to motion driven by growth, temporarily bracketing the potential contributions of other forces. In this final chapter, we will discuss strategies to integrate the mechanism we derived into existing models, and propose some avenues for future work.

5.1 Model Synthesis

The mechanism we have proposed exhibits a wide range of interesting behaviours, but it is not rich enough to cover the totality of bacterial dynamics. The question then naturally arises: How might we incorporate additional mechanisms of action? In particular, is it possible to combine our mechanism with previously published models, the majority of which rely on a Cauchy momentum equation to govern velocity?

We have already seen one potential method. The near-incompressible formulation of our model also expresses our directed expansion mechanism in terms of a Cauchy momentum equation, namely $(\partial_t + \vec{v} \cdot \nabla)(b\vec{v}) = -\mathbf{M}\nabla p - \mu b\vec{v}$, where p is some explicit function of density. It is fairly straightforward to substitute the first term on the R.H.S. for the equivalent pressure term in another model.

For example, combining our model with the model by Dell'Arciprete *et al.* [21] would yield the following governing equation for velocity:

$$\mu b\vec{v} = -\mathbf{M}\nabla p - a\nabla \cdot \mathbf{Q}$$

where $p = p_0 \max[(b/b_p - 1), 0]$.

However, as we observed in Chapter 4, prescribing pressure explicitly in terms of density does not produce the correct behaviour near the boundary of the microcolony. In the spirit of the incompressible Navier–Stokes equations, we propose the following model:

$$\begin{aligned}
\partial_t b + \nabla \cdot (b\vec{v}) &= \lambda b && \text{on } D \\
(\partial_t + \vec{v} \cdot \nabla)\mathbf{Q} &= 2\xi\mathbf{u} + \boldsymbol{\omega}\mathbf{Q} - \mathbf{Q}\boldsymbol{\omega} - \xi \mathrm{tr}(\mathbf{u}\mathbf{Q})\mathbf{Q} + \Gamma\mathbf{H} && \text{on } \Omega \\
b(\partial_t + \vec{v} \cdot \nabla)\vec{v} &= \mathbf{M}\nabla p + \nabla \cdot \boldsymbol{\sigma} - \mu b\vec{v} && \text{on } \Omega \\
\nabla \cdot \vec{v} &= \lambda && \text{on } \Omega \\
\vec{v} &= 0 && \text{on } D \setminus \Omega
\end{aligned} \tag{5.1}$$

Where:

$$\begin{aligned}
\mathbf{M} &= \frac{1 + S\gamma}{1 + 2S\gamma}\mathbf{I} + \frac{\gamma}{1 + 2S\gamma}\mathbf{Q} \\
\boldsymbol{\sigma} &= a\mathbf{Q} - \xi S\mathbf{H} + \mathbf{Q}\mathbf{H} - \mathbf{H}\mathbf{Q} \\
\Omega(t) &= \left\{(x, y) \in D \;\middle|\; b(x, y, t) \geq b_p\right\}
\end{aligned}$$

This model should, in principle, combine our incompressibile growth mechanism with the stresses that have been studied in the rest of the active nematic literature. However, we expect that a numerical implementation of such a model would require techniques more sophisticated than those we have employed in this thesis.

5.2 Model Extensions

Thus far, we have developed tools to investigate how cell orientation impacts the physics of microcolony growth. Cell orientation, however, does not have any intrinsic biological significance. In order to better illustrate the potential usefulness of this model in a biological context, we will pose three questions that have biological significance and show how equations 2.10 may be extended to investigate these questions.

Question 1: Suppose two strains of rod-shaped bacteria are growing in a semi-confined environment. If both strains have similar growth rates and do not interact except through physical forces, could cell morphology (aspect ratio) allow one strain to out-compete the other? (This question is inspired by [49], who answered the question in the affirmative for bacterial velocity.)

We can investigate this question by turning the model parameters related to morphology (ξ and γ) into approximately piece-wise constant field variables that evolve according

to a corresponding transport equation. E.g.: the evolution of ξ would be governed by $\partial_t \xi = -\vec{v} \cdot \nabla \xi$.

Given an initial distribution, say $\xi = 0.5$ in one part of the domain, $\xi = 1$ in another (each value corresponds to a different bacterial strain), we allow the system to evolve accordingly. If cell morphology impacts survival, we expect one ξ/γ value to come to dominate in the long term.

Question 2: Suppose rod-shaped bacteria are undergoing nutrient-limited growth. If cell orientation and alignment impacts the ability of nutrients permeate the microcolony (e.g. if nutrients diffuse more readily through an ordered colony than a disordered one, as hypothesized by [15], following observations in [39]), what is the ultimate impact on microcolony growth?

We would begin by turning one of the model parameters, λ, into a function of nutrient concentration, $N(x, y, t)$. The nutrient concentration, in turn, should obey an equation of the form $\partial_t N = \nabla \cdot (D(\mathbf{Q}, b)\nabla N) - c(b, N)$, where c is a consumption rate and D is a diffusion rate which, in general, may depend on $\mathbf{Q}$ and b, and which may have directional dependence (i.e. D is a matrix, not a scalar).

Question 3: Suppose two strains of rod-shaped bacteria interact via a contact-based mechanism that depends on orientation (e.g. conjugation, as demonstrated in [62]). Should we expect the average interaction rate to change if the bacteria are grown in a semi-confined environment, like a microfluidic device, as opposed to an open environment, like an agar pad?

Unlike in question 1, it is not sufficient to represent the different cell strains by associating them to particular values of, e.g. ξ or γ. Instead, we will need to introduce two bacterial densities, call them b_1 and b_2. These densities will evolve according to a pair of equations:

$$\partial_t b_1 + \nabla \cdot (\vec{v} b_1) = \lambda b_1 + f(b_1, b_2, \mathbf{Q})$$
$$\partial_t b_2 + \nabla \cdot (\vec{v} b_2) = \lambda b_2 + g(b_1, b_2, \mathbf{Q})$$

where f and g are interaction terms.

Because the interaction terms impact the total bacterial growth, we need to revise our incompressibility condition. When the total density reaches the packing density, $b_1 + b_2 = b_p$, *and* the total bacterial growth is non-negative (i.e. $\lambda(b_1 + b_2) + f + g \geq 0$), we expect

the material derivative of $b_1 + b_2$ to be zero.

$$\partial_t(b_1 + b_2) + \nabla \cdot (\vec{v}(b_1 + b_2)) = \lambda(b_1 + b_2) + f + g$$

$$\partial_t(b_1 + b_2) + \cancelto{0}{\vec{v} \cdot \nabla(b_1 + b_2)} + (b_1 + b_2)\nabla \cdot \vec{v} = \lambda(b_1 + b_2) + f + g$$

$$\nabla \cdot \vec{v} = \lambda + \frac{f + g}{b_1 + b_2}$$

In the rest of the domain, where the density is below packing density or the net growth is negative, the velocity is zero. From here, the rest of the model derivation follows as usual.

5.3 Towards A Full FEM Implementation

The mixed finite element and finite difference scheme we described in Section 3.2.4 allows for a relatively simple treatment of the Beris-Edwards equation in system 2.10. However, it suffers from a significant drawback: it requires us to define the Q-tensor in parts of the domain where bacterial density is zero. This would not be a problem, except for the presence of the diffusion term in the Beris-Edwards equation, as none of the other terms in the Beris-Edwards equation allow for communication between the close-packed region, Ω, and the rest of the domain. In principle, we could define the Q-tensor to take some arbitrary value (say zero) outside the close-packed region, and the dynamics of the system would proceed as desired. Unfortunately, the diffusion term allows the values outside the close-packed region to influence the dynamics inside the close-packed region.

The natural solution is to restrict $\mathbf{Q}$ to be defined only inside Ω and impose suitable boundary conditions on $\partial\Omega$. Unfortunately, finite difference methods are not naturally suited to deal with such irregular boundaries. This motivates us to move towards a scheme using only finite element methods. Such a numerical scheme would have the additional practical benefits. The computational bottlenecks in our mixed implementation are all in the finite difference portion of the implementation, so a fully FEM implementation has the potential to be much faster. In addition, translation between the FEM and finite difference representations could be eliminated, removing a source of error.

We have yet to implement a working FEM implementation, but we propose the following as one promising avenue of investigation. Notice that we can write the components of $\mathbf{u}$

and $\boldsymbol{\omega}$ in divergence form. E.g., u_{11} may be written as:

$$\begin{aligned} u_{11} &= \frac{1}{2}\left(\partial_x v_x - \partial_y v_y\right) \\ &= \frac{1}{2}\nabla \cdot \left(\begin{bmatrix} 1 & 0 \\ 0 & -1 \end{bmatrix} \vec{v} \right) \\ &= \frac{1}{2}\nabla \cdot \left(\begin{bmatrix} -1 & 0 \\ 0 & 1 \end{bmatrix} \mathbf{M}\nabla p \right) \end{aligned}$$

Similarly, $u_{12} = \frac{1}{2}\nabla \cdot \left(\begin{bmatrix} 0 & -1 \\ -1 & 0 \end{bmatrix} \mathbf{M}\nabla p \right)$ and $\omega_{12} = \frac{1}{2}\nabla \cdot \left(\begin{bmatrix} 0 & 1 \\ -1 & 0 \end{bmatrix} \mathbf{M}\nabla p \right)$.

This allows us to apply the divergence theorem to put the Beris-Edwards equation(s) into weak form. Multiplying the equation for Q_{11} by a test function ϕ_1 and integrating yields:

$$\begin{aligned} \int_\Omega \left(\partial_t Q_{11} - \mathbf{M}\nabla p \cdot \nabla Q_{11}\right)\phi_1 dA &= \int_\Omega \left(2\xi u_{11} - \xi \mathrm{tr}(\mathbf{uQ})Q_{11} + 2\omega_{12}Q_{12} + H_{11}\right)\phi_1 dA \\ &= \int_\Omega 2u_{11}\xi(1-Q_{11}^2)\phi_1 - 2u_{12}\xi Q_{12}Q_{11}\phi_1 \\ &\quad + 2\omega_{12}Q_{12}\phi_1 + H_{11}\phi_1 dA \\ &= \int_\Omega \nabla \cdot \left(\begin{bmatrix} -1 & 0 \\ 0 & 1 \end{bmatrix} \mathbf{M}\nabla p \right) \xi(1-Q_{11}^2)\phi_1 dA \\ &\quad - \int_\Omega \nabla \cdot \left(\begin{bmatrix} 0 & -1 \\ -1 & 0 \end{bmatrix} \mathbf{M}\nabla p \right) \xi Q_{12}Q_{11}\phi_1 dA \\ &\quad + \int_\Omega \nabla \cdot \left(\begin{bmatrix} 0 & 1 \\ -1 & 0 \end{bmatrix} \mathbf{M}\nabla p \right) Q_{12}\phi_1 dA \\ &\quad + \int_\Omega H_{11}\phi_1 dA \end{aligned}$$

The terms on the R.H.S. can then be rewritten using the divergence theorem. For example, the first term is rewritten as follows:

$$\begin{aligned} \int_\Omega \nabla \cdot \left(\begin{bmatrix} -1 & 0 \\ 0 & 1 \end{bmatrix} \mathbf{M}\nabla p \right) \xi(1-Q_{11}^2)\phi_1 dA &= \int_{\partial\Omega} \xi(1-Q_{11}^2)\phi_1 \left(\begin{bmatrix} -1 & 0 \\ 0 & 1 \end{bmatrix} \mathbf{M}\nabla p \right) \cdot \hat{n} dS \\ &\quad - \int_\Omega \left(\begin{bmatrix} -1 & 0 \\ 0 & 1 \end{bmatrix} \mathbf{M}\nabla p \right) \cdot \nabla \left(\xi(1-Q_{11}^2)\phi_1 \right) dA \end{aligned}$$

The end result is a system of three coupled equations—nonlinear equations for Q_{11} and Q_{12} and a Poisson equation for p—all in weak form, which require no more than first derivatives for each of the relevant quantities. These equations can, at least in principle, be linearized and solved using Newton's method.

We attempted to implement this formulation early on but abandoned the approach because it produced singularities along the open boundary of the domain. However, at the time we were using the Olmsted-Goldbart equations, 1.9, not the Beris-Edwards equations, 1.8, so it is unclear whether these singularities were inherent to the above formulation, the result of incorrect boundary conditions, or because the Olmsted-Goldbart equations have no restoring force that keeps $\mathbf{Q}$ bounded.

5.4 Validation

Finally, a confession. When we first conceived of this project, our goal was threefold: (a) to develop a continuum model of 2-dimensional microcolony dynamics, (b) to conduct corresponding microscopy experiments using microfluidic devices, extracting quantitative data using image processing techniques, and (c) to compare the results of the continuum model to the experimental data, using simulated results from an agent-based model to bridge the gap between the two. In this thesis, we have presented the results of (a). Goal (b) is well underway, and is being pursued by other members of the Ingalls Quantitative Cell Biology Lab. However, time constraints being what they are, (c) remains almost entirely unaddressed. As such, the results of this thesis are, for the time being, mathematical in nature, not scientific.

To give a brief summary of our intentions regarding model validation, our strategy would have been to extract low-dimensional, quantitative descriptions of the system's behaviour (summary statistics), such as the number of topological defects or the roundness of the boundary, and use these to compare the experimental data to the behaviour of our PDE model. For a detailed account of our thoughts on model calibration, we refer readers to [71].

5.5 Conclusion

In this thesis, we have developed a new model for the microcolony dynamics of rod-shaped bacteria, based on an extension of the Hubble mechanism proposed by Dell'Arciprete *et*

al. [21]. We began our investigation by revisiting the incompressible models from the literature on nutrient-limited growth. We showed that the physics in these models could be derived from an optimization problem: minimizing the total kinetic energy. Armed with this insight, we modified the optimization problem to account for cell morphology, using tools from liquid crystal theory to describe the orientation and orderliness of cells. The result is a model of microcolony growth where new biomass spreads asymmetrically based on the orientation of the cells. Using a combination of finite difference methods, level set methods, and unfitted finite element methods, we developed a numerical scheme to simulate our model. We validated this scheme against analytic solutions, and used it to explore the behaviour of our model in more complex scenarios where analytic solutions are lacking. We find that the model exhibits several of the same behaviours observed in real microcolonies: spontaneous alignment in confined domains, defect formation, and fingering at the boundary. It is our hope that this novel Hubble mechanism will be incorporated into the existing models of microcolony growth, which have thus far failed to account for non-gradient effects.

References

[1] David Adalsteinsson and James A Sethian. The fast construction of extension velocities in level set methods. *Journal of Computational Physics*, 148(1):2–22, 1999.

[2] Rosalind J Allen and Bartlomiej Waclaw. Bacterial growth: a statistical physicist's guide. *Reports on Progress in Physics*, 82(1):016601, 2018.

[3] Denis Andrienko. Introduction to liquid crystals. *IMPRS school, Bad Marienberg*, 14:4, 2006.

[4] Aleksandra Ardaševa and Amin Doostmohammadi. Topological defects in biological matter. *Nature Reviews Physics*, 4(6):354–356, 2022.

[5] Mustafa Basaran, Y Ilker Yaman, Tevfik Can Yüce, Roman Vetter, and Askin Kocabas. Large-scale orientational order in bacterial colonies during inward growth. *Elife*, 11:e72187, 2022.

[6] Christopher Basting and Dmitri Kuzmin. A minimization-based finite element formulation for interface-preserving level set reinitialization. *Computing*, 95(Suppl 1):13–25, 2013.

[7] David J Beebe, Glennys A Mensing, and Glenn M Walker. Physics and applications of microfluidics in biology. *Annual review of biomedical engineering*, 4(1):261–286, 2002.

[8] Antony N Beris, Brian J Edwards, et al. *Thermodynamics of flowing systems: with internal microstructure*. Number 36. Oxford University Press on Demand, 1994.

[9] Farzan Beroz, Jing Yan, Yigal Meir, Benedikt Sabass, Howard A Stone, Bonnie L Bassler, and Ned S Wingreen. Verticalization of bacterial biofilms. *Nature physics*, 14(9):954–960, 2018.

[10] Nicole Billings, Alona Birjiniuk, Tahoura S Samad, Patrick S Doyle, and Katharina Ribbeck. Material properties of biofilms—a review of methods for understanding permeability and mechanics. *Reports on Progress in Physics*, 78(3):036601, 2015.

[11] Matthew L Blow, Sumesh P Thampi, and Julia M Yeomans. Biphasic, lyotropic, active nematics. *Physical review letters*, 113(24):248303, 2014.

[12] Susanne C Brenner, L Ridgway Scott, and L Ridgway Scott. *The mathematical theory of finite element methods*, volume 3. Springer, 2008.

[13] Erik Burman. Ghost penalty. *Comptes Rendus Mathematique*, 348(21-22):1217–1220, 2010.

[14] Elizabeth Caplice and Gerald F Fitzgerald. Food fermentations: role of microorganisms in food production and preservation. *International journal of food microbiology*, 50(1-2):131–149, 1999.

[15] HoJung Cho, Henrik Jönsson, Kyle Campbell, Pontus Melke, Joshua W Williams, Bruno Jedynak, Ann M Stevens, Alex Groisman, and Andre Levchenko. Self-organization in high-density bacterial colonies: efficient crowd control. *PLoS biology*, 5(11):e302, 2007.

[16] David L Chopp. Some improvements of the fast marching method. *SIAM Journal on Scientific Computing*, 23(1):230–244, 2001.

[17] Richard Courant, Kurt Friedrichs, and Hans Lewy. Über die partiellen differenzengleichungen der mathematischen physik. *Mathematische annalen*, 100(1):32–74, 1928.

[18] Richard Courant, Kurt Friedrichs, and Hans Lewy. On the partial difference equations of mathematical physics. *IBM journal of Research and Development*, 11(2):215–234, 1967.

[19] Carlos A De Moura and Carlos S Kubrusly. The courant–friedrichs–lewy (cfl) condition. *AMC*, 10(12), 2013.

[20] Frits de Prenter, Christoph Lehrenfeld, and André Massing. A note on the stability parameter in nitsche's method for unfitted boundary value problems. *Computers & Mathematics with Applications*, 75(12):4322–4336, 2018.

[21] D Dell'Arciprete, ML Blow, AT Brown, FDC Farrell, Juho S Lintuvuori, AF McVey, D Marenduzzo, and Wilson CK Poon. A growing bacterial colony in two dimensions as an active nematic. *Nature communications*, 9(1):1–9, 2018.

[22] Daniele Antonio Di Pietro and Alexandre Ern. *Mathematical aspects of discontinuous Galerkin methods*, volume 69. Springer Science & Business Media, 2011.

[23] Amin Doostmohammadi, Jordi Ignés-Mullol, Julia M Yeomans, and Francesc Sagués. Active nematics. *Nature communications*, 9(1):3246, 2018.

[24] Amin Doostmohammadi and Benoit Ladoux. Physics of liquid crystals in cell biology. *Trends in cell biology*, 2021.

[25] Amin Doostmohammadi, Sumesh P Thampi, Thuan B Saw, Chwee T Lim, Benoit Ladoux, and Julia M Yeomans. Celebrating soft matter's 10th anniversary: Cell division: a source of active stress in cellular monolayers. *Soft Matter*, 11(37):7328–7336, 2015.

[26] Amin Doostmohammadi, Sumesh P Thampi, and Julia M Yeomans. Defect-mediated morphologies in growing cell colonies. *Physical review letters*, 117(4):048102, 2016.

[27] Ravindra Duddu, Stéphane Bordas, David Chopp, and Brian Moran. A combined extended finite element and level set method for biofilm growth. *International Journal for Numerical Methods in Engineering*, 74(5):848–870, 2008.

[28] Hermann J Eberl and Laurent Demaret. A finite difference scheme for a degenerated diffusion equation arising in microbial ecology. *Electron. J. Differ. Equ*, 15:77–95, 2007.

[29] Jerald L Ericksen. Conservation laws for liquid crystals. *Transactions of the Society of Rheology*, 5(1):23–34, 1961.

[30] Jerald L Ericksen. Hydrostatic theory of liquid crystals. *Archive for Rational Mechanics and Analysis*, 9(1):371–378, 1962.

[31] Jack A Gilbert, Martin J Blaser, J Gregory Caporaso, Janet K Jansson, Susan V Lynch, and Rob Knight. Current understanding of the human microbiome. *Nature medicine*, 24(4):392–400, 2018.

[32] L Giomi, L Mahadevan, B Chakraborty, and MF Hagan. Banding, excitability and chaos in active nematic suspensions. *Nonlinearity*, 25(8):2245, 2012.

[33] Chiara Giverso, Marco Verani, and Pasquale Ciarletta. Branching instability in expanding bacterial colonies. *Journal of The Royal Society Interface*, 12(104):20141290, 2015.

[34] Didier Gonze, Katharine Z Coyte, Leo Lahti, and Karoline Faust. Microbial communities as dynamical systems. *Current opinion in microbiology*, 44:41–49, 2018.

[35] Egbert F Gramsbergen, Lech Longa, and Wim H de Jeu. Landau theory of the nematic-isotropic phase transition. *Physics Reports*, 135(4):195–257, 1986.

[36] Matthew AA Grant, Bartłomiej Wacław, Rosalind J Allen, and Pietro Cicuta. The role of mechanical forces in the planar-to-bulk transition in growing escherichia coli microcolonies. *Journal of The Royal Society Interface*, 11(97):20140400, 2014.

[37] Rifat Hayat, Safdar Ali, Ummay Amara, Rabia Khalid, and Iftikhar Ahmed. Soil beneficial bacteria and their role in plant growth promotion: a review. *Annals of microbiology*, 60:579–598, 2010.

[38] Raphael Hornung, Alexander Grünberger, Christoph Westerwalbesloh, Dietrich Kohlheyer, Gerhard Gompper, and Jens Elgeti. Quantitative modelling of nutrient-limited growth of bacterial colonies in microfluidic cultivation. *Journal of the Royal Society Interface*, 15(139):20170713, 2018.

[39] Jan Hrabe, Sabina Hrabětová, and Karel Segeth. A model of effective diffusion and tortuosity in the extracellular space of the brain. *Biophysical journal*, 87(3):1606–1617, 2004.

[40] Jona Kayser, Carl F Schreck, Matti Gralka, Diana Fusco, and Oskar Hallatschek. Collective motion conceals fitness differences in crowded cellular populations. *Nature ecology & evolution*, 3(1):125–134, 2019.

[41] Hassan Khassehkhan, Thomas Hillen, and Hermann J Eberl. A nonlinear master equation for a degenerate diffusion model of biofilm growth.

[42] Isaac Klapper and Jack Dockery. Finger formation in biofilm layers. *SIAM Journal on Applied Mathematics*, 62(3):853–869, 2002.

[43] Isaac Klapper and Jack Dockery. Mathematical description of microbial biofilms. *SIAM review*, 52(2):221–265, 2010.

[44] Christoph Lehrenfeld. High order unfitted finite element methods on level set domains using isoparametric mappings. *Computer Methods in Applied Mechanics and Engineering*, 300:716–733, 2016.

[45] Christoph Lehrenfeld. A higher order isoparametric fictitious domain method for level set domains. In *Geometrically unfitted finite element methods and applications*, pages 65–92. Springer, 2017.

[46] Christoph Lehrenfeld, Fabian Heimann, Janosch Preuß, and Henry von Wahl. ngsxfem: Add-on to ngsolve for geometrically unfitted finite element discretizations. *Journal of Open Source Software*, 6(64):3237, 2021.

[47] Frank M Leslie. Some constitutive equations for liquid crystals. *Archive for Rational Mechanics and Analysis*, 28(4):265–283, 1968.

[48] Yan Liu, Bo Li, and Xi-Qiao Feng. Buckling of growing bacterial chains. *Journal of the Mechanics and Physics of Solids*, 145:104146, 2020.

[49] Oliver J Meacock, Amin Doostmohammadi, Kevin R Foster, Julia M Yeomans, and William M Durham. Bacteria solve the problem of crowding by moving slowly. *Nature Physics*, 17(2):205–210, 2021.

[50] Prashant Mishra. *Pattern Formation in Active Nematics*. PhD thesis, Syracuse University, 2017.

[51] Nigel J Mottram and Christopher JP Newton. Introduction to q-tensor theory. *arXiv preprint arXiv:1409.3542*, 2014.

[52] Joachim Nitsche. Über ein variationsprinzip zur lösung von dirichlet-problemen bei verwendung von teilräumen, die keinen randbedingungen unterworfen sind. In *Abhandlungen aus dem mathematischen Seminar der Universität Hamburg*, volume 36, pages 9–15. Springer, 1971.

[53] Peter D Olmsted. Perspectives on shear banding in complex fluids. *Rheologica Acta*, 47(3):283–300, 2008.

[54] Peter D Olmsted and Paul Goldbart. Theory of the nonequilibrium phase transition for nematic liquid crystals under shear flow. *Physical Review A*, 41(8):4578, 1990.

[55] Stanley Osher, Ronald Fedkiw, and K Piechor. Level set methods and dynamic implicit surfaces. *Appl. Mech. Rev.*, 57(3):B15–B15, 2004.

[56] Stanley Osher and Nikos Paragios. *Geometric level set methods in imaging, vision, and graphics*. Springer Science & Business Media, 2003.

[57] Judith Pérez-Velázquez, Meltem Gölgeli, and Rodolfo García-Contreras. Mathematical modelling of bacterial quorum sensing: a review. *Bulletin of mathematical biology*, 78:1585–1639, 2016.

[58] Janosch Preuß. Higher order unfitted isoparametric space-time fem on moving domains. *Master's thesis, University of Gottingen*, 2018.

[59] Elias Putzig, Gabriel S Redner, Arvind Baskaran, and Aparna Baskaran. Instabilities, defects, and defect ordering in an overdamped active nematic. *Soft matter*, 12(17):3854–3859, 2016.

[60] Thuan Beng Saw, Amin Doostmohammadi, Vincent Nier, Leyla Kocgozlu, Sumesh Thampi, Yusuke Toyama, Philippe Marcq, Chwee Teck Lim, Julia M Yeomans, and Benoit Ladoux. Topological defects in epithelia govern cell death and extrusion. *Nature*, 544(7649):212–216, 2017.

[61] Joachim Schöberl. C++ 11 implementation of finite elements in ngsolve. *Institute for analysis and scientific computing, Vienna University of Technology*, 30, 2014.

[62] Jose Seoane, Tatiana Yankelevich, Arnaud Dechesne, Brian Merkey, Claus Sternberg, and Barth F Smets. An individual-based approach to explain plasmid invasion in bacterial populations. *FEMS microbiology ecology*, 75(1):17–27, 2011.

[63] James A Sethian. A fast marching level set method for monotonically advancing fronts. *Proceedings of the National Academy of Sciences*, 93(4):1591–1595, 1996.

[64] James A Sethian and Peter Smereka. Level set methods for fluid interfaces. *Annual review of fluid mechanics*, 35(1):341–372, 2003.

[65] Pin-Tzu Su, Pei-Wen Yen, Shao-Hung Wang, Chi-Hung Lin, Arthur Chiou, and Wan-Jr Syu. Factors affecting daughter cells' arrangement during the early bacterial divisions. *PloS one*, 5(2):e9147, 2010.

[66] Marcus J Tindall, Philip K Maini, Steven L Porter, and Judith P Armitage. Overview of mathematical approaches used to model bacterial chemotaxis ii: bacterial populations. *Bulletin of mathematical biology*, 70:1570–1607, 2008.

[67] Fredi Tröltzsch. *Optimal control of partial differential equations: theory, methods, and applications*, volume 112. American Mathematical Soc., 2010.

[68] Nico P Van Dijk, Kurt Maute, Matthijs Langelaar, and Fred Van Keulen. Level-set methods for structural topology optimization: a review. *Structural and Multidisciplinary Optimization*, 48:437–472, 2013.

[69] Dmitri Volfson, Scott Cookson, Jeff Hasty, and Lev S Tsimring. Biomechanical ordering of dense cell populations. *Proceedings of the National Academy of Sciences*, 105(40):15346–15351, 2008.

[70] Ping Wang, Lydia Robert, James Pelletier, Wei Lien Dang, Francois Taddei, Andrew Wright, and Suckjoon Jun. Robust growth of escherichia coli. *Current biology*, 20(12):1099–1103, 2010.

[71] Aaron Yip, Julien Smith-Roberge, Sara Haghayegh Khorasani, Marc G Aucoin, and Brian P Ingalls. Calibrating spatiotemporal models of microbial communities to microscopy data: A review. *PLOS Computational Biology*, 18(10):e1010533, 2022.

[72] Zhihong You, Daniel JG Pearce, Anupam Sengupta, and Luca Giomi. Geometry and mechanics of microdomains in growing bacterial colonies. *Physical Review X*, 8(3):031065, 2018.

[73] Zhihong You, Daniel JG Pearce, Anupam Sengupta, and Luca Giomi. Mono-to multilayer transition in growing bacterial colonies. *Physical review letters*, 123(17):178001, 2019.

[74] Kevin D Young. Bacterial morphology: why have different shapes? *Current opinion in microbiology*, 10(6):596–600, 2007.